August 2016

Ph.D. Dissertation

Co-sensitization of TiO$_2$ Photoelectrodes in Panchromatic Dye-Sensitized Solar cells

판크로마틱 染料感應太陽電地에서 TiO$_2$ 光電極의 共感應

Graduate School of Chosun University

Department of Energy Convergence

Jung-Hun Kim

Co-sensitization of TiO$_2$ Photoelectrodes in Panchromatic Dye-Sensitized Solar cells

판크로마틱 染料感應太陽電地에서 TiO$_2$ 光電極의 共感應

August 25, 2016

Graduate School of Chosun University

Department of Energy Convergence

Jung-Hun Kim

Co-sensitization of TiO$_2$ Photoelectrodes in Panchromatic Dye-Sensitized Solar cells

Supervised by Professor Jae-Wook Lee

This dissertation is submitted to the Graduate School of Chosun University in partial fulfillment of the requirements for the Degree of Doctor of Philosophy in Engineering

April 2016

Graduate School of Chosun University

Department of Energy Convergence

Jung-Hun Kim

Jung-Hun Kim's dissertation is certified

Thesis Committee Members

Ph.D./Prof.	Hee Moon
Committee chair	Chonnam National University

Ph.D./Prof.	In-Hwa Lee
Committee	Chosun University

Ph.D./Prof.	Jung-Heon Lee
Committee	Chosun University

Ph.D./Prof.	Kyung-Hee Park
Committee	Chonnam National University

Ph.D./Prof.	Jae-Wook Lee
Committee	Chosun University

June 2016

Graduate School of Chosun University

Table of Contents

Chapter 5. Light-Harvesting over a Wide Wavelength Range using a Variety of Natural Dyes with Rainbow Dye-Sensitized Solar Cells ·· 78

List of Tables

List of Figures

Chapter 4

Chapter 5

국문 초록

판크로마틱 染料感應太陽電地에서 TiO$_2$ 光電極의 共感應

김 정 훈

지도교수 : 이재욱

신재생에너지융합학과

조선대학교 대학원

18 ~ 19세기 영국의 산업혁명 이후 인류가 본격적인 산업화에 돌입하게 되면서 온실가스 배출량은 기하급수적으로 증가하였고 21세기 이르러 지구온난화현상이 인류를 위협하게 되었다. 기후 변화에 관한 정부 간 협의체인 IPCC에 따르면, 1880년 산업화 이전에 비해 현재 지구의 평균 기온은 0.85℃가 상승함에 따라 해수면은 약 19 cm가 상승하였다고 발표했다. 그런데 현재와 같은 온실 가스의 배출량이 계속된다면 향후 2100년 지구 평균 온도는 지금보다 3.7℃가 더 상승되고 해수면은 63 cm가 더 높아질 것으로 예측되었다. 이에 따라 온실 가스 감축, 지구 환경 변화 대응에 대한 국제회의가 지속적으로 진행되어 왔다. 기후변화 대응 논의를 위해 UN회원국 195개국이 참여한 21차 당사국 총회가 2015년 12월게 파리에서 개최되었다. UN회원국인 195개국 모두가 참여해 자발적 감축 목표 안을 제출하였고 최종적으로 온실가스 감축 의무에 동참하기로 합의를 내렸다. 대한민국(온실 가스 배출 세계 7위)은 파리기후협약에 따라 2030년까지 BAU대비 37%까지 감축을 목표로 제시하였다. 37%목표를 달성하기 위해서 화석연료를 대체할 에너지 자원으로 원자력과 신재생에너지가 대안으로 논의되었다. 2004년 신에너지 및 재생에너지 개발 이용 보급 촉진법에 의해 재생에너지는 태양열, 태양전지, 바이오매스, 풍력, 소수력, 지열, 해양, 폐기물에너지 등 8개 분야이고 신에너지는 수소, 연료전지, 석탄액화가스화 등 3개 분야이다.

친환경 재생에너지원으로서 염료감응태양전지를 다루었다. 실리콘 및 화합물 계열 반도체 태양전지와는 달리 광합성의 원리를 이용한 고효율의 태양전지의 메카니즘이 1991년 Grälzel(효율 7.1%)에 의하여 Nature지에 보고되어 처음으로 염료감응태양전지

로 알려지게 되었다. 염료감응태양전지의 효율 향상 및 셀 안정성을 위해 TiO₂ 나노 구조체 및 광전극 구조, 다양한 염료 개발, 전해질, 그리고 전도성 기판 및 플렉시블 기판 등에 관한 핵심 연구들이 수행되고 있다.

본 연구에서는 광전극 제조를 위해 염료감응태양전지의 전자의 전달 및 전류 발생에 중요한 역할을 하는 TiO₂ 광전극을 제조하고 광기전 특성을 조사하였다. TiO₂ 광전극에서 염료의 흡착량 및 빛 산란 효과를 증가시키기 위해 긴 골격구조가 있는 나비 날개 구조체를 이용하여 나노포러스 TiO₂를 제조하였다. 이렇게 얻은 다결정 나노입자는 염료감응태양전지에서 효과적인 아나타제의 결정상과 약 12.1 nm 입자 크기를 보였다. 나비 날개 구조 TiO₂ 광전극을 제조한 후 FE-SEM, XRD, UV-vis 등의 기기분석을 통해 상용화된 TiO₂ paste로 제작된 광전극과 비교 평가하였다. 상용화된 TiO₂ 광전극 보다 나비 날개 구조 TiO₂ 광전극의 경우 높은 효율을 보였다. 그리고 합성된 나비 날개 구조 TiO₂ 광전극 필름 상에서 N719 염료의 흡착특성이 염료감응태양전지 효율에 미치는 영향을 체계적으로 조사하였다. 이를 위해 나비 날개 구조 TiO₂ 광전극 필름 상에서 시간에 따른 N719 염료의 흡착 속도론적 특성을 고찰한 결과 나비 날개 구조 TiO₂ 광전극의 흡착 속도가 더 빠름을 알 수 있었다. 특이한 나비 날개 구조 TiO₂ 광전극의 구조가 빛 수확 및 빛 산란 효과로 인해 염료감응태영전지의 효율에 긍정적인 영향을 미친 것으로 분석되었고 IPCE, OCVD, Impedance 등을 이용하여 전기화학특성을 분석하였다.

흡수파장이 서로 다른 여러 가지 염료를 혼합하는 방법이 있다. 흡수파장이 서로 다른 염료를 무순위로 혼합할 경우 각각의 염료가 선호하는 빛을 선택적으로 활용할 수 없게 될 수도 있다. 따라서 여러 가지 염료를 선택적으로 배열 기술이 필요하다. 염료감응태양전지에서 염료를 선택적으로 배열하기란 쉽지 않다. 첫 번째 흡착된 염료는 고온의 열처리 과정에서 분해될 수 있다. 따라서 고전적인 염료감응태양전지 제법으로는 여러 가지 염료를 TiO₂ 필름에 배열하기 쉽지 않다. TiO₂ 필름을 전도성 기판 위에 형성 한 후 TiO₂ 필름 표면 전부를 첫 번째 염료로 흡착한다. 그리고 첫 번째 염료가 흡착된 일부분만을 선택적으로 탈착한 뒤 두 번째 염료로 흡착한다. 이 기술의 핵심에는 나노구조 TiO₂ 필름을 어떻게 활용할 것인가에 달려있다. 하지만 이 기술은 흡착 기술을 고려하지 않은 방법이다. 이에 따라 흡착 장치 개발로 효과적은 흡착 방법을 제시하고 UV-vis 분석을 통하여 TiO₂ 광전극 표면에서 일어나는 N719 염료와 MK-2 염료의 흡착 특성을 관찰하였다. 단일성분 흡착에서 N719와 MK-2의 q_e 값과 흡착반응 속도 상수 k 값이 MK-2가 더 높고 속도가 빠른 것을 알 수 있었다. 순차적 흡착에서

MK-2/N719의 총 q_e 값이 더 높았다. 이는 추후 효율에서도 향상된 것을 알 수 있었다. 이로 인해 N719 염료가 상대적으로 느리지만 강한 결합으로 확산 된 반면 MK-2 염료는 빠르지만 TiO₂ 광전극의 결합이 약한 흡착특성을 보였습니다. 나노포러스 TiO₂ 광전극 표면에 N719 및 MK-2 염료 흡착량이 염료의 흡착 평형 및 반응 속도의 차이에 기초하여 제어 될 수 있음을 알 수 있다. 또한 흡착 방법에 따흔 흡착된 TiO₂ 광전극을 CV, Impedance 등을 이용하여 전기화학특성을 분석하였다.

 여러 가지 색상을 구현하면서 값 비싼 합성염료를 대처할 수 있는 천연염료를 이용하여 다양한 색상을 구현하는 레이보우 염료감응태양전지를 제조하였다. 사용한 사용화 된 3가지 염료 중 하나인 치자황은 치자나무의 과실로부터 얻어진 수용성 크로신 및 크로세틴을 주성분으로 색상은 아름다운 황색을 나타내지만 빛과 산에 약하다. 이리드이드 배당 체와 단백질 분해물의 혼합물에 β-글리코시 다제를 첨가하여 얻어진 것으로 색은 파랑색을 띄는 것은 치자청이다. 마지막 치자적은 이리드이드 배당 체의 에스테르 가수 분해 물과 단백질 분해물의 혼합물에 β- 글리코시 다제를 첨가해 얻어진 것이다. 천연에서 얻은 염료(치자황, 치자청, 치자적)를 이용하여 다양한 색상의 염료감응태양전지를 구현하고자 기초연구를 진행하였다. 모든 빛을 흡수하는 색은 검정색으로 3가지 색상(치자황, 치자청, 치자적)을 이용하여 검정색을 만들어 실험하였습니다. 염료의 특성은 UV-스펙트럼을 이용하여 치자황은 400 ~ 450 nm 파장에서 큰 픽이 보였고 치자청은 550 ~ 600 nm 파장에서 큰 픽이 보였고 치자적은 500~550nm 파장에서 큰 픽이 보였다. 염료흡착 시간의 영향에 따른 TiO₂ 광전극의 물리 화학적 특성의 변화를 체계적으로 조사하였다. 그 결과 일정 시간이 지난 뒤에는 에너지 변환효율이 낮아졌고 저항을 커짐을 알 수 있었다. 염료 흡착 시간에 따라 염료감응태양전지의 전류밀도 및 에너지 변환효율에도 많은 영향을 미쳤다. 또한 치자나무에서 추출한 치자황, 치자청, 치자적 염료의 흡착 특성을 연구하였다. 치자황이 가장 흡착 특성이 좋았고 치자적은 가장 작은 흡착 하는 것을 보였다. 치자황, 치자청, 치자적의 농도별 UV 스펙트럼의 결과로 비어-램버트 법칙을 이용하여 상업용 천연 검정색 염료의 농도를 알 수 있었다. 이는 비어-램버트 법칙으로 성공적으로 천연 염료 혼합물의 농도를 결정하는데 사용될 수 있음을 알 수 있었다. 치자황, 치자청, 치자적을 사용하여 레이보우 염료감응태양전지를 성공적으로 제조 할 수 있었다. 또한 염료 흡착 특성을 고려하여 천연 염료의 다양한 색을 이용하여 여러 색을 가지는 염료감응태양전지를 구현할 수 있을 것으로 판단되어진다. 본 연구를 통해 얻은 최적화된 염료 흡착 조건을 이용하여 다양한 색상을 구현하면서 높은 에너지 변환 효율을 가지는 염료감응태양전

지를 제조할 수 있었다. 본 논문에서 수행한 TiO$_2$ 광전극의 제조 및 염료 흡착 특성에 관한 체계적인 연구 결과는 향후 상업용 염료감응태양전지 모듈을 제작하는데 중요한 정보로 활용될 것이다.

This dissertation was based on

Research funds:

International Scientific Journals:

1. Tae-Young Kim, Jae-Wook Lee, En-Mei Jin, Ju-Young Park, **Jung-Hun Kim**, Kyung-Hee Park, **In situ measurement of dye adsorption on TiO$_2$ thin films for dye-sensitized solar cells**, *Measurement*, Volume 46, Issue 5, June 2013, Pages 1692-1697, ISSN : 0263-2241, I/F: 1.526 (SCI-E)

2. **Jung-Hun Kim**, Tae Young Kim, Kyung-Hee Park, Jae-Wook Lee, **Electron lifetimes in hierarchically structured photoelectrodes biotemplated from butterfly wings for dye-sensitized solar cells**, *International Journal of Electrochemical Science*, Volume 10, 27 May 2015, Pages 5513 −5520, ISSN : 1452-3981, I/F: 1.956 (SCI-E)

3. **Jung-Hun Kim**, Woo-Hyeon Cho, Yong-Min Song, Tae-Young Kim, Kyung-Hee Park, Jae-Wook Lee, **Light harvesting over wide range of wavelengths by rainbow dye-sensitized solar cells**, *Journal of Nanoscience and Nanotechnology*, Volume 16, Number 2, February 2016, Pages 1553-1557, ISSN : 1533-4880, I/F: 1.339 (SCI)

Chapter 1. Introduction

1.1. Global Warming And Greenhouse Gases

Beginning in the 18th and 19th centuries with the Industrial Revolution in Great Britain, humankind has been in a period of full-scale industrialization. This industrialization has dramatically increased greenhouse gas emissions, causing the Earth's surface temperature to increase exponentially in the 21st century. In response, the Intergovernmental Panel on Climate Change (IPCC) has been established to assess the risk of climate change and to establish international measures to mitigate it. According to the IPCC, the planet's average temperature has increased by 0.85°C since the pre-industrialization year 1880, and the sea level has increased by approximately 19 cm. However, if greenhouse gas emissions remain at present levels, the Earth's average temperature will be 3.7°C higher than the present value in 2100, and the sea level has been estimated to rise by a whopping 63 cm. The increases in the average temperature and sea level are blamed for the many natural disasters that have occurred recently, such as floods, storms, droughts, and other extreme weather events. Predictions of the future increases in the average temperature suggest that the occurrence of severe natural disasters may increase four-fold. Experts have determined that humanity will be able to adapt to a temperature increase that is less than 2°C lower than presently forecasted value, which is similar to the 1.7°C increase from the onset of industrialization to the present. Accordingly, international conferences aiming at reducing greenhouse gas emissions and addressing issues surrounding global climate change have been ongoing. In 1997, 37 major developed countries signed the Kyoto Protocol, pledging emission reductions; this agreement is the most widely adopted climate change agreement to date. The period of global greenhouse gas emission reductions set forth by the Kyoto Protocol can be divided into two equal commitment periods: 2008 to 2012 and 2013 to 2020. One of the goals of the first period was to create a new response system [1]. However, this goal has not been implemented properly and has thus extended into the second period. The existing Kyoto system has a number of limitations. First, the United

States did not participate. Second, many of the greenhouse gas emissions of developing countries, such as China and India, were omitted. Finally, Canada, Russia, Japan, and New Zealand may decide to leave the protocol starting in the second transitional period. As a result, at the 17th Conference of the Parties (COP17), held in Durban, South Africa, in 2011, it was concluded that there is a need for an all-encompassing system for reducing greenhouse gas emissions that involves all of humanity, but not all countries were in agreement. Accordingly, a total of 193 countries, including all UN member states, are participating in COP21 discussions on climate change up to 2020, which ended on March 12, 2015, in Paris, France. In these talks, a proposal for the voluntary greenhouse gas reductions by all 193 countries, including all UN member states, was put forward in terms of intended nationally determined contributions (INDCs). The Kyoto Protocol and the Paris Agreement differ in terms of the following key points:

Table 1.1. Kyoto Protocol and Paris Agreement

	Kyoto Protocol	Paris Agreement
Scope	Focus on reducing greenhouse gas emissions	Comprehensive response, including reductions
		Reductions, adaptation, financing, technology transfer, capacity building, transparency
Reduction target station	37 developed countries and the European Union	All developed and developing countries.
	United States, Russia, Japan, Canada, New Zealand absent	
Means of setting reduction targets	Top-down	Bottom-up
Implementation period	First commitment: 2008 ~ 2012	After 2012
	Second commitment: 2013 ~ 2020	

Source: Ministry of the Environment 15. 11. 30

The Paris Agreement has launched greenhouse gas emission reduction efforts throughout the world. As the seventh-highest emitter of greenhouse gases, South Korea was assigned a reduction target of 37% of business as usual (BAU) by 2030. BAU is defined as a scenario in which no restrictions or reduction efforts were implemented and is thus based on assumptions and expectations. South Korea proposed an INDS commitment to reduce greenhouse gas emissions by 37% of the BAU value by 2030. To achieve this target, fossil fuels must be replaced by alternative energy resources in every industry. The replacement of nuclear power by renewable energy is being discussed as a possibility. The International Energy Agency, the largest energy-related organization, defines renewable energy as energy that is constantly supplied by nature. Thus, renewable energy resources can be obtained from a variety of sources, including indirectly from the Earth's core (e.g., geothermal energy) or directly from the sun. Specifically, electrical and thermal energy obtained from sun, wind, ocean, hydropower, biomass, geothermal, biofuels, etc., are classified as renewable energy [1].
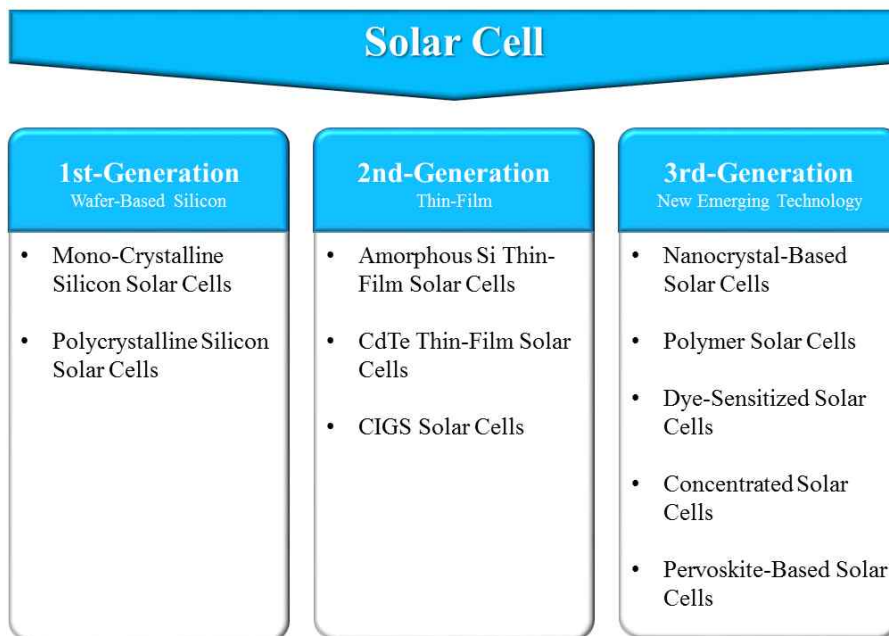
Figure 1.1. Various solar cell technologies and current development trends.

1.2. Solar Cells

The photovoltaic effect was first recognized by French physicist Alexandre-Edmond Becquerel in 1839 [2], and the modern (silicon-based) solar cell was invented by Russel Ohl in 1946 [2, 3]. In modern photovoltaic technology, each cell is composed of two different layers of semiconductor material (p-type and n-type) [4]. In this arrangement, when a photon of appropriate energy impinges on the p-n junction, it provides an electron with sufficient energy to eject the electron, and the electron then moves from one layer to another [4]. This process creates an electron and a hole and generates electrical power [4].

The materials used in photovoltaic solar cells are mainly based on silicon (single-crystal, multi-crystalline, amorphous) [5-7], cadmium telluride [5, 6], copper indium gallium selenide (CIGS) [5, 6, 8], and copper indium gallium sulfide [4, 9]. Photovoltaic solar cells are categorized into various classes, as discussed in the following sections (also shown in Figure 1.1).

1.2.1. First-Generation Solar Cell

The oldest first-generation (wafer-based) solar cells are fabricated on silicon wafers. This technology is the most widely used due to its high efficiencies. Silicon-wafer-based solar cells are divided into two subgroups: those based on mono-crystalline silicon (single-crystalline silicon) and those based on polycrystalline silicon (multi-crystalline silicon) [4-6, 9, 10].

1.2.1.1. Mono-Crystalline Silicon Solar Cell (Single-Crystalline Silicon Solar Cell)

Mono-crystalline solar cells are manufactured from single-crystalline silicon by the Czochralski process [4, 11, 12], which is a method for growing crystals that is used to obtain single crystals of semiconductors [13]. During the manufacturing process, Si crystals

are sliced from very large ingots. Obtaining high-quality single crystals requires precise processing, as recrystallizing the cell is expensive and labor-intensive. The efficiency of mono-crystalline silicon solar cells is 17 ~ 18% [8].

1.2.1.2. Polycrystalline Silicon Solar Cell (Multi-Crystalline Silicon Solar Cell)

Polycrystalline photovoltaic modules are commonly composed of a number of different crystals, coupled to one other in a single cell. The processing of polycrystalline Silicon solar cells is more economical, which are produced by cooling a graphite mold filled containing molten silicon. Polycrystalline silicon solar cells are currently the most popular solar cells. They are believed to charge most up to 48% of the solar cell production worldwide during 2008 [14]. During solidification of the molten silicon, various crystal structures are formed. They are slightly cheaper to fabricate compared to monocrystalline silicon solar panels. The efficiency is approximately 12 ~ 14% [15].

1.2.2. Second-Generation Solar Cells

Most a-Si and thin-film solar cells are second-generation solar cells and are more economical than first-generation silicon solar cells. Silicon cells feature light-absorbing layers up to 350 μm thick, while thin-film solar cells have a very thin light absorbing layers, generally ~1 μm in thickness [16]. Thin-film solar cells are classified as a-Si, CdTe, or CIGS [4].

1.2.2.1. Amorphous Silicon (a-Si) Thin-Film Solar Cell

Amorphous (uncrystallized) silicon thin-film solar cells offer cell efficiencies of 4 ~ 7%. Amorphous silicon exists in several varieties, including amorphous silicon carbide (a-SiC), amorphous silicon germanium (a-SiGe), microcrystalline silicon (μc-Si), and amorphous silicon-nitride (a-SiN). Yang et al. discussed the advances made in a-Si PV technology that led to the achievement of a stable cell efficiency and provided the foundation for the manufacturing of spectrum splitting multi-junction devices by the roll-to-roll continuous deposition process [17]. Lund et al. reported on laboratory and field studies on the nature of the Staebler-Wronski effect (SWE) in a-Si:H solar cells and how the stability of these cells is affected by their operating conditions [18]. Tawada et al. developed a series of production technologies for stable 8% efficiency direct-super-straight-type modules along with large-area monolithic amorphous silicon pin single-junction cells on 910 mm × 455 mm glass substrates [19].

1.2.2.2. Cadmium Telluride (CdTe) Thin-Film Solar Cell

Cadmium telluride (CdTe) thin-film solar cells are among the leading candidates for the development of cheaper solar cells. Cadmium telluride thin-film solar cells are economically viable photovoltaic devices and constitute the first low-cost photovoltaic technology [8, 20, 21]. Cadmium telluride has a band gap of ~ 1.5 eV, a high optical absorption coefficient,

and chemical stability. These properties make CdTe an extremely attractive material for designing new devices. CdTe is an excellent direct band gap crystalline semiconductor, as it facilitates light absorption and improves the efficiency. These solar cells are generally constructed by sandwiching between cadmium sulfide layers to form a p-n junction diode. The manufacturing process involves three steps. First, the CdTe-based solar cells are fabricated from polycrystalline materials using glass as a substrate. In the second process, deposition, the multiple layers of CdTe solar cells are coated onto the substrate using different economical methods. As previously mentioned, CdTe has an optimum direct band gap (~ 1.45 eV) with a high absorption coefficient (over 5 sorp[15]/cm) [22]. Therefore, its energy conversion efficiency is usually 9 ~ 11% [8, 23]. CdTe solar cells can be fabricated on flexible polymer substrates. However, the cadmium component of these solar cells poses various environmental issues. Cadmium is regarded as a heavy metal and a potential toxin that can accumulate in humans, animals, and plants. The disposal toxic Cd-based materials as well as their recycling can be highly expensive and damaging to the environment and society [9]. The limited supply of cadmium and the environmental hazard associated with its use are the main disadvantages of these solar cells [21-24].

1.2.2.3. Copper Indium Gallium Diselenide (CIGS) Solar Cells

CIGS is a quaternary semiconductor composed of copper, indium, gallium, and selenium [9]. CIGS is also a direct band gap semiconductor. Compared to CdTe thin-film solar cells, CIGS has a higher efficiency (10 ~ 12%). Due to their significantly high efficiency and economy, CIGS-based solar cells are one of the most viable thin-film technologies. The processing of CIGS is achieved by the following techniques: sputtering, evaporation, electrochemical coating, printing, and electron beam deposition [4, 25]. In addition, sputtering can be a two- or multi-step process involving deposition and subsequent interaction with selenium or a one-step reactive process instead. Meanwhile, evaporation is similar to sputtering in that it can be performed in one or more processing steps. The substrates for CIGS may include glass plates, polymer substrates, steel, and aluminum, among others. The advantages of CIGS thin-film solar cells include a prolonged life

without considerable degradation. These properties of CIGS provide an easy solution to enhancing the efficiency [8, 23, 26]. Table 1 shows a comparison of popular wafer-based solar cells and thin-film solar cells [4, 11].

1.2.3. Third-Generation Solar Cells

Third-generation cells are a promising new technology but have not been widely commercialized. Most of the developed third-generation solar cells are nanocrystal-based, polymer-based, dye-sensitized, or concentrated solar cells [10].

1.2.3.1. Nanocrystal-Based Solar Cells

Nanocrystal-based solar cells are also known as quantum dot (QD) solar cells. These solar cells are composed of a nanocrystal-sized semiconductor, generally a transition metal. The term "QD" refers to materials with crystals of a few nanometers in size, for example, porous Si or porous TiO_2 [27]. With the advance of nanotechnology, these nanocrystals of semiconducting material are expected to replace semiconducting material in the bulk state, such as Si, CdTe, or CIGS. This concept of QD-based solar cells with a theoretical formulation was employed for the design of a p-i-n solar cell over a self-organized As/GaAs system [27]. Generally, the nanocrystals are mixed in a bath and coated onto the Si substrate. These crystals rotate very fast and flow away due to centrifugal force. In conventional semiconductor solar cells, a photon excites an electron by creating an electron-hole pair [28]. However, when a photon strikes a QD made of these semiconductor materials, numerous electron-hole pairs can be formed: usually 2 or 3, but the formation of 7 pairs has been observed in a few cases [10, 24].

1.2.3.2. Polymer Solar Cells

Polymer solar cells (PSCs) are generally flexible due to the flexibility of their polymer substrates. The first PSC was developed by Tang et al. [10]. A PSC is composed of serially connected thin functional layers coated on a polymer foil or ribbon. It usually works as a combination of a polymer (donor) and a fullerene (acceptor). Various materials are used for the absorption of sunlight, including organic materials, such as a conjugate/conducting polymers [10, 29]. In 2000, Heeger, MacDiarmid, and Shirakawa were

awarded the Nobel Prize in Chemistry for the discovery of a new category of polymer materials known as conducting polymers [30, 31]. The PSC and other organic solar cells operate on the principle of the photovoltaic effect, in which electromagnetic radiation is transformed into electrical current [32]. Yu et al. mixed poly[2-methoxy-5-(2'-ethylhexyloxy)-p-phenylene vinylene] (PPV), C60, and its derivatives to develop the first polymer solar cell and obtained a high power conversion efficiency [33]. This process triggered the dawn of a new age in the use of polymer materials to capture solar energy. After substantially optimizing the parameters, researchers achieved an efficiency of over 3.0% for PPV-type PSCs [33-35]. The unique properties of PSCs enabled the development of stretchable solar devices, including textiles and fabrics [34]. A modern recycling concept known as polarizing organic photovoltaics (ZOPVs) was also developed to increase the applicability of liquid crystal displays utilizing the same polarizer, a photovoltaic device, and proper light conditions/solar panels [34-36].

1.2.3.3. Dye-Sensitized Solar Cells (DSSC)

Recent research has focused on improving solar efficiency by molecular manipulation and the use of nanotechnology for harvesting light energy [37-40]. The first dye-sensitized solar cell (DSSC) was introduced by Gratzel [4, 9]. DSSCs generally employ dye molecules between the electrodes. A DSSC consists of four components: a semiconductor electrode (n-type TiO_2 and p-type NiO), dye sensitizer, redox mediator, and counter electrode (carbon or Pt) [41]. DSSCs are attractive due to their simple and conventional processing methods, such as printing techniques, as well as their high flexibility, transparency, and low cost [9]. The novelty of DSSCs is based on the photosensitization of nanograined TiO_2 coatings coupled with visible optically active dyes, increasing the efficiencies by more than 10% [37-39, 41, 42]. However, certain challenges remain, such as degradation of the dye molecules, which creates stability issues [9]. This is due to the poor optical absorption of sensitizers, which results in poor conversion efficiency. The dye molecules generally degrade after exposure to ultraviolet and infrared radiation, leading to a decrease in the lifetime and stability of the cells. Moreover, coating with a barrier layer may also increase

the manufacturing costs and lower the efficiency [8].

1.2.3.4. Concentrated Solar Cells

Concentrating photovoltaics (CPVs) were first developed in the 1970s [40, 43, 44] and represent the newest technology in solar cell research and development. The main principle of concentrated cells is to collect a large amount of solar energy onto a tiny region within the PV solar cell. The principle of this technology is based on optics, using large mirrors and lens arrangements to focus sunlight onto a small region on the solar cell [8]. The convergence of the sunlight radiation thus produces a large amount of heat energy. This heat energy is further driven by a heat engine controlled by a power generator with integrated. CPVs have shown promise in the solar world [44, 45]. These devices can be classified into low-, medium-, and high-concentrated solar cells depending on the power of the lens systems [44]. CPV technology such merits as solar cell efficiencies > 40%, the absence of moving parts, no thermal mass, low response times, and high scalability.

1.2.3.5. Perovskite Based Solar Cell

Perovskites are a class of compounds defined by the formula ABX_3 where X represents a halogen (such as I^-, Br^-, or Cl^-) and A and B are cations of different sizes. Perovskite solar cells are a recent discovery within the solar cell research community and possess several advantages over conventional silicon- and thin-film-based solar cells. Conventional Si-based solar cells require expensive, multi-step processing, including high temperatures (> 1273 K) and vacuum facilities [46]. Perovskite-based solar cells can have efficiencies of up to 31% [47]. An investigation recently performed by Volkswagen suggests that these perovskites may also play an important role in next-generation electric automobile batteries [47]. However, perovskite solar cells currently suffer from poor stability and durability. The material degrades over time, decreasing the overall efficiency. Therefore, more research is needed to bring these cells to the marketplace.

Table 1.2. Comparison of various types of solar cells

Cell type		Efficiency
Crystalline silicon	Monocrystalline	14 ~ 17.5%
	Polycrystalline	12 ~ 14%
Thin film	CdTe	9 ~ 11%
	CIGS	10 ~ 12%
	Amorphous silicon	4 ~ 8%
Third Generation	Nanocrystal	7 ~ 8%
	Dye-sensitized	≈10%
	Polymer	≈3 ~ 10%
	Concentrated	≈40%
Perovskite		31%

1.3. DSSC Components

1.3.1. Transparent Conductive Oxide (TCO)

Transparent conductive oxide (TCO) substrates must be highly transparent (transparency > 80%) to allow the maximum passage of sunlight to the active area [48]. Typically, DSSCs are constructed from two sheets of TCO material as current collectors for the deposition of the semiconductor and catalyst. The characteristics of the TCO material determine the efficiency of the DSSC [49] because the efficiency of the charge transfer process determines the energy loss. Fluorine tin oxide (FTO, SnO_2:F) and indium tin oxide (ITO, In_2O_3:Sn) are typical conductive oxide substrates consisting of soda lime glass coated with fluorine tin oxide or indium tin oxide, respectively. The transmittance of ITO films is over 80% in the visible region, with a sheet resistance of approximately 18 Ω/cm^2, whereas FTO films exhibit a transmittance of approximately 75% with a sheet resistance of 8.5 Ω/cm^2 [48]. Sima et al. conducted a study based on FTO and ITO glass substrates sintered at 726 K [50]. They found that upon sintering, the sheet resistance of ITO increased from 18 Ω/cm^2 to 52 Ω/cm^2, while that of FTO remained constant. The overall conversion efficiencies (η) of DSSCs based on FTO and ITO are approximately 9.4% and 2.4%, respectively. Thus, FTO is strongly recommended for use in DSSC fabrication due to its conduction properties and stable sheet resistance temperature.

Murakami et al. used a polyethylene terephthalate (PET) polymer substrate coated with ITO and obtained a conversion efficiency of approximately 3.8% [51]. Meanwhile, Ito et al. reported an efficiency of 7.8% using polyethylene naphthalate (PEN) [52]. Polymer substrates are attractive alternatives due to their flexibility and low cost. Nevertheless, the use of polymer substrates in DSSCs limits their viability due to the requirement of a relatively low fabrication temperature. Another alternative is the use of metals, such as stainless steel, tungsten, and titanium, as conducting layer substrates. Jun et al. reported an efficiency of 6.1% [53] using a stainless steel substrate. However, the high cost and corrosion caused by the electrolyte restrict the use of metals as substrates. Launching a

new research trend, Braga et al. demonstrated the reliable front contact of cadmium stannate (CTO) and titanium dioxide (TiO$_2$) deposited entirely by magnetron sputtering. The CTO contact results in a high optical transmittance of approximately 90% along with a sheet resistance of 15 Ω/cm^2 [54].

1.3.2. Semiconductor Oxide Material

The central part of a DSSC device is a thick nanoparticle film that provides a large surface area for light-harvesting molecules to accept electrons from the excited dye [55], such as TiO$_2$, ZnO [56], SnO$_2$ [57], Nb$_2$O$_5$, WO$_3$, Ta$_2$O$_5$, CdSe, CdTe, and CdS. These molecules are interconnected to allow electronic conduction [58]. The efficiency of DSSCs depends on the electron transfer rates, which in turn depends on the crystallinity, morphology, and surface area of the semiconductor. However, previous research has shown that DSSCs based on ZnO and SnO$_2$ exhibit lower efficiencies than those based on nanocrystalline TiO$_2$ [57, 59, 60] due to the latter's superior morphological and photovoltaic properties [61]. TiO$_2$ is considered by some to be the most efficient and environmentally benign photocatalyst [62]. Bulk TiO$_2$ is dominated by three main phases: rutile, anatase, and brookite [63]. Anatase TiO$_2$ is preferred due to its high conduction band edge energy (3.2 eV), which provides chemical stability. In comparison, the conduction band edge energy of rutile TiO$_2$ is approximately 3 eV. In rutile TiO$_2$, electron transport is hindered by the high packing density, and for the same film thickness, anatase-based DSSCs produce a 30% [50] higher short-circuit current than rutile-based DSSCs.

Recent trends in research have involved the fabrication of anatase TiO$_2$ as nanoparticles, nanofibers [64], nanowires [65], hollow spheres [66], hollow hemispheres [67], nanotubes [68], and hierarchical spheres [69] and ellipsoid spheres [70] via the solvothermal reactions of titanium n-butoxide and acetic acid. The one-dimensional (1D) nanostructure of TiO$_2$ nanowires has also attracted considerable attention in terms of its application to DSSCs. A novel method involving hydrothermal growth has been reported for the synthesis of a TiO$_2$ nanowire array on FTO glass substrates [71]. TiO$_2$ nanowires in a standard DSSC configuration exhibited a conversion efficiency of approximately 5%, which is considerably

higher than the value of 1.2 ~ 1.5% attained by ZnO nanowires with lengths of up to ~ 40 μm [71]. Anatase TiO_2 spheres have an overall η of 3.5% with a current density I_{sc} of 17.94%, open circuit voltage V_{oc} of 803 mV and FF of 0.65%. This η value is much lower than those of DSSCs based on nanoparticles (7.37%), nanofibers (8.15%), and ellipsoid TiO_2 spheres (7.93%) [72]. The superior η and I_{sc} of the hierarchical sphere-based DSSCs are a result of higher dye loading, improved light-scattering ability, faster charge transfer, and longer electron lifetime [73, 74]. To produce higher η and I_{sc}, several strategies are used to minimize electron-hole recombination. These approaches include the deposition of an insulating layer on the semiconductor electrode. ZnO [75], niobium pentoxide (Nb_2O_5) [76], Al_2O_3 [77], and SiO_2 [78] have been used as energy barriers to slow charge recombination due to their insulating character, which reduces the interaction between the electrons injected into the semiconductor and the electrolyte solution [79]. The surface treatment of TiO_2 with $TiCl_4$ also reduces charge recombination by increasing the interfacial charge transfer resistance of the TCO/electrolyte interface [80, 81], as demonstrated by Melhem et al. I_{sc} was up to 10% higher when using DSSCs based on an N-doped electrode compared to the pure anatase configuration [82]. This improvement is associated with the electronic and optical properties of the starting nanopowder.

ZnO is an alternative semiconductor oxide material due to its wide band gap, which is similar to that of TiO_2, and its ability to be synthesized in a simple manner and with different nanostructures. Recently, Keis et al. achieved a conversion efficiency of ~5% under illumination (10 mW/cm^2) with a porous ZnO electrode prepared using the high-pressure compression method and Ru complexes with a carboxylate polypyridine ligand [83]. The advantages of ZnO over TiO_2 include the following [58]: (i) a direct band gap of approximately 3.37 eV, (ii) a higher excitation binding energy (60 meV) compared with TiO_2 (4 meV), and (iii) higher electron mobility (200 cm^3/V s) compared with TiO_2 (30 cm^3/V s). The grain size of ZnO is overly large, and its effective surface area is insufficient; hence, the efficiency of ZnO is low. Therefore, the key to improving the performance of ZnO-based DSSCs is the preparation of a nanoporous ZnO film. Law et al. first reported the use of ZnO nanowire arrays in DSSCs with the aim of replacing the traditional nanoparticle film to increase the electron diffusion length [84]. ZnO nanowire-based DSSCs have been reported to achieve a conversion efficiency of 0.5% and

an internal quantum efficiency of 70% due to their high surface area and good connectivity to the electrode. Compared with TiO$_2$, the similar electron mobility and conduction band energies of ZnO, in combination with its high excited-state binding energy, make it a promising candidate for lasing devices and stable room-temperature luminescence [85]. Thus, ZnO nanowires are an alternative material for high-efficiency DSSCs.

1.3.3. Dye Sensitizer

An efficient solar cell sensitizer should adsorb strongly to the surface of the semiconductor oxide via anchoring groups, exhibit intense absorption in the visible region of the spectrum, and possess an appropriate energy level alignment between the dye excited state and the conduction band edge of the semiconductor. The performance of DSSCs mainly depends on the molecular structure of the photosensitization. Sensitization of the semiconductor in DSSCs has been achieved using numerous chemical compounds, such as phthalocyanines [86-88], coumarin 343 (C343) [69, 89], carboxylated derivatives of anthracene [90, 91], and porphyrins [92-94]. However, the best photosensitization has been attained using transition metal materials [95]. Three classes of dye sensitizers are used in DSSCs: metal complex sensitizers, metal-free organic sensitizers, and natural sensitizers.

Ru(II) is the most efficient dye due to its numerous advantageous features, such as good absorption, long excited-state lifetime, and highly efficient metal-to-ligand charge transfer. Ru bipyridyl complexes are excellent photosensitizers due to the stability of their excited states and the long-term chemical stability of oxidized Ru(III) [96]. The standard dye used in traditional DSSCs is tris(2,2'-bipyridyl-4,4'-carboxylate) ruthenium (II) (N3 dye) [97]. N3 and N719 dyes contain four and two photons, respectively, and have been reported to successfully absorb solar light and undergo charge transfer. Another promising candidate is tri(cyanato-2,2'2,2''-terpyridyl-4,4',4''-tricarboxylate) Ru (II) (black dye), whose response extends approximately 100 nm further into the infrared (IR) region than the response of the N3 dye [97]. Therefore, many researchers have studied Ru bipyridyl complexes as photosensitizers for the reactions of homogeneous photocatalytic and dye-sensitization systems. However, these complexes also have disadvantages, including high cost and the

need for sophisticated preparation techniques.

Coumarin is a synthetic organic dye sensitizer obtained from a natural compound found in many plants. C343 is an excellent organic-dye photosensitizer for efficient electron injection into the conduction band of semiconductors. However, the efficiency η for nanocrystalline DSSCs based on the C343 dye is lower than those of DSSCs based on Ru-complex photosensitizers because of a lack of absorption in the visible region [89].

Table 1.3. Various types of plant pigmentation [98]

Plant Pigment	Common Types	Occurrence
Betalains	Betacyanins	Caryophyllales and betaxanthins some fungi
	Betaxanthins	
Carotenoids	Carotenes	Photosynthetic plants and bacteria
	Xanthophylls	Retained from the diet by some birds, fish, and crustaceans
Chlorophyll	Chlorophyll	All photosynthetic plants
Flavonoids	Anthocyanin	Widespread and common in plants including angiosperms, gymnosperms, ferns, and bryophytes
	Aurones	
	Chalcones	
	Flavonols	
	Proanthocyanidins	

Natural dyes are a viable alternative to expensive organic-based DSSCs. The overall solar energy conversion efficiency of natural dyes extracted from pigments containing anthocyanins and carotenoids has been demonstrated to be less than 1% [99]. Different parts of the plant, including the flower petals, fruits, leaves, stems, and roots, typically have different pigments. The advantages of natural dyes are their low cost, easy extraction, non-toxicity, and environmentally benign nature [100]. The orange-red lawsone, red-purple anthocyanin (sensitization of wide-bandgap semiconductors) [101], and yellow curcumin are the main components in the natural dyes obtained from these natural products [102]. Plant pigmentation occurs due to the electronic structure of the pigments, and exposure to

illumination modifies the wavelengths that are either transmitted or reflected by the plant tissue. Table 1.3 describes the plant pigmentation groups based on a common structure and biosynthesis basis.

Table 1.4. Photoelectrochemical parameters of DSSCs sensitized by various natural dyes [99, 105-107]

Dye Sensitizer	J_{sc} (mA/cm^2)	V_{oc} (V)	Fill Factor	Efficiency
Wormwood	0.196	0.585	0.47	0.538%
Purple Cabbage	0.208	0.660	0.53	0.75%
Turmeric	0.288	0.529	0.48	0.03%
Lemon Leaves	0.272	0.537	0.05	0.05%
Morinda Lucida	0.256	0.440	0.47	0.53%
Wild Silican Prickly Pear	7.320	0.400	0.41	1.21%
Red Turnip	9.500	0.450	0.37	1.70%
Bougainvillea	2.100	0.300	5.7	0.36%

Carotenoid pigments are obtained from fruits and plants with distinctive red, orange, and yellow colors and carotenoid-derived aromas. The skeleton of carotenoids may be linear or may contain cyclic end groups, and the major two classes consist of carotenes and their oxygen-generated derivatives, xanthophylls [103]. In addition, carotenoids also provide protection from excess light through the dissipation of energy and free radical detoxification, limiting the damage to the membrane. Flavonoids and their conjugates form a large group of natural products. These components have been observed in many plant tissues, where they can be found inside the cells or on the surfaces of different types of plant organs. The three major classes of flavonoid compounds are anthocyanins, proanthocyanidins, and flavonols. Anthocyanins do not display vivid colors until they are grouped together in acidic vacuoles. Some of the flavonols have protective roles as UV-B filters and function as co-pigments for anthocyanin, especially for special tissues.

The achievement of wide-bandgap semiconductor sensitization using natural pigments is typically attributed to anthocyanin. Anthocyanins comprise a major flavonoid group that is responsible for cyanic colors ranging from salmon pink to red and dark violet to dark blue in most flowers, fruits, and leaves of angiosperms [103]. The anthocyanin molecule possesses carboxyl and hydroxyl groups and occurs in fruit, leaves, and flowers, where it is responsible for colors ranging from visible red to blue [104]. The bonding causes the electron to move from the anthocyanin molecule to the conduction band of TiO_2. Anthocyanins are often used in organic solar cells due to their ability to absorb light and convert it into electrons. Table 1.4 describes the performances of various types of natural dyes used as photosensitizers in DSSCs.

1.3.4. Electrolyte

Electrolytes are used to regenerate the dye after electron injection into the conduction band of the semiconductor and act as a charge transport medium for the transfer of positive charge toward the counter electrodes [48]. The liquid electrolyte is based on an organic solvent with a high ionic conductivity and distinctive interfacial contact properties; nevertheless, the leakage and volatility of the solvent affect the long-term performance of DSSCs [103]. Therefore, the electrolyte must have the following characteristics [108, 109]: (i) high electrical conductivity and low viscosity for faster electron diffusion; (ii) good interfacial contact with the nanocrystalline semiconductor and counter electrode; (iii) no tendency to induce the desorption of the dye from the oxidized surface or dye degradation; and (iv) no absorption of light in the visible region.

A liquid electrolyte consists of a solvent, a redox couple (the most important component), and one or more additives. Other redox couples used include I^-/I_3^-, Br^-/Br_2 [110], $(SCN)_2/SCN^-$, $(SeCN)_2/SeCN^-$ [111, 112], and bipyridyl cobalt (III/II) complexes [113], which have also been investigated for use in DSSCs [114]. Generally, the liquid electrolyte used in DSSCs contains I^-, I^-/I_3^-, and I_3^- redox ions as mediators between the TiO_2 photoelectrode and counter electrode. Compared with I^-/I_3^-, the other redox couples exhibit lower DSSC light-to-electricity conversion efficiencies because the energy cannot be

matched with the sensitized dye or as a result of their intrinsically low diffusion coefficients in the electrolyte [114].

There are two types of solid-state DSSCs: one using a hole transport material (HTM) as the medium and one using a solid-state electrolyte containing an I^-/I_3^- redox couple as the medium. A solid-state device has recently been described in which the liquid electrolyte based on a porous nanocrystalline oxide film is replaced by a wide-bandgap p-type semiconductor as a medium for hole transport [103]. The solid-state device containing a p-type semiconductor has advantages over all solid-state cells due to its easy preparation and higher stability, whereas solar cells occupied with polymer electrolytes exhibit a higher efficiency and have additional future practical applications with proper encapsulation [103]. Organic and inorganic electron HTMs cannot be used as a transport material in DSSCs for practical applications due to their low power conversion efficiencies [114].

1.3.5. Counter Electrode

Counter electrodes are mainly used to regenerate the electrolyte, with the oxidized electrolyte diffusing towards the counter electrode [48]. The counter electrode transports the electron that arrives from the external circuit back to the redox electrolyte system. Hence, for efficient charge transfer, the counter electrode should exhibit a high catalytic activity and high electrical conductivity [115]. Thus, the catalyst must accelerate the reduction reaction. On this basis, platinum (Pt) is considered a preferred catalyst. Pt is a superior catalyst for use as a counter electrode for I_3^- reduction because of its high exchange current density, good catalytic activity, and transparency. The performance of the counter electrode depends on the method of Pt deposition on TCO substrates, such as the thermal decomposition of hexachloroplatinic acid in isopropanol [116], electrodeposition [117], sputtering [118], vapor deposition [119], and screen-printing.

However, Pt is a rare and expensive metal, and some researchers have reported that Pt erodes via reaction with I_3^- in the electrolyte to form PtI_4 [120]. The Pt catalytic activity was reported to decrease upon exposure to the dye solution and in the presence of I^-/I_3^- redox couples [121], likely because its surface is blocked by the adsorbed dye. The major

causes of the deactivation of a Pt counter electrode are the alteration of its electrocatalytic properties and the removal of Pt from substrates [116], as demonstrated experimentally. Therefore, carbon, graphene, and conductive polymers have also been used as counter electrodes [122].

Carbon is an interesting low-cost alternative because it offers sufficient conductivity and heat resistance in addition to corrosion resistance and electrocatalytic activity for I_3^- reduction [123]. Carbonaceous materials exhibit numerous advantageous features, such as high electronic conductivity, corrosion resistance toward I_3^- reduction, and low cost as substitutes for Pt. In 1996, Kay et al. reported the use of carbon black as a counter electrode, resulting in a conversion efficiency of approximately 6.7% [120]. Josef et al. demonstrated the substitution of a Pt catalyst with a nanocomposite of dry-spun carbon multi-walled nanotube (MWNT) sheets with graphene flakes (Gr-F) in a DSSC, reporting an improvement in the catalytic behavior and power conversion efficiency (7.55%) relative to MWNTs alone (6.62%) or graphene alone (4.65%) [124]. The latest study by Arman et al. used a Pt-multi-walled carbon nanotube (MWCNT) counter electrode to obtain a current density J_{sc} of 17.2 mA/cm^2, open-circuit voltage V_{oc} of 0.690 V, and efficiency η of 8.6%, which is the highest photovoltaic performance to date [125]. Table 1.5 shows the performance of the various counter electrodes.

Table 1.5. Photoelectrochemical parameters of DSSCs with different counter electrodes [125]

Counter Electrode	J_{sc} (mA/cm^2)	V_{oc} (V)	Fill Factor	Efficiency, η
Pt	15.3	0.670	0.70	7.2
Pt-MWCNT	17.2	0.690	0.71	8.6
MWCNT	15.1	0.655	0.68	6.7

1.3.6. Application

Building-integrated photovoltaics (BIPV) are one of the fastest growing segments of the photovoltaic industry. Photovoltaic materials may be used to replace conventional building materials in parts of the building envelope, such as the roof, skylights, or facades.

In 2009, G24 Innovations, a DSSC license holder, announced the first-ever commercial shipment of DSSC photovoltaic modules. The first consumer product, backpacks coated with cheap and flexible DSSCs for on-the-go recharging of portable gadgets, was made available in stores in January 2010.

Figure 1.2. Applications of dye-sensitized solar cells.

Although DSSCs are still in relatively early stages of development, they show great promise as a reasonably priced substitute to costly silicon solar cells and an attractive candidate as a new renewable energy source. DSSCs could play an important role in the future of alternative renewable energy.

1.4. Purpose and Outline of This Dissertation

The thesis is arranged into six chapters. This first chapter introduces the thesis and describes the history of global warming and greenhouse gases, the current state of photovoltaics technologies, and the components of DSSCs as well as the outline of this thesis. The overall structure of this thesis is shown in **Figure 1.3**.

Chapter 2 provides the theoretical background of DSSCs. The operating principle of the DSSCs is presented along with the mechanism. In addition, the theoretical basis of DSSC operation is systematically explained. The fundamental physical and chemical processes of the cell operation are discussed. The fabrication of DSSCs is described in this work. Finally, a simple electrochemical model of the DSSC is introduced.

Chapter 3 investigates the photovoltaic properties of TiO_2 electrodes prepared using a mesoporous silica template. In this chapter, hierarchical structures for TiO_2 photoelectrodes, biotemplated from *Parpilio paris* butterfly wings, were synthesized and applied to DSSCs. The adsorption kinetics of N719 dye molecules on thin TiO_2 films was measured and interpreted using a pseudo-second-order model. The morphology of the films plays an important role in their light-harvesting behavior, and hierarchical structures lead to increased absorption. The synthesized samples were characterized by various instrumental analysis techniques. The influence of the properties of the adsorption of N719 molecules onto nanoporous BW-TiO_2 thin-film surfaces on the efficiency of the DSSC was also systematically investigated on the basis of the photovoltaic performance calculated from the *J-V* curves.

Chapter 4 describes the photovoltaic properties of successive DSSCs prepared using synthetic dyes. The preparation of photoelectrodes by a typical successive adsorption method is discussed in this chapter. The adsorption properties of the

prepared photoelectrode toward two dyes (N719 and MK-2) were also investigated. To improve the photovoltaic conversion efficiency, a double layer of the two natural dyes as sensitizers was successfully formulated on the nanoporous TiO_2 surface to harvest light over a wide wavelength range. The adsorption properties of photoelectrodes adsorbed with a single dye were compared with those attained with a mixture of the two dyes.

Chapter 5 addresses the enhanced photovoltaic properties of rainbow DSSCs achieved by natural dye. In this chapter, three natural dyes (yellow, blue, and red) were extracted from gardenia and used as sensitizers in the assembly of rainbow DSSCs to harvest light over a wide wavelength range. The adsorption characteristics, photovoltaic efficiencies, and electrochemical properties of the rainbow DSSCs were investigated. The adsorption kinetics for the dyes were measured in a small adsorption chamber. The data fitted a pseudo-second-order model. The photovoltaic performance of a photoelectrode with an adsorbed mixture of the three dyes was evaluated from current-voltage measurements.

Finally, in **Chapter 6**, overall conclusions are drawn on the basis of the theoretical and experimental results. This thesis includes 114 pages, 36 figures and 16 tables and 198 references.

Chapter 1 — *Introduction*

1. Global Warming And Greenhouse Gases
2. Basics of photovoltaic energy conversion
3. DSSC Components
4. Literature review concerning DSSCs

Chapter 2 — *DSSCs*

1. Operational Principles of DSSCs
2. Theoretical basis of DSSC operation
3. Electrochemical methods

Chapter 3 — *Butterfly wings TiO$_2$*

1. Synthesis of Butterfly Wings TiO$_2$
2. Hierarchically Structured electrode
3. Adsorption properties of Photoelectrode
4. Characterization of BW-TiO$_2$ cells

Chapter 4 — *N719/MK-2 DSSCs*

1. Successive Adsorption Properties of cells
2. Fabrication of Successive Adsorption cells
3. Photoelectrochemical Measurements

Chapter 5 — *Rainbow DSSCs*

1. Adsorption Properties of Rainbow electrode
2. Fabrication of Rainbow DSSCs
3. Characterization of Rainbow DSSCs

Chapter 6 — *Overall Conclusion*

1. Summary of the experimental and theoretical results

Figure 1.3. Thesis structure.

Chapter 2. Dye-Sensitized Solar Cells

2.1. Operational Principles of DSSCs

The operating principle of dye-sensitized solar cells (DSSCs) entails the surface e^- transfer and interfacial dynamics resulting from the ultrafast e^- injection from the molecular excited state into the conduction band of the oxide. The produced dye cations must be intercepted by the oxidized dye prior to recombination with conduction band electrons. This charge transfer between the oxidized dye at the semiconductor surface and the hole transport arbitrator determines the photon-to-current efficiency. At the heart of the system is a mesoscopic semiconductor oxide film, which is placed in contact with an electrolyte or an organic hole conductor [126].
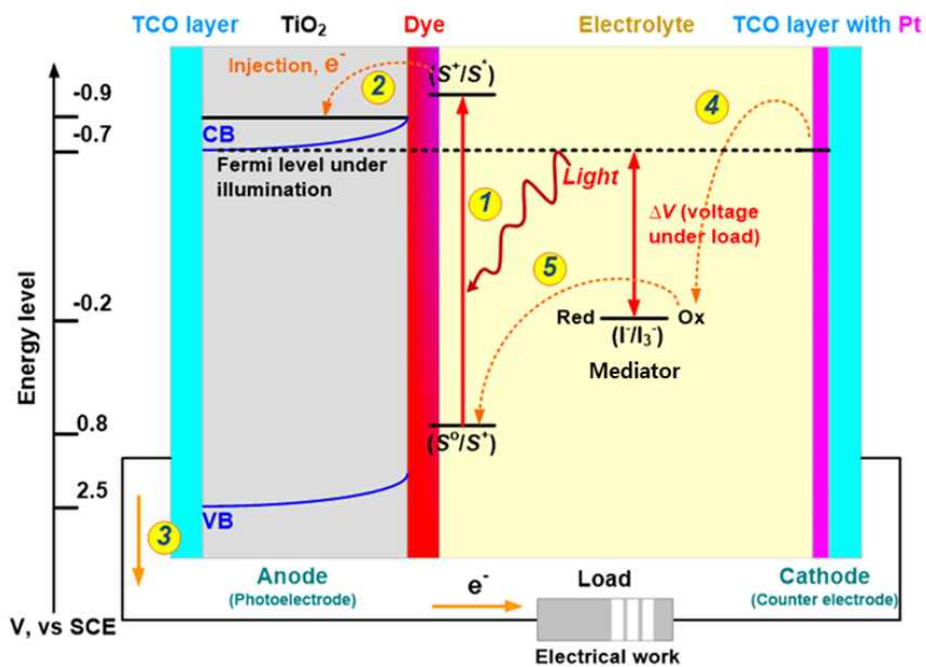
Figure 2.1 Working principle of dye-sensitized solar cells.

As a result, the rate must be sufficiently high to prevent indirect recombination. The photophysical e^- transfer processes taking place at the TiO$_2$/dye/electrolyte interface for state-of-the-art DSSCs are summarized in Figure 2.1 and Equation 2.5.

The regenerative working cycle of the DSSC and the comparative energy levels of a working DSSC are presented schematically in Figure 2.1. The incoming photon is absorbed by the dye molecule adsorbed on the surface on the nanoporous TiO$_2$ particle and an electron from a molecular excited state S* to the nanoporous TiO$_2$ [127].

$$S + h\nu \rightarrow e^- + S^+ \qquad \text{Excitation process} \qquad \text{Equation 2.2}$$

$$S^* + TiO_2 \rightarrow e^- + S^+ \qquad \text{Injection process} \qquad \text{Equation 2.3}$$

$$e^- + C.E \rightarrow TiO_2 + e^- + energy \qquad \text{Energy generation} \qquad \text{Equation 2.4}$$

$$S^+ + \frac{3}{2}I^- \rightarrow \frac{1}{2}I_3^- \qquad \text{Regeneration of dye} \qquad \text{Equation 2.5}$$

$$\frac{1}{2}I_3^- + e^- \rightarrow \frac{1}{2}I^- + C.E \qquad e^- \text{ recapture reaction} \qquad \text{Equation 2.6}$$
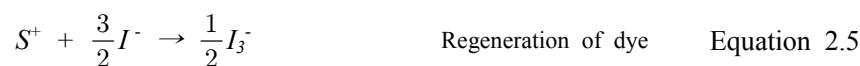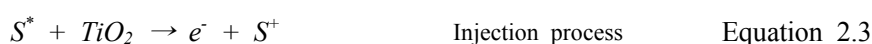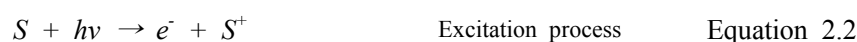
$$\phi_{inj} = \frac{k_{inj}}{k_{inj+k_1}} \qquad \text{Equation 2.7}$$

DSSCs are characterized by excited-state lifetimes typically in the range of excited state Smolecule adsorbed on the surface on the nanoporhich is placed in contact with n the nanoporous TiOce conventefficient charge injection should occur within a sub-picosecond time frame. The lifetimes of the excited state of Ru-complex dyes are usually longer, with sually longerecond time frae^- injection efficiency can be determined by Equation 2.7. The rate constants for e^- injection (k_{inj}) and decay (k_1) were used for the equation. For efficient injection, k_{inj} should be approximately 100 times larger than k_1. The oxidized dye is intercepted by an e^- donor, normally I^-, typically on a μn timescale. In addition, the

charge transport mechanism in nanoparticles is still under debate and is determined by the inherent conductivity, low built-in electrical potential, and many phase boundaries with relatively slow diffusion (ms domain) at the interface of TiO_2, in the bulk of the particles, and/or at grain boundaries, which can serve as e^- traps [127, 128]. To complete the electrical circuit of a DSSC, a Pt-coated counter electrode with an I_3^-/I^- electrolyte should be used for the reduction of e^- acceptors in the electrolyte. At the surface of the counter electrode, triiodide is reduced to iodide [128, 129]:

$$I_3^- + 2e^- \leftrightarrow 3I^-$$ Equation 2.8

A benefit of DSSCs is their imitation of natural photosynthesis, in which the light absorption is separated from the e^- collection. In the DSSCs, the driving force for the transport of ions or electrons is the gradient of the electrochemical potential or free energy. Consequently, knowledge of the kinetics and relative positions of the energy levels at the oxide/dye/electrolyte interface are important for understanding the e^- transfer dynamics in DSSCs [130, 131].

The configuration of the sensitizer, the energy separation gap and the highest occupied molecular orbital (HOMO)/lowest unoccupied molecular orbital (LUMO) level strongly affect the e^- flow. Figure 2.2 presents a schematic illustration of the kinetics in DSSCs. Hagfeldt et al. and Gratzel et al. reported the timescales of each component: relaxation of the excited level, 60 ns; e^- injection from the dye (LUMO) to the TiO_2 (conduction band, CB), 50 fs ~ 1.7 ps; recombination of the electrons with the hole in the dye (HOMO), ns ~ ms timescale; regeneration of the oxidized dye by electrolytes (I^-), 10 ns; recombination of the electrons in the TiO_2 (CB) with a hole in the electrolyte (I_3^-), 10 ms [127].

The electrons injected from the photoexcited dye into TiO_2 pass through the interconnected nanoporous networks to reach the anode. In nanoporous TiO_2, the electrons diffuse to the anode by hopping 10^3 ~ 10^6 times between particles [132]. With each hop, there is a considerable probability of the photoexcited e^- recombining with the electrolyte

because both the diffusion and recombination rates are on the order of milliseconds. This recombination limits the cell efficiency. The excess electric charge of the oxide nanoparticles arising from the injected e^- (from the sensitizer) is balanced by the net ionic charge in the electrolyte. To develop efficient DSSCs, a high quantum efficiency for injection is very important. The e^- injection efficiency is defined as follows [133-135]:
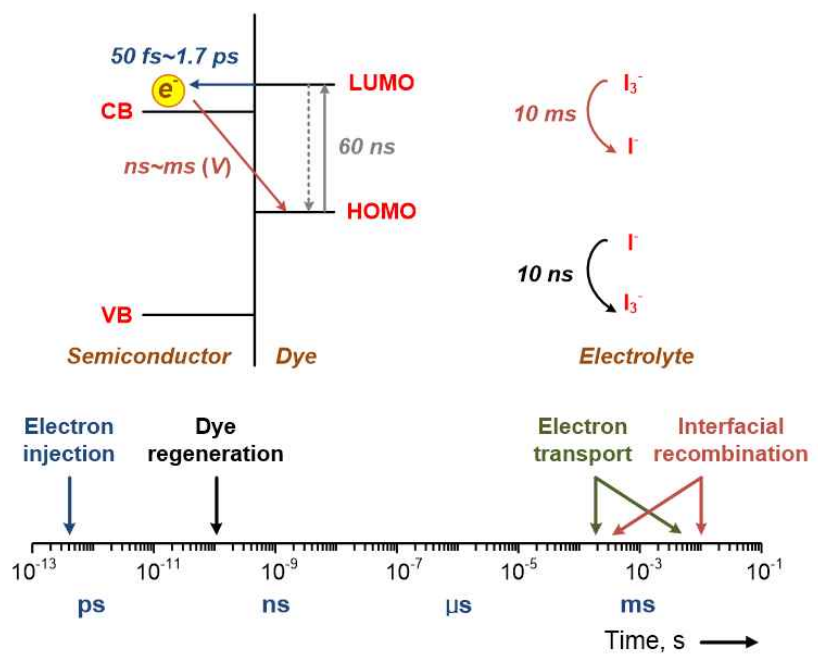
Figure 2.2. Schematic illustration of the kinetics in DSSCs with the electron dynamics timescales [127].

$$\phi_{inj} = \frac{k_{inj}}{k_{inj+k_1}}$$ Equation 2.9

$-$ 29 $-$

where ϕ_{inj}, k_{inj}, and k_1 are the e^- injection efficiency, rate constant for e^- injection, and rate constant for e^- decay of the photoexcited dye, respectively. To achieve efficient injection, k_{inj} should be approximately 100 times larger than k_1 for times larger than ratof the system. The kinetics of e^- is related to the performance. If the e^- injection of the device is slowed by increasing the energy of conduction band (E_c), V_{oc} should increase. However, the driving force for e^- injection (E_{inj}) will decrease, resulting in a decreased φ_{inj} and J_{sc}. The positive ionic charge in the electrolyte is delivered from the regeneration of the dye by e^- transfer from iodide ions. Due to the high density of ionic charge in the electrolyte, the excess charges in the oxide nanoporous can be efficiently blocked, and electric fields can be formed. However, the diffusion of electrons is also complicated by trapping and de-trapping processes, influencing the time response [136, 137].

At open-circuit conditions under illumination, the total rate of e^- transfer to I_3^- ions in the electrolyte and to the oxidized sensitizer must be balanced by the net rate of e^- injection. After photoexcited e^- injection from the dye into the conduction band of the nanoparticles, the dye molecules are in their oxidized state and should be reduced by the electrolyte (regeneration). The regeneration time is subject to diffusion-limited kinetics. The diffusion rate constant (k_{diff}) in non-viscous redox coupling electrolyte is in the range of $10^9 \sim 10^{10}$/ms. On the basis of k_{diff}, the regeneration efficiency, ϕ_{reg}, can be determined [138-140].

$$\phi_{reg} = \frac{k_{reg}}{k_{reg} + k_{rec}}$$
Equation 2.10

This equation gives the probability that an oxidized dye will be regenerated by an electrolyte rather than by recombination. The k_{reg} and k_{rec} are the rate constants for regeneration and the first oxidized dye recombination, respectively. In DSSCs, the standard e^- donor in the electrolyte is iodide. After photoinduced e^- injection from the dye to the conduction band of TiO$_2$, the oxidized sensitizer (S^+) should be reduced by iodide as follows [141]:

$$S^+ + I^- \rightarrow (S-I)^{complex} \qquad \text{Equation 2.11}$$

$$(S-I)^{complex} + I^- \rightarrow (S-I_2^-)^{complex} \qquad \text{Equation 2.12}$$

$$(S-I_2^-)^{complex} \rightarrow S + I_2^- \qquad \text{Equation 2.13}$$

$$2I_2^- \rightarrow I_3^- + I^- \qquad \text{Equation 2.14}$$
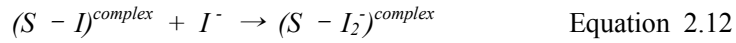
First, one-electron transfer from I^- to S^+ occurs to reduce the oxidized dye. The oxidation of iodide produces free iodine radicals bound to the dye, and an (S-I) complex is formed. Next, a second iodide leads to the formation of an (S-I_2^-) complex, which dissociates into the reduced dye S and I_2^-. Finally, two I_2^- produce triiodide (I_3^-) and iodide (I^-). In the absence of e^- recombination, the steady-state e^- density under illumination at open circuit is determined by Equation 2.15, where v_{inj} and v_{br} are the rates of e^- injection and e^- recombination with I_3^-, respectively [141-143].

$$\frac{dn}{dt} = v_{inj} - v_{br} = 0 \qquad \text{Equation 2.15}$$

The rate of the back-reaction (2.8) depends on the concentration of the reactant. This back-reaction consists of several steps. An e^- at the surface of the counter electrode is captured by I_3^- ions to form the iodine radical ion (2.16). Subsequently, two possible steps with I_2^- can occur (2.17, 2.18) [112, 144, 145].

$$I_3^- + e^- \rightarrow I_2^- + I^- \qquad\qquad \text{Equation 2.16}$$

$$I_2^- + e^- \rightarrow 2I^- \qquad\qquad \text{Equation 2.17}$$

$$2I_2^- \rightarrow I_3^- + I^- \qquad\qquad \text{Equation 2.18}$$

$$I_3^- + e^- \rightarrow I_2^- + I^-$$

$$I_2^- + e^- \rightarrow 2I^-$$
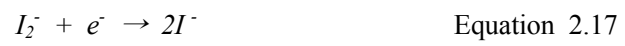
2.2. Characterization of dye-sensitized solar cells (DSSCs)

2.2.1. Efficiency measurement with J-V curve

The current-voltage (*J-V*) characteristics of DSSCs under illumination are used to determine the power-conversion efficiency, *η*. From these data, the open-circuit voltage (V_{oc}) is determined as the $I = 0$ intercept, while the short-circuit current (I_{sc}) or short-circuit current density (J_{sc}) are found at $V = 0$. DSSCs have a fairly slow electrochemical response with high interfacial capacity. Therefore, the voltage scan rate should be sufficiently slow in the current measurement. The maximum power can be achieved when $[I \times V]$ reaches a maximum. The power conversion efficiency is defined as follows [146, 147]:

$$\eta(\%) = \frac{P_{out}}{P_{in}} \times 100 = \frac{V_{\max} \circ J_{\max}}{P_{in}} = \frac{J_{sc} \times V_{oc} \times FF}{P_{in}} \times 100 \qquad \text{Equation 2.19}$$

P_{in} is the power density at a given photon flux (100 mW/cm^2 for an air mass of 1.5), and *FF* is the fill factor of the device, which a value between 0 to 1 that describes the shape of the *J-V* curve. *FF* is calculated by multiplying the photocurrent and voltage, resulting in the maximum electrochemical power. If the value is high, the shape is more rectangular, with high energy conversion efficiency. The open-circuit voltage and the short-circuit current are the maximum voltage and current. However, at both of these operating points, the power from the solar cell is 0. *FF* is a parameter that, in conjunction with V_{oc} and I_{sc}, determines the maximum power from a solar cell. The fill factor is defined as the ratio of the maximum power from the solar cell to the product of I_{sc} and V_{oc}. Graphically, the fill factor is a measure of the "squareness" of the solar cell and is also the area of the largest rectangle that fits in the *I-V* (or *J-V*) curve. The fill factor is

illustrated below [148, 149].

As the fill factor is a measure of the "squareness" of the *I-V* curve, a solar cell with a higher voltage has a larger possible fill factor because the rounded portion of the *I-V* curve takes up less area. The maximum theoretical fill factor from a solar cell can be determined by differentiating the power from a solar cell with respect to voltage and finding where this differential is equal to zero.
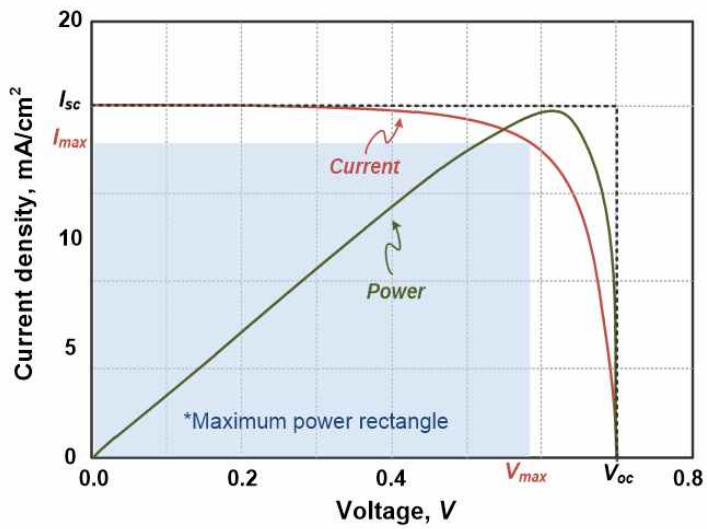
Figure 2.3. Photocurrent-voltage curve of solar cells with short-open-circuit points (V_{oc}, I_{sc}) and maxima (V_{max}, I_{max}) [148].

$$\frac{d(IV)}{dV} = 0 \qquad \text{Equation 2.20}$$

$$V_{max} = V_{oc} - \frac{nkT}{q} ln \left(\frac{V_{max}}{nkT/q} + 1 \right) \qquad \text{Equation 2.21}$$

However, the above technique does not yield a simple or closed-form equation. The equation only relates V_{oc} to V_{max}, and additional equations are needed to find I_{max} and *FF*. A more commonly used expression for the fill factor can be determined empirically as follows [148, 150]:

$$FF = \frac{V_{oc} - h\left(V_{oc} + 0.72\right)}{V_{oc} + 1}$$

Equation 2.22

$$V_{oc} = \frac{q}{nkT}\, V_{oc}$$

Equation 2.23

The above equations show that a higher voltage will have a higher possible fill factor. However, large variations in the open-circuit voltage within a given material system are fairly rare. For example, at one Sun, the difference between the maximum open-circuit voltage measured for a silicon laboratory device and a typical commercial solar cell is approximately 120 mV, giving maximum fill factors of 0.85 and 0.83, respectively. However, the difference in the maximum fill factors can be significant for solar cells made from different materials. For example, a GaAs solar cell may have a fill factor approaching 0.89. The equation also demonstrates the importance of the ideality factor, also known as the "n-factor" of a solar cell. The ideality factor is a measure of the junction quality and the type of recombination in a solar cell. For the simple recombination mechanisms discussed in the Types of Recombination section, the n-factor has a value of 1. However, some recombination mechanisms, particularly if they contain many steps, may introduce recombination mechanisms, providing an n-factor of 2. A high n-value not only degrades the fill factor but also gives low open-circuit voltages because it usually signals high recombination. A key limitation in the equations described above is that they represent a maximum possible fill factor, whereas the actual fill factor will be lower due to the presence of parasitic resistive losses, which are discussed in the Effects of Parasitic Resistances section. Therefore, the fill factor is most commonly determined by measurement

of the *I-V* curve and is defined as the maximum power divided by the product of I_{sc} cuV_{oc}, i.e., [127, 148]

$$FF = \frac{V_{max} \circ I_{max}}{V_{oc} \circ I_{sc}}$$

Equation 2.24

2.2.2. Incident photon-to-current efficiency (IPCE)

The solar spectral response of DSSCs depends on the absorption properties of the sensitizer. The spectral response is determined by measuring the monochromatic incident photon-to-current efficiency (IPCE). Because DSSCs have fairly slow relaxation times, it is important to ensure that the measurement duration for a given wavelength is sufficient for the current to be stabilized. In addition, DSSCs have slower response times than solid-state photovoltaics, so a low chopping frequency should be chosen. To check the IPCE spectra, two measurement methods can be used: AC and DC methods. In the AC method, the monochromatic light is mechanically chopped by a chopper, and the current response is measured by a lock-in amplifier. Moreover, white bias light can be added in the AC method. In the DC method, monochromatic light is obtained by passing white light through a monochromator, and the photocurrent is measured. The J_{sc} in full sunlight is obtained by integrating the IPCE spectrum using the following expression [151, 152]:

$$J_{sc} = \int IPCE\,(\lambda)\,\eta_{inj}\,(\lambda)\,\eta_{oc}\,(\lambda)$$

Equation 2.25
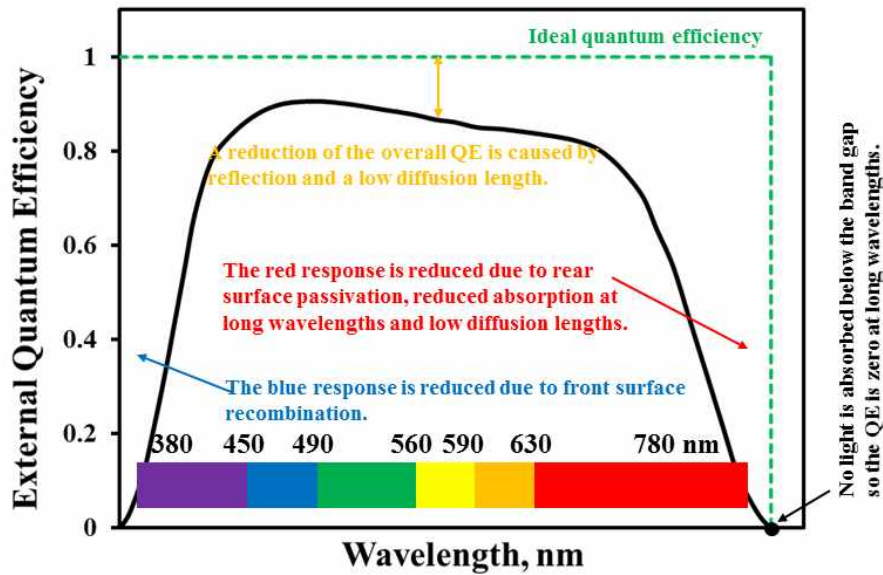
Figure 2.4 The quantum efficiency of a solar cell.

In Equation 2.25, the parameters LHE, ϕ_{inj}, and η_{cc} are the light-harvesting efficiency, efficiency of the e^- injection, and charge collection, respectively. From a fundamental viewpoint, the IPCE value, which is also called the external quantum efficiency (EQE), is the ratio of the observed photocurrent divided by the incident photon flux, uncorrected for reflective losses during optical excitation through the conducting glass electrode. This value shows how efficiently the photons are converted into current [153].

$$IPCE = \frac{[1240\,(eV\,nm)] \times [J_{sc}\,(\mu A/cm^2)]}{[\lambda\,(nm)] \times [P\,(\mu m/cm^2)]}$$

Equation 2.26

2.2.3. Electrochemical methods: cyclic voltammetry and electrochemical impedance spectroscopy

Electrochemical methods, such as cyclic voltammetry (CV) and electrochemical impedance spectroscopy (EIS), are powerful techniques for characterizing DSSCs. The most widely used electrochemical technique, CV, can be performed using a potentiostat connected with a three electrode cell composed of a working electrode, counter electrode, and reference electrode. In CV, the potential is swept at a constant rate and reversed at a certain point, while the current is monitored continuously [154, 155]. The measured current results from faradaic and non-faradaic reactions. The obtained data can be used to obtain the formal redox potentials and information on the reversibility of the e^- transfer process. EIS is widely used to study either the DSSC system as a whole or its individual components, such as the counter/working electrode or electrolyte diffusion. EIS can be performed with a sinusoidal modulated voltage. In this system, the applied potential is perturbed by a sine wave modulation, and the resulting current is measured as a function of modulated frequency. The impedance response of a DSSC is related to the response of the various components of the device. For a resistor, the impedance is a real value, independent of the modulated frequency, while the capacitor and inductors are imaginary values that vary with the frequency. Moreover, the impedance is associated with ion transport in the electrolyte by a finite Warburg element (W), which appears in series with the charge transfer resistance associated with e^- transfer at the cathode. The remaining elements are the double-layer capacitance of the cathode and the series resistance of the DSSC. Using EIS, the following parameters can be obtained: series resistance, charge transfer resistance, diffusion resistance, resistance of e^- transport and recombination in the working electrode, and the chemical capacitance of the working electrode [156]. The equivalent circuit of the DSSC is shown in Figure 2.5 [157].
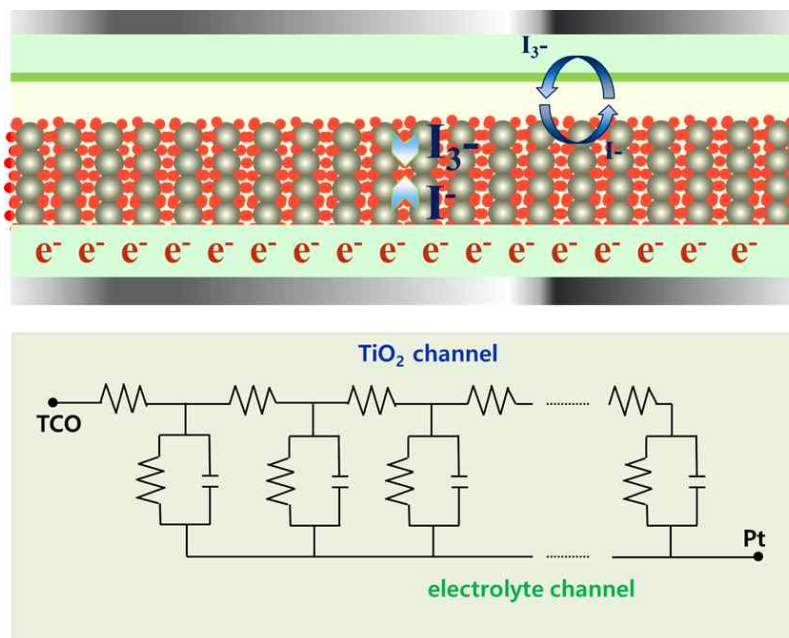
Figure 2.5 Equivalent circuit of the dye-sensitized solar cell [126].

In this circuit, R_s, CPE, R_1, and R_2 represent the series (sheet) resistance in high-frequency region, constant phase element (equivalent electrical circuit component), and two resistances, respectively. A Nyquist plot with a commonly suggested circuit was employed to investigate the interfacial properties of DSSC, and Figure 2.6 shows the Nyquist plot of a general DSSC. In Figure 2.6, the first semicircle, at high frequency, is ascribed to the charge transfer at the interface between the counter electrode and electrolyte (R_{ct1}), and the second semicircle, at intermediate frequency, is associated with the charge transfer across the dye/TiO$_2$/electrolyte (R_{ct2}). The third semicircle is attributed mainly to the Nernst diffusion of I_3^- ions within the electrolyte (R_{diff}). To analyze this system in more detail, a Bode phase plot can be composed [158, 159].
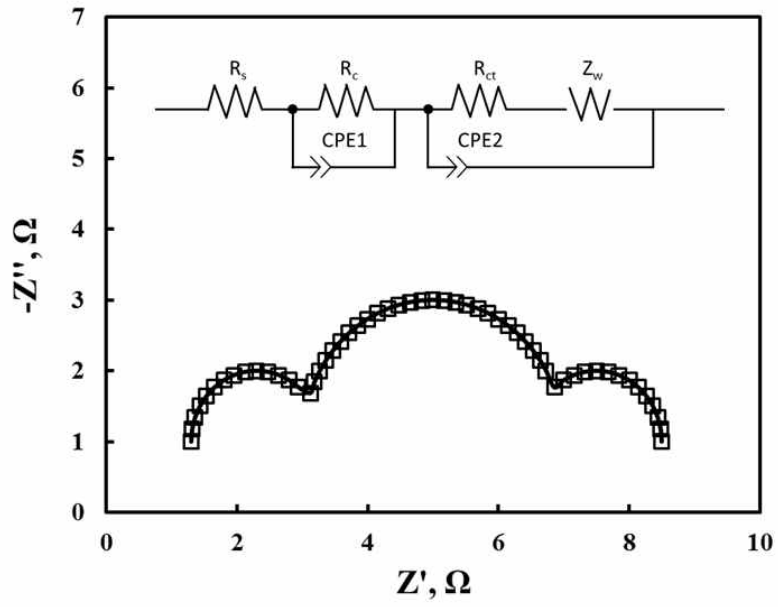
Figure 2.6 Nyquist plot of conventional DSSCs.

Chapter 3. Hierarchically Structured Photoelectrodes of Biomimetic Replication from Butterfly Wings

3.1. Introduction

Dye-sensitized solar cells (DSSCs) were first reported by Gratzel in 1991 [61]. The initial design consisted of a dye-adsorbed mesoporous titania film filled with iodide/triiodide redox electrolyte and a Pt counter photoanode. Much effort has since been devoted to improving the photovoltaic conversion efficiency. Theoretically, a perfect photoelectrode for DSSCs must provide fast electron injection and separation, fast electron transport, slow electron recombination, a high surface area, and excellent light collection [160]. The photonic structures in butterfly wings have been found to have promising applications in infrared detectors, photo-trappers, and flat-panel displays [161]. Recently, a novel photoelectrode structure biotemplated from a butterfly wing has been developed to improve the light-absorbing performance of DSSCs.

Liu et al. proposed a facile one-step approach for the replication of butterfly wings in TiO$_2$, with the resulting structures containing ordered mesopores [162]. Han et al. reported light-trapping phenomena in the wing scales of the butterfly *Papilio peranthus*. A complex functional structure is formed by a variety of monolayer films with different refractive indexes and thicknesses. Interference between neighboring ridges in the multilayer film structure creates a light-trapping effect [163]. Zang et al. synthesized a novel photoanode templated from butterfly-wing scales, with a quasi-honeycomb structure composed of shallow concavities and cross-ribbing. The quasi-honeycomb-structured TiO$_2$ replica photoanode was found to have a higher surface area and light absorbance, both of which are advantageous in terms of light-harvesting efficiency and dye sorption [164]. A number of studies have focused on their structural properties [165-167]. However, to date, no systematic study has investigated the influence of dye sorption and electron lifetime on the photovoltaic conversion efficiency of DSSCs.

3.2. Experimental

3.2.1. Synthesis of TiO₂ replicas from butterfly wings

The wings of the *Papilio paris* butterfly were used as biological templates. Figure 3.1 shows the preparation method for the butterfly-wing architecture TiO$_2$. A Pluronic P123 triblock copolymer (EO$_{20}$PO$_{70}$EO$_{20}$, Mw. 5,800 g/mol, Sigma-Aldrich Co.) was used as the structure-directing agent for the butterfly wings. The titanium tetrachloride (i.e., TiCl$_4$, Sigma-Aldrich Co.) was used as the TiO$_2$ source for the modified butterfly-wing architecture.
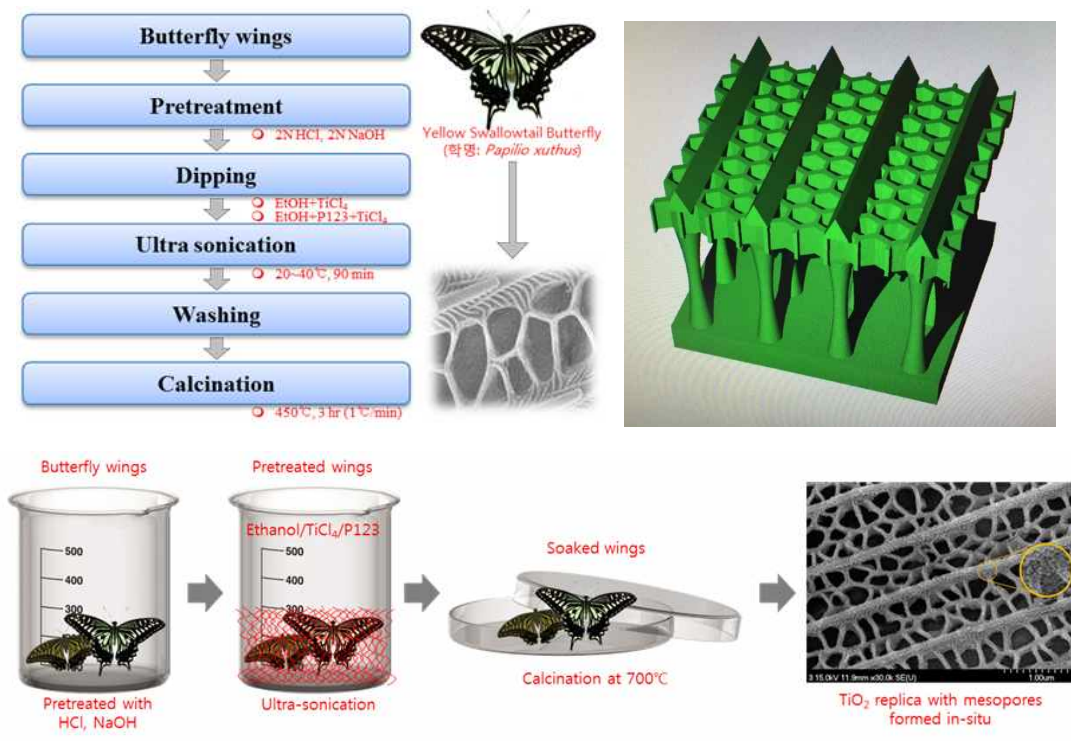
Figure 3.1. Synthesis process for the butterfly-wing TiO$_2$ replicas.

The butterfly wings were pretreated with 10 ml of HCl (35 wt%, Sigma-Aldrich Co.) at room temperature and 2 N NaOH (98%, Sigma-Aldrich Co.) aqueous solution to remove proteins. The pretreated wings were then carefully immersed in a solution of Pluronic P123 triblock copolymer (10 g), and 3 mM $TiCl_4$ was added with 10 ml of ethanol. The mixture was ultrasonicated at room temperature using a high-intensity ultrasonic probe. The sonicated butterfly wings were washed five times with distilled water, dried in air, and then calcined at 723.15 K for 2 h. The chitin substrates and surfactant were removed by reaction with the air. A metal oxide in the form of the ceramic butterfly wings is then obtained. The resulting replicas are named "butterfly-wing TiO_2" (BW-TiO_2) in the following text.

3.2.2. Fabrication of hierarchically structured photoelectrodes for DSSCs

Figure 3.2 shows a schematic diagram of the fabrication of photoelectrodes using nanoporous TiO_2 particles through the repetitive coating method. For the preparation of the nanoporous TiO_2 thin films, TiO_2 slurry was prepared by mixing 1 g nanoporous TiO_2 particles, 0.2 ml acetic acid, 5 ml distilled water, 6 ml ethanol, 20 g terpineol, and 3 g ethylcellulose for 3 h at 1,250 rpm using a paste mixer (DAEWHA TECH PDM-300, Korea). A nanoporous TiO_2 film was then obtained by coating the slurry onto fluorine-doped tin oxide (FTO) glass (Pilkington, TEC-8, 80% transmittance in the visible region) by doctor blade coating (an adhesive polymer film was used as a spacer of ca. 58 μm thickness). The nanoporous TiO_2 film was treated by heating at 723.15 K for 2 h. The nanoporous TiO_2 film formed on the FTO glass was 8~9 μm thick and 0.5×0.5 cm^2 in size. In addition, multi-layer coating of the nanoporous TiO_2 film was conducted to study its influence on the efficiency enhancement of the DSSC. The coated nanoparticle TiO_2 (NP-TiO_2) films were re-coated with nanoporous BW-TiO_2 paste and calcined. To fabricate the DSSC, the prepared thin film electrode was immersed in 0.3 mM N719 dye (Solaronix Co.) solution at 303.15 K for 12 h, rinsed with anhydrous ethanol, and dried. A Pt-paste-coated TEC glass electrode was prepared as a counter electrode with an active area of 0.5×0.5 cm^2. The Pt electrode was placed over the dye-adsorbed nanoparticle TiO_2

photoelectrode, and the edges of the cell were sealed with 2-mm-wide stripes of a 60-µm-thick sealing sheet (SX 1170-60, Solaronix Co.). Sealing was accomplished by hot-pressing the two photoelectrodes together at 373.15 K. The electrolyte was filled into the cell through the holes, and the filling ports were sealed with a sealant glue (Amosil 4, Solaronix Co.). The redox electrolyte was 0.3 M 1,2-dimethyl-3-propylimidazolium iodide (Solaronix Co.), 0.5 M LiI (Sigma-Aldrich Co.), 0.05 M I_2 (Sigma-Aldrich Co.), and 0.5 M 4-tert-butylpyridine (4-TBP, Sigma-Aldrich Co.) with 3-methoxypropionitrile (3-MPN, Fluka Co.) as the solvent.
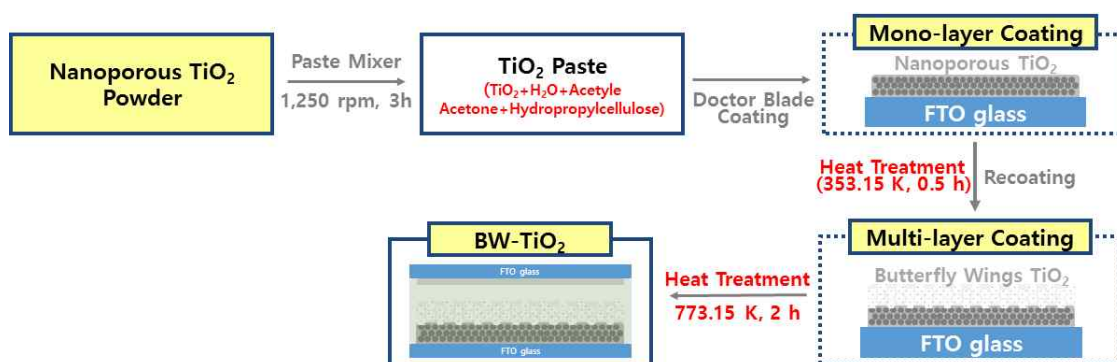
Figure 3.2. Fabrication of nanoporous TiO_2 electrodes.

3.2.3. Fabrication of adsorption photoelectrodes for DSSCs

This work presents important experimental data obtained from direct measurements of the amounts of dye adsorbed on the TiO_2 thin films. The adsorption apparatus consists of a water circulation jacket (a), vessel (b), photoelectrode holder (c), magnetic stirrer bar (d), and TiO_2-coated thin film (e). The water circulation jacket was connected to a thermo-circulator. All runs were conducted at 298.15 K. The volume of the vessel was approximately 25 ml, and that of the dye solution was 20 ml. To prevent the magnetic stirrer bar from destroying the TiO_2 thin film, we maintained a distance of 3 mm between the bottom of the vessel and the TiO_2 thin film. To increase the amount of dye adsorbed

on the TiO_2 thin film in the adsorption apparatus, we placed the photoelectrode in the photoelectrode holder with its TiO_2-coated surface facing downward. The stirrer bar was centered with respect to the vessel such that it could rotate without wobbling inside the vessel, while the dye was agitated continuously to facilitate its adsorption on the TiO_2 thin film. To measure the amount of dye adsorbed on the TiO_2 thin film without involving a desorption step, we periodically extracted samples using a micro-pipette. The amount of dye adsorbed was calculated using Equation 3.1:

$$q_t = (C_0 - C_t)\,V/W \qquad\qquad \text{Equation 3.1}$$

where C_0 and C are the liquid-phase concentrations (mg/L) of N719 at time 0 and time t, respectively. The concentration of the N719 dye solution was determined using a UV spectrophotometer (Shimadzu UV-160A, Japan) based on the absorbance of the solution at 528 nm.

3.2.4. Characterization of BW-TiO$_2$ photoelectrodes for DSSCs

In this work, TiO_2 photoelectrodes were biotemplated from a *Parpilio paris* butterfly wing, and their fine hierarchical structure was characterized by field-emission scanning electron microscopy (FE-SEM; Hitachi S-4700, Japan) and X-ray diffraction (XRD, Rigaku D/MAX-1200, Japan). The resulting concentration was analyzed on the basis of the absorbance of the solution at 528 nm using a UV/vis spectrophotometer (Shimadzu UV-160A, Japan). The adsorption kinetics of the N719 dye molecules on thin TiO_2 films was measured and analyzed using a pseudo-second-order model. The electron lifetime in hierarchical TiO_2 photoelectrodes was determined from open-circuit-voltage-decay (OCVD) curves and electrochemical impedance spectroscopy (EIS; CH Instruments CHI660E, USA). The current-voltage (*I-V*) curves were recorded under white-light irradiation from a 200-W

xenon lamp (McScience, Korea). The active cell area and the incident light intensity were 100 mW/cm^2 and 0.5 × 0.5 cm^2, respectively. The *J-V* curves were used to calculate the short-circuit current density (J_{sc}), open-circuit voltage (V_{oc}), fill factor (*FF*), and efficiency (η_{eff}) of DSSC.

3.3. Results and discussion

3.3.1. Characteristics of biotemplated BW-TiO$_2$

Figure 3.3 shows the wing architecture of *Papilio paris*, a species of butterfly found in Asia, and its TiO$_2$ replica. The scales in the original butterfly wing have parallel ridges spaced several microns apart and aligned lengthwise. The lamellae (ridges) are hollow and comprise cross-ribs on the bottom surface. The ridges are composed of nanoscale ribs (~10 nm in width) approximately 50 nm apart. The fine microstructural details of the original butterfly-wing scales are still observed after calcination in the BW-TiO$_2$ samples. However, the interlamellar spacing has decreased by ~ 48% to approximately 0.56 μm due to the elevated calcination temperature.
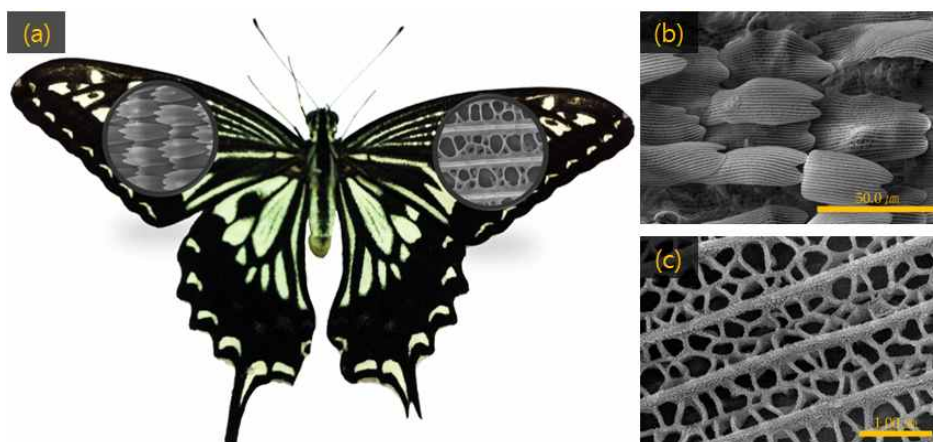
Figure 3.3. FE-SEM images of butterfly wings and templated TiO$_2$.

Figure 3.4 shows the XRD patterns obtained from BW-TiO$_2$ samples calcined at 450 °C. Peaks are observed at 2θ values of 25.2, 37.8, 48.0, 55.0, 62.6, 68.7, 70.3, and 75.0°, corresponding to the (101), (004), (200), (211), (204), (116), (220), and (215) crystal planes of anatase TiO$_2$ (JCPDS no. 211272), respectively. The average crystallite size of BW-TiO$_2$

is approximately 12.1 nm, as calculated from the XRD patterns using Scherrer's formula:

$$D = \frac{k\lambda}{\beta \cos\theta}$$

<div align="right">Equation 3.2</div>

where D is the crystallite size, λ is the wavelength of the X-rays, β is the width of the diffraction line measured at half the maximum intensity, and θ is the corresponding angle.
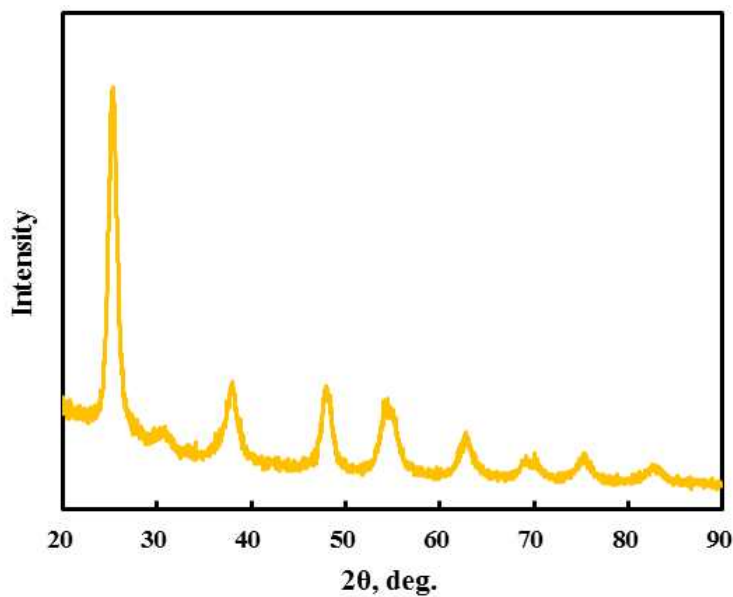
Figure 3.4. XRD patterns obtained from NP-TiO$_2$ and BW-TiO$_2$ cells.

3.3.2. Adsorption study of BW-TiO$_2$ photoelectrodes toward N719 dye

The photovoltaic conversion efficiency of materials is known to be highly dependent on their adsorption properties. Adsorption kinetics can be used to understand the sorption mechanism on nanoparticle TiO$_2$ thin films.
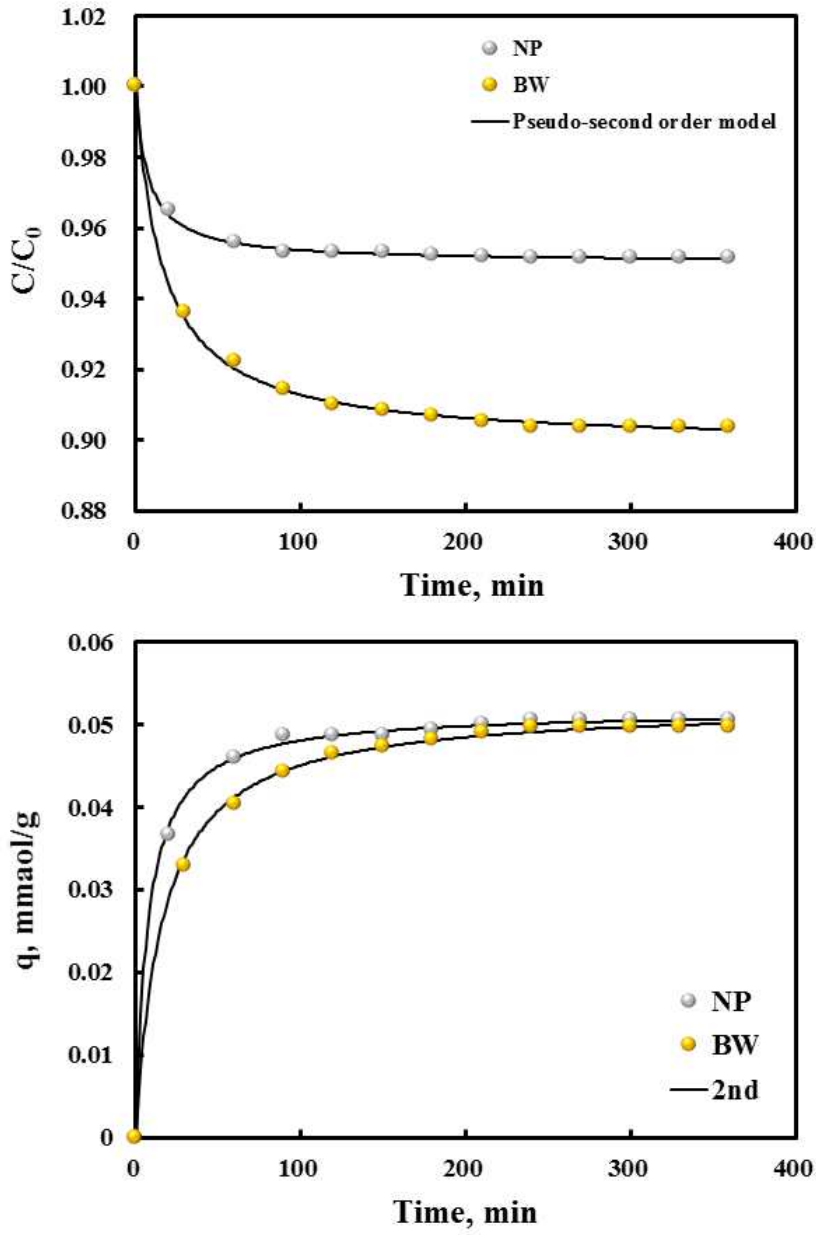
Figure 3.5. Adsorption kinetics of N719 dye onto NP-TiO$_2$ and BW-TiO$_2$ cells.

Figure 3.5 shows the adsorption kinetics of N719 onto NP-TiO$_2$ and BW-TiO$_2$ thin films obtained in a small-batch adsorption chamber without a desorption step [168]. The parameters obtained from pseudo-second-order models of the kinetics of N719 adsorption onto the NP-TiO$_2$ and BW-TiO$_2$ thin films are listed in Table 3.1. The models fit the experimental data very well ($R^2 > 1.0$). For NP-TiO$_2$ and BW-TiO$_2$, the second-order rate constants are 2.57 and 1.18 g/(mol·min), respectively, with the same q_e, 0.052 mmol/g, for both samples.

Table 3.1. Kinetic adsorption characteristics of NP-TiO$_2$ and BW-TiO$_2$ cells

Samples	k_2 [g/mol·min]	q_e [mmol/g]	R^2
NP-TiO$_2$	2.57	0.052	1.00
BW-TiO$_2$	1.18	0.052	1.00

3.3.3. Characteristics of hierarchically structured photoelectrodes
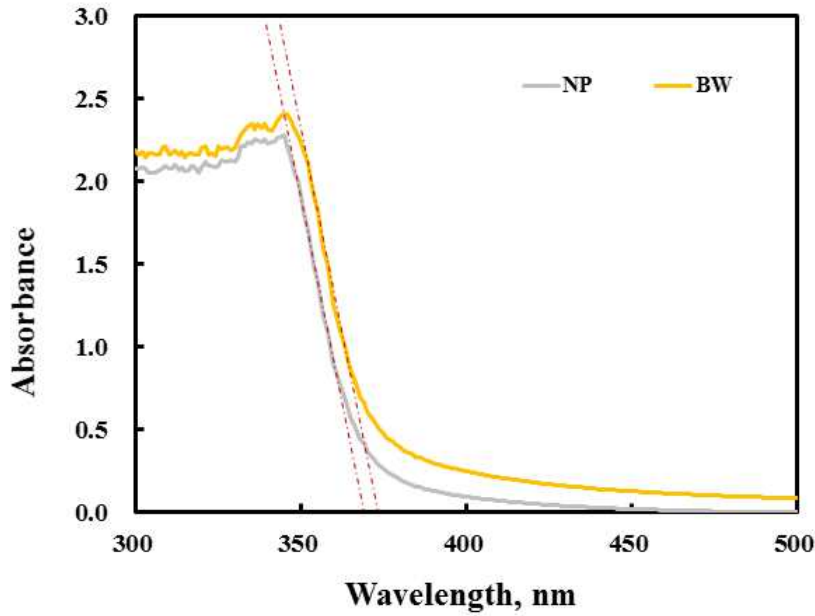
Figure 3.6. UV-vis absorption spectra of NP-TiO₂ and BW-TiO₂ cells.

The light-harvesting properties of the samples were examined using absorbance spectroscopy. Figure 3.6 shows the optical properties of the BW-TiO$_2$ and NP-TiO$_2$ films. The UV-vis curve for the BW-TiO$_2$ film is redshifted relative to that for the NP-TiO$_2$ film. In addition, the BW-TiO$_2$ film strongly absorbed visible wavelengths between 400 and 500 nm. The absorption edge for the two samples was determined using the following equation [169]:

$$E_g = \frac{1239.8}{\lambda} \qquad \text{Equation 3.3}$$

– 51 –

where E_g is the band gap (eV) of the sample and λ (nm) is the wavelength of the onset of absorption. The band gaps for the NP-TiO$_2$ and BW-TiO$_2$ films are thereby calculated to be 3.22 and 3.18 eV, respectively. The BW-TiO$_2$ sample has a greater absorbance than NP-TiO$_2$, suggesting that film morphology plays an important role in light-harvesting and that hierarchical structures have high absorption properties.
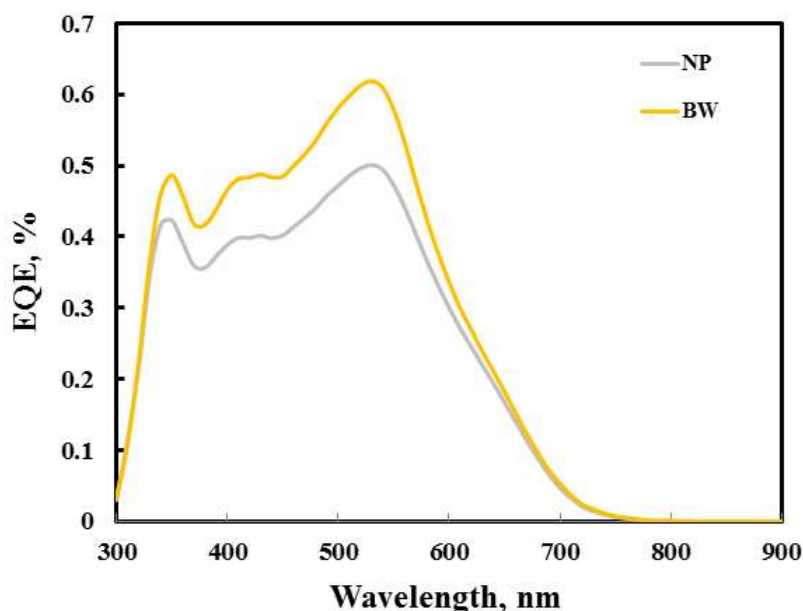
Figure 3.7. Incident photon-to-current efficiency curves for NP-TiO$_2$ and BW-TiO$_2$.

The incident photon-to-current efficiency (IPCE) spectra obtained from the NP-TiO$_2$ and BW-TiO$_2$ samples are shown in Figure 3.7 The peak efficiency at 530 nm corresponds to the maximum absorption wavelength of the N719 dye. For all wavelengths, the external quantum efficiency is higher for the BW-TiO$_2$ electrode than the NP-TiO$_2$ electrode, which is consistent with the J_{sc} values obtained by photocurrent-voltage measurements (see below). The IPCE peak height at 530 nm for the BW-TiO$_2$ electrode is 61.8%, which is much higher than the value of 50% obtained with the NP-TiO$_2$ electrode. Figure 3.8 shows the photocurrent-voltage curves obtained for the NP-TiO$_2$ and BW-TiO$_2$ photoelectrodes. The

BW cell achieved a short-circuit current density (J_{sc}) of 10.66 mA/cm^2 and an energy conversion efficiency (η) of 4.32% (Figure 3.8 and Table 3.2). In comparison, the DSSC based on the NP-TiO$_2$ film had J_{sc} and η values of 8.17 mA/cm^2 and 3.48%, respectively. These results indicate that the 24% improvement in η results mainly from the 30% increase in J_{sc}. The increase in the latter is most likely due to the improved light scattering and dye uptake afforded by the BW-TiO$_2$.
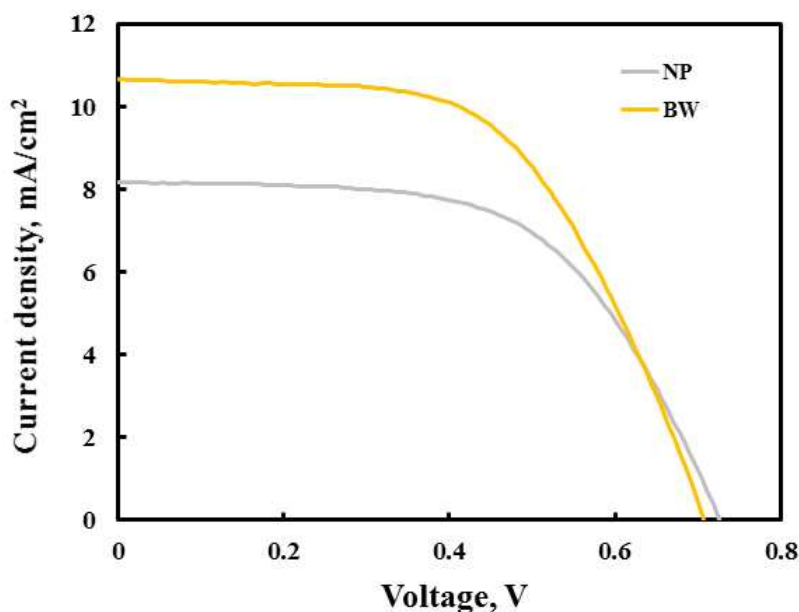
Figure 3.8. Photocurrent-voltage (*J-V*) curves for NP-TiO$_2$ and BW-TiO$_2$ cells.

Table 3.2. Photocurrent-voltage (J-V) characteristics of NP-TiO$_2$ and BW-TiO$_2$ cells

Samples	J_{sc} [mA/cm^2]	V_{oc} [V]	*Fill Factor* [%]	*Efficiency* [%]
NP-TiO$_2$	8.17	0.73	58.6	3.48
BW-TiO$_2$	10.66	0.71	57.3	4.32

To investigate the recombination kinetics in fine hierarchical structures, OCVD measurements reported by Zaban and Greenshtein are used [170]. As shown in Figure 3.9, OCVD measurements were conducted by monitoring the V_{oc} transient during relaxation from an illuminated quasi-equilibrium state to the dark equilibrium. The photovoltage decay rate is directly related to the electron lifetime by the following expression:

$$\tau_n = \frac{-k_B T}{e} \left[\frac{dV_{oc}}{dt} \right]^{-1} \qquad\qquad \text{Equation 3.4}$$

where τ_n is the reciprocal of the derivative of the decay curve normalized by the thermal voltage, $k_B T$ is the thermal energy, e is the elementary charge, and dV_{oc}/dt is the derivative of the open-circuit voltage transient. Equation 3.3 is obtained based on the assumption that the recombination is linear with a first-order dependence on the electron concentration and that electron recombination occurs only with the electrolyte.

Figure 3.9(a) shows the OCVD curves measured for NP-TiO$_2$ and BW-TiO$_2$ cells. The voltage decay of the BW-TiO$_2$ cell is slower than that of the NP-TiO$_2$. Figure 3.9(b) shows the response times obtained by applying Equation 3.3 to the data in Figure 3.9(a). Electron recombination is slow in both the BW-TiO$_2$ and NP-TiO$_2$ cells, allowing them to sustain significant voltages many seconds after the light is turned off. The τ_n values are much larger in the BW-TiO$_2$ cell than in the NP-TiO$_2$ cell. This result suggests that the recombination of the photogenerated electrons with electrolyte-oxidized species is slower in the BW-TiO$_2$ electrode. This effect may also explain the higher performance of the BW-TiO$_2$ DSSC electrode.
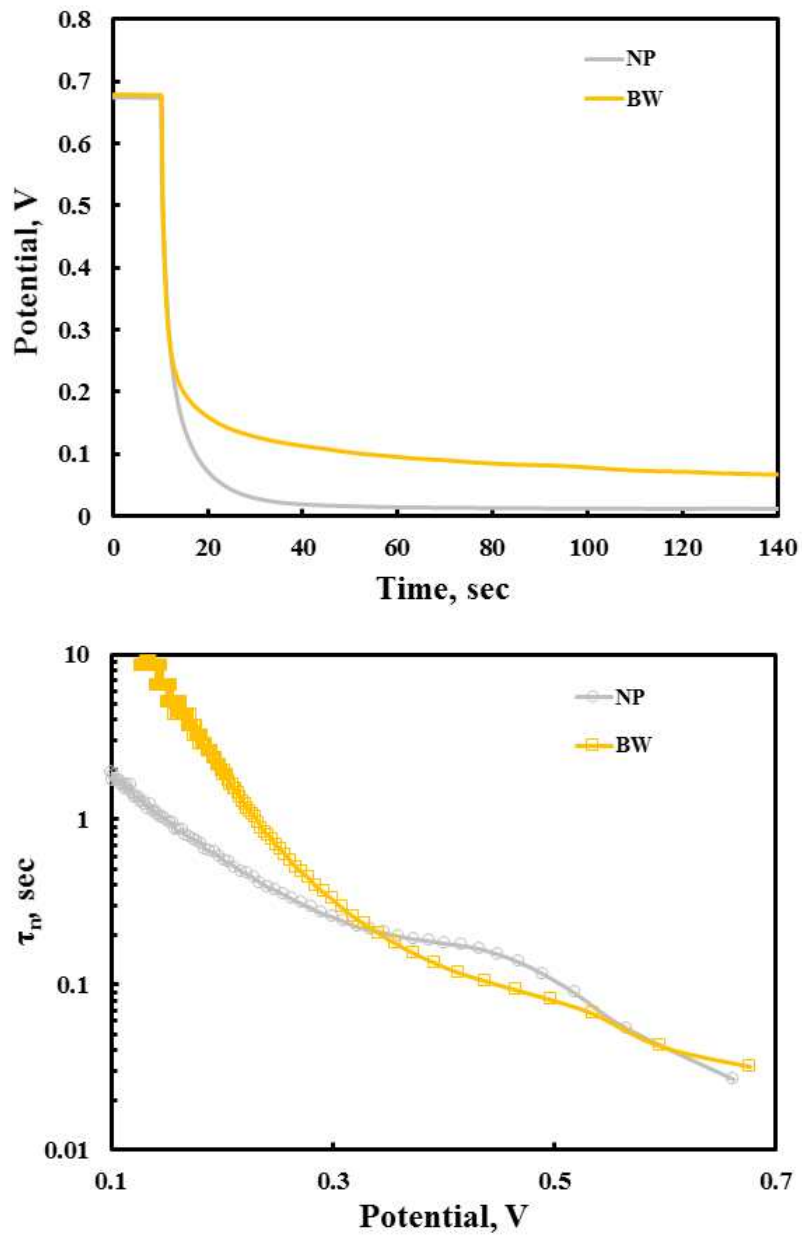
Figure 3.9. (a) OCVD curves and (b) the corresponding response times for NP-TiO$_2$ and BW-TiO$_2$ cells.

To examine the internal resistance and charge transfer kinetics of the samples, EIS was performed under illumination at an applied bias of V_{oc} with an AC amplitude of 10 mV. Figure 3.10(a) shows the Nyquist plots obtained for the NP-TiO$_2$ and BW-TiO$_2$ cells. Two well-defined semicircles are charge transfer resistance at the electrolyte-Pt-FTO interface (R_{ct1}) and charge transfer resistance at the TiO$_2$-dye-electrolyte interface (R_{ct2}). The equivalent-circuit model of the DSSCs is shown in the inset of Figure 3.10(a). The serial resistance (R_s) of the NP-TiO$_2$ cell is slightly larger than that of the BW-TiO$_2$ cell, such that the former has a lower fill factor than the latter.

The R_{ct1} resistances of the two DSSCs are almost identical, whereas the R_{ct2} resistance of the BW-TiO$_2$ cell is smaller. Resistances of approximately 37.1 imatelys r. BW- obtained for the NP-TiO$_2$ and BW-TiO$_2$ cells, respectively, by fitting the Nyquist plots to the equivalent circuit model. These values indicate faster electron transfer in the BW-TiO$_2$ cell. As supported by the UV-vis spectra, this can be attributed to more efficient light-harvesting.

The electron lifetime (i_s) in the TiO$_2$ films can be obtained from the characteristic angular frequency (i_{mid}) of the middle frequency (f_{mid}) peak in the Bode phase plots using the relation $f_s = 1/g_{mid} = 1/2$ thf_{mid}. The Bode phase plots for the NP-TiO$_2$ and BW-TiO$_2$ cells are shown in Figure 3.10(b). The characteristic frequency for the BW-TiO$_2$ cell is downshifted by 26.1 Hz with respect to the corresponding peak for the NP-TiO$_2$ cell. The electron lifetimes for the NP-TiO$_2$ and BW-TiO$_2$ cells obtained from these peaks are 6.1 and 7.4 ms, respectively. This result implies that film morphology plays an important role in DSSC electron recombination.
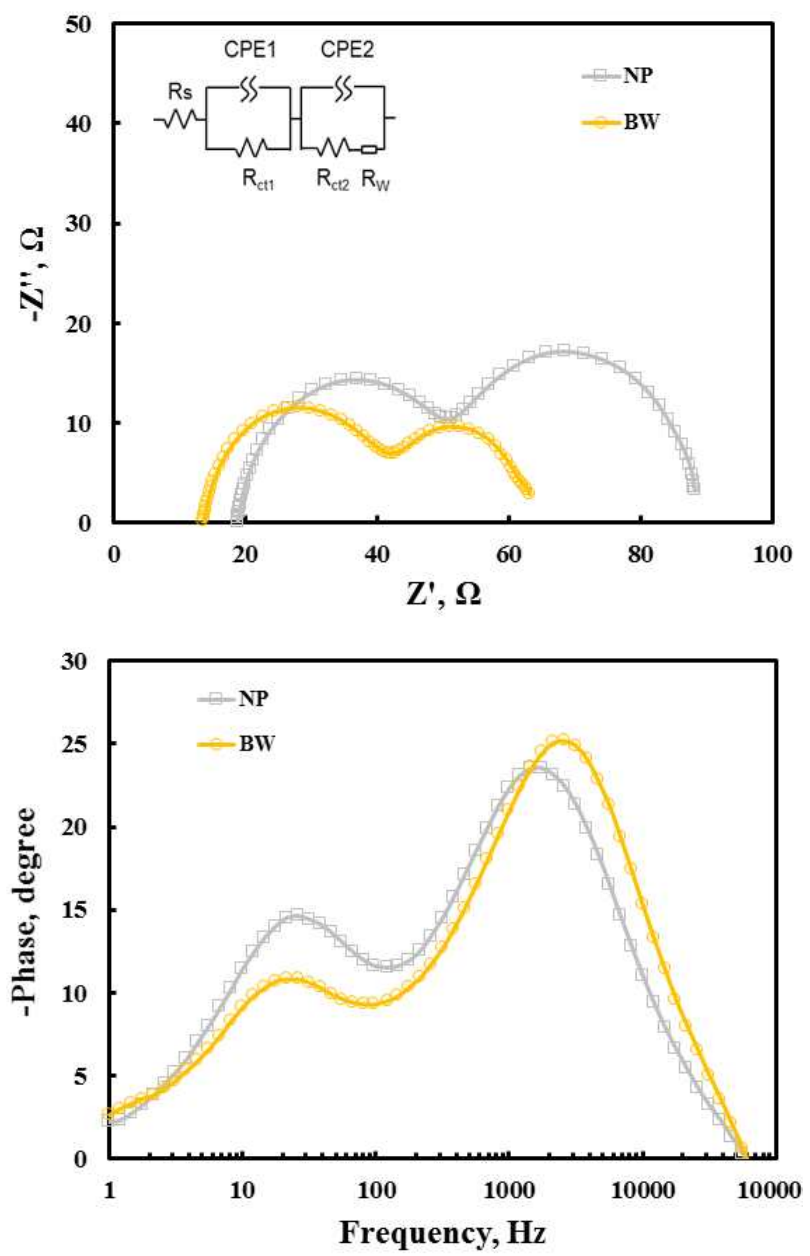
Figure 3.10. (a) Nyquist plots and (b) Bode phase plots for NP-TiO$_2$ and BW-TiO$_2$ cells. The inset in (a) shows the equivalent circuit model of both cells.

3.4. Conclusions

Fine hierarchical TiO_2 structures were successfully synthesized using *Parpilio paris* butterfly wings as biotemplates. The prepared samples have homogeneous pores, ca. 0.1 ~ 0.5 nm in size, and large pore volumes and surface areas. The electron lifetimes in $NP\text{-}TiO_2$ and $BW\text{-}TiO_2$ films, determined from EIS measurements, are 6.1 and 7.4 ms, respectively, with photovoltaic conversion efficiencies of 3.48 and 4.32%, respectively. These results show that hierarchical structures have an important and positive impact on light absorption and light-harvesting properties.

Chapter 4. Successive Adsorption of N719 and MK-2 for Co-Sensitization in Dye-Sensitized Solar Cells

4.1. Introduction

Dye-sensitized solar cells (DSSCs) consist of a nanoporous semiconductor metal oxide electrode, an adsorbed dye, an electrolyte, and a counter electrode. They have many advantages for the conversion of visible light into electrical energy, such as high conversion efficiency, low cost, and easy fabrication [61, 171, 172]. Many research groups have developed strategies to improve the photovoltaic performance of DSSCs [160, 173-178]. One of these strategies is to improve the efficiency of the dye adsorption characteristics.

Table 4.1. Literature review

Authors	Dyes	Effi.(%)	Method	Ref.
Kazuhiro Noda et al.	N749/D131	11.0	cocktail	[179]
Shuzi Hayase et al.	Z907/NK3705	7.1	cocktail	[180]
Michael Gratzel et al.	C106/D131	11.1	cocktail	[181]
Michael Gratzel et al.	TT1/JK2	7.74	cocktail	[182]
Eric Wei-Guang Diau et al.	LD12/CD5	9.0	cocktail	[183]
Kuo-Chuan Ho et al.	N719/FL	5.1	successive	[184]
Nam-Gyu Park et al.	N719/N749/P5	4.8	cocktail	[185]
Kazuhiro Sayama et al.	Cy0/Cy1/SQ	3.1	cocktail	[186]
Sheng-Min Cai et al.	A/B	3.4	cocktail	[187]
Kuo-Chuan Ho et al.	SQ2/5c	6.2	cocktail	[188]
Shyam S. Pandey et al.	NK3705/Z907	7.1	cocktail	[189]

Recently, Gratzel et al. reported a high performance of 12.3% using single ruthenium dye [190]. Park et al. employed N719, N749, and P5 dyes as sensitizers for DSSC with an efficiency of 4.8% [185]. Wei et al. achieved a conversion efficiency of 7.64% using the successive adsorption method [191]. It has been reported that the electron lifetime increases with the length of the alkyl chains of MK-2 because longer chains prevent the approach of acceptors (i.e., I_3^- ions) to the TiO$_2$ surface and/or reduce the reorganization energy of the dye, resulting in the desired situation for the kinetic competition for the reduction of the dye cation (Figure 4.2).
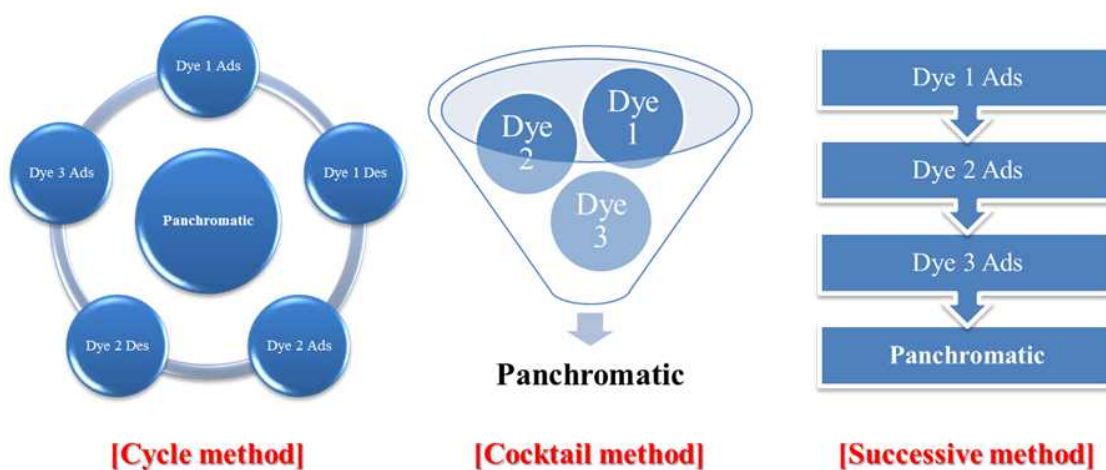
Figure 4.1. Adsorption mode.

In addition, the aggregation of dye molecules would also be suppressed by the steric hindrance due to the long alkyl chains [192]. It is generally known that the photovoltaic performance of DSSCs is strongly influenced by adsorption properties of dyes on TiO$_2$ thin films. Unfortunately, research on the adsorption properties (i.e., equilibrium and kinetics) of dye molecules is still nascent. In this work, the influence of the adsorption mode of the N719 and MK-2 dye onto the TiO$_2$ thin film on the energy conversion efficiency of the DSSCs was systematically investigated. To this end, experimental and theoretical studies on the adsorption equilibrium and kinetics were conducted to control the adsorption amount and understand the mechanism of the adsorption of N719 and MK-2 as photosensitizers

onto TiO$_2$ thin films. The equilibrium data were fitted by the Langmuir isotherm model, and the adsorption kinetic data were obtained and analyzed on the basis of pseudo-second-order models to understand the adsorption mechanisms of successive adsorption of N719 and MK-2 dyes.

(a)
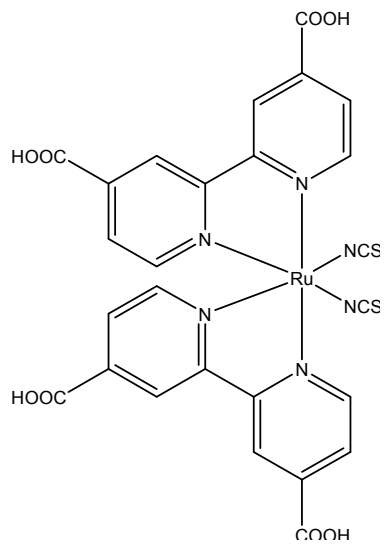
(b)
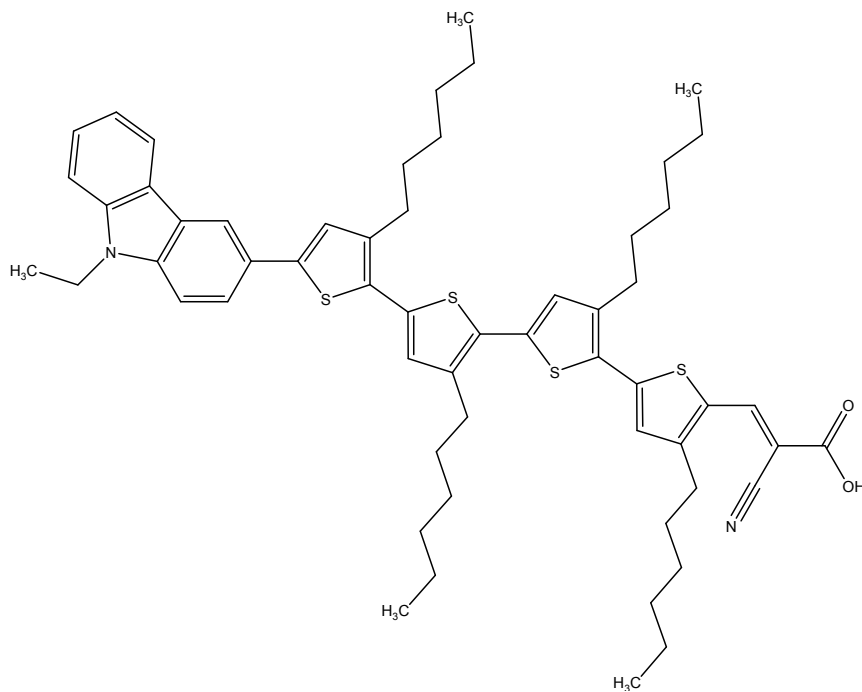
Figure 4.2. Molecular structure of N719 dye (a) and MK-2 dye (b).

4.2. Experimental

4.2.1. Fabrication of nanoporous TiO₂ electrodes for successive adsorption DSSCs

TiO$_2$ paste (DSL18NR-T, Dyesol co.) was used to prepare TiO$_2$ films for the DSSCs. The paste was coated on pre-cleaned fluorine-doped tin oxide (FTO) conducting glass (Pilkington, TEC-8, 80% transmittance in the visible region) by a squeeze-printing technique followed by annealing at 723.15 K for 30 min. The TiO$_2$ photoelectrodes were deposited on FTO glass substrates with active areas of 2.0 × 2.0 cm^2 and 0.5 × 0.5 cm^2 for adsorption kinetics and photovoltaic efficiency measurements, respectively.
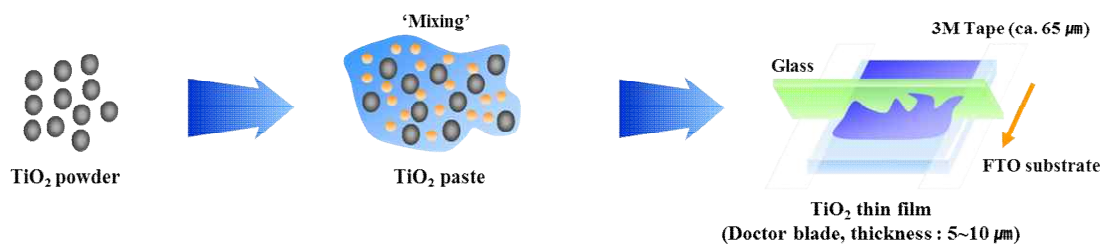
Figure 4.3. Preparation of TiO₂ film using the doctor blade method.

4.2.2. Fabrication of an adsorption apparatus for measurement of adsorption properties

The prepared photoelectrodes were immersed overnight (ca. 24 h) in a 5 × 10^{-4} mol/L ethanol solution of di-tetrabutylammonium cis-bis(isothiocyanato)bis(2,2′-bipyridyl-4,4′-dicarboxylato) ruthenium (Ⅱ) (N719, Solaronix co.) and 5 × 10^{-4} mol/L toluene solution of 2-cyano-3-[5luene soluti-9*H*-carbazol-3-yl)-3luti-9 of 5 othioc*n*-hexyl-[2,2-yl)-3luti-9 of 5 othrter-thiophen-5-yl] acrylic acid (MK-2, Sigma-Aldrich Co.), rinsed with anhydrous ethanol, and dried. A TiO$_2$ film, approximately 8 ~ 9 µm thick, was deposited on a 0.25-cm^2 FTO glass substrate.

Collection @ chosun
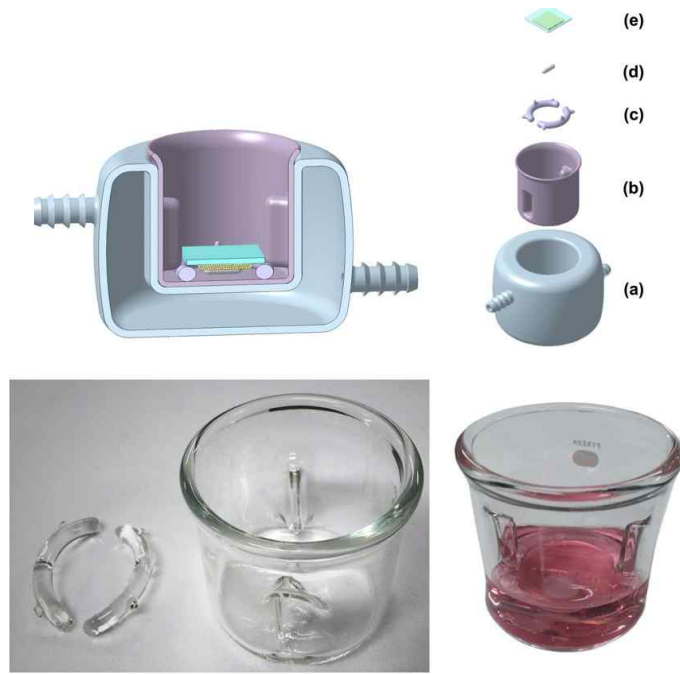
Figure 4.4. Schematic diagram (A) and photograph (B) of the adsorption experiment apparatus.
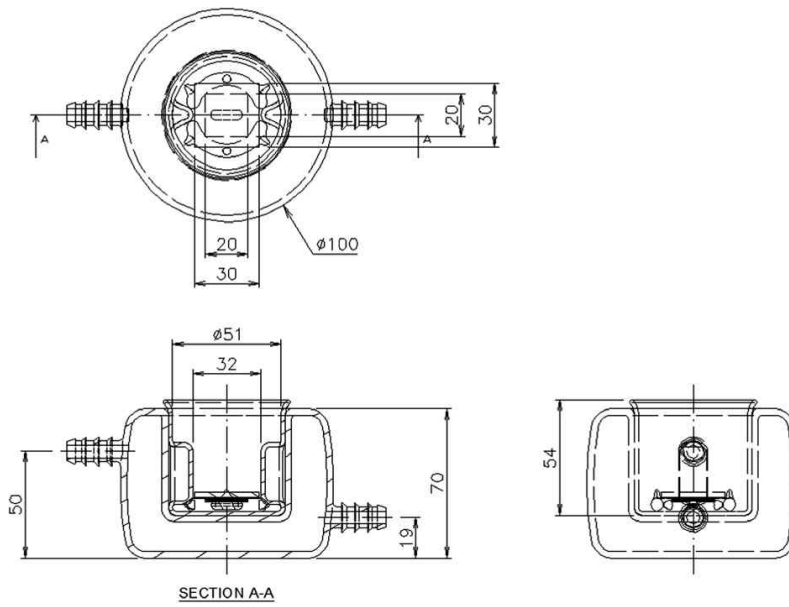
Figure 4.5. Detailed diagram of the adsorption experiment apparatus.

This work presents important experimental data obtained from the direct measurement of the amount of dye adsorbed on the TiO$_2$ thin film. Figure 4.4 shows a schematic of the apparatus used in this work for the direct measurement of the amount of dye adsorbed. The adsorption apparatus consists of a water circulation jacket (a), vessel (b), photoelectrode holder (c), magnetic stirrer bar (d), and TiO$_2$-coated thin film (e). The water circulation jacket was connected to a thermo-circulator. All runs were conducted at 298.15 K. The volume of the vessel was approximately 25 ml, and that of the dye solution was 20 ml. To prevent the stirrer bar from destroying the TiO$_2$ thin film, the distance between the bottom of the vessel and TiO$_2$ thin film was fixed at 3 mm. To improve the adsorption efficiency of the dyes on the TiO$_2$ thin film in the adsorption apparatus, the coated TiO$_2$ surface of the photoelectrode was faced downwards in the photoelectrode holder. The stirrer bar was centered such that it could rotate properly inside of the vessel, while the dye was agitated continuously to facilitate its adsorption on the TiO$_2$ thin film. Figure 4.5 shows a detailed diagram of the adsorption experiment apparatus. The diameter of the chamber including the water circulation jacket was 100 mm. The outer and inner lengths of the photoelectrode holder were 30 and 20 mm, respectively. The height and diameter of the adsorption chamber were 54 and 51 mm, respectively. To measure the amount of dye adsorbed on the TiO$_2$ thin film without a desorption step, samples were taken periodically using a micropipette. The concentrations of the N719 and MK-2 solutions adsorbed on the TiO$_2$ thin film were analyzed based on the absorbance of the solution at 528 or 378 nm, respectively as measured by a UV spectrophotometer (Shimadzu UV-1601A, USA). The amounts of N719 and MK-2 at equilibrium on the TiO$_2$ thin film were calculated from the following equation:

$$q = (C_0 - C)\,V/W \qquad \text{Equation 4.1}$$

where q (mg/g) is the equilibrium amount of the dyes adsorbed on the TiO$_2$ thin film. C_0 and C (mg/l) are the initial and equilibrium liquid phase concentrations of the dyes,

respectively. V (l) is the volume of the solution, and W (g) is the mass of the TiO$_2$ thin film used.

4.2.3. Photoelectrochemical measurements of successive DSSCs

The two identical dye-adsorbed TiO$_2$ electrodes were sealed with a sealing sheet (SX 1170−60, Solaronix Co.), which served as a spacer. The electron transfer rates between the TiO$_2$ electrode and the electrolyte under the illuminated and dark conditions were obtained from the cyclic voltammograms (CVs) of a DSSC consisting of a TiO$_2$ photoanode, platinized counter electrode, and I^-/I_3^- redox couple electrolyte recorded at a scan rate of 100 mV/s. Electrochemical impedance spectroscopy (EIS) measurements were performed using an AC impedance (CH Instruments CHI 660E, USA) over the frequency range of 0.1 ~ 10^5 Hz with amplitudes of V$_{oc}$ ± 5 mV. The photovoltaic properties were investigated by measuring their current-voltage (I-V) characteristics under white-light irradiation from a 200-W xenon lamp (McScience, Korea). The obtained I-V curves were used to calculate the short-circuit current (I_{sc}), open-circuit voltage (V_{oc}), fill factor (FF), and overall conversion efficiency (η_{eff}) of the DSSCs.

4.3. Results and discussion

4.3.1. Adsorption study of nanoporous TiO₂ electrodes toward N719 and MK-2 dyes

It has been reported that the photovoltaic conversion efficiency is strongly influenced by the adsorption characteristics of the dye molecules and the electrochemical properties of the TiO_2 electrode. Therefore, it would be very meaningful to systematically examine the adsorption characteristics of the dyes onto the TiO_2 films. Many studies have been conducted on the adsorption equilibria and kinetics based on the differences in the amounts of dye adsorbed and subsequently desorbed onto TiO_2 thin films. However, as described in the experimental section, the adsorption kinetics data were directly obtained in a small adsorption chamber in the absence of a desorption step. The adsorption kinetics of N719 and MK-2 dyes on the TiO_2 film were obtained and then analyzed by employing a pseudo-second-order model. The kinetics data provide valuable information for understanding the mechanism of the sorption process [168]. Figure 4.6 shows the obtained concentration decay curves of the single-component adsorption of N719 and MK-2 onto the TiO_2 film obtained in a small adsorption chamber. The solid lines are the results simulated using the kinetics model. The kinetics data were analyzed with a pseudo-second-order model [168, 193].

$$\frac{dq}{dt} = k_2 \left(q_e - q_t\right)^2 \qquad \text{Equation 4.2}$$

where k_2 (g/mmol・min) is the second-order rate constant determined by the plot of t/q_t vs. t. Note that the correlation coefficients (R^2) of the pseudo-second-order model for the linear plots of TiO_2 were very close to 1. This result implies that the adsorption kinetics was successfully described by the pseudo-second-order model. As listed in Table 4.2, the determined rate constants of q_e and k_2 were in the ranges 0.410 ~ 2.787 mmol/g and 0.0049 ~ 0.3659 g/mmol/min, respectively.
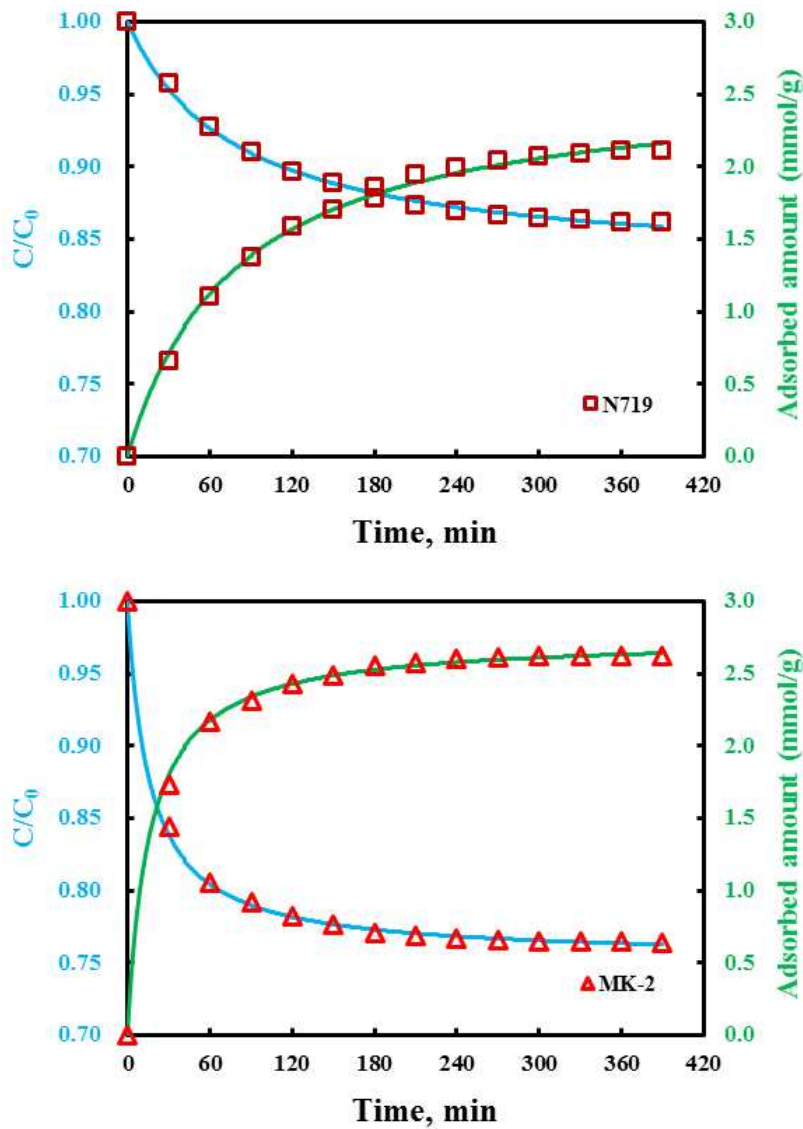
Figure 4.6. Adsorption kinetics of a single dye, N719 (a) or MK-2 (b), on TiO$_2$ electrodes.
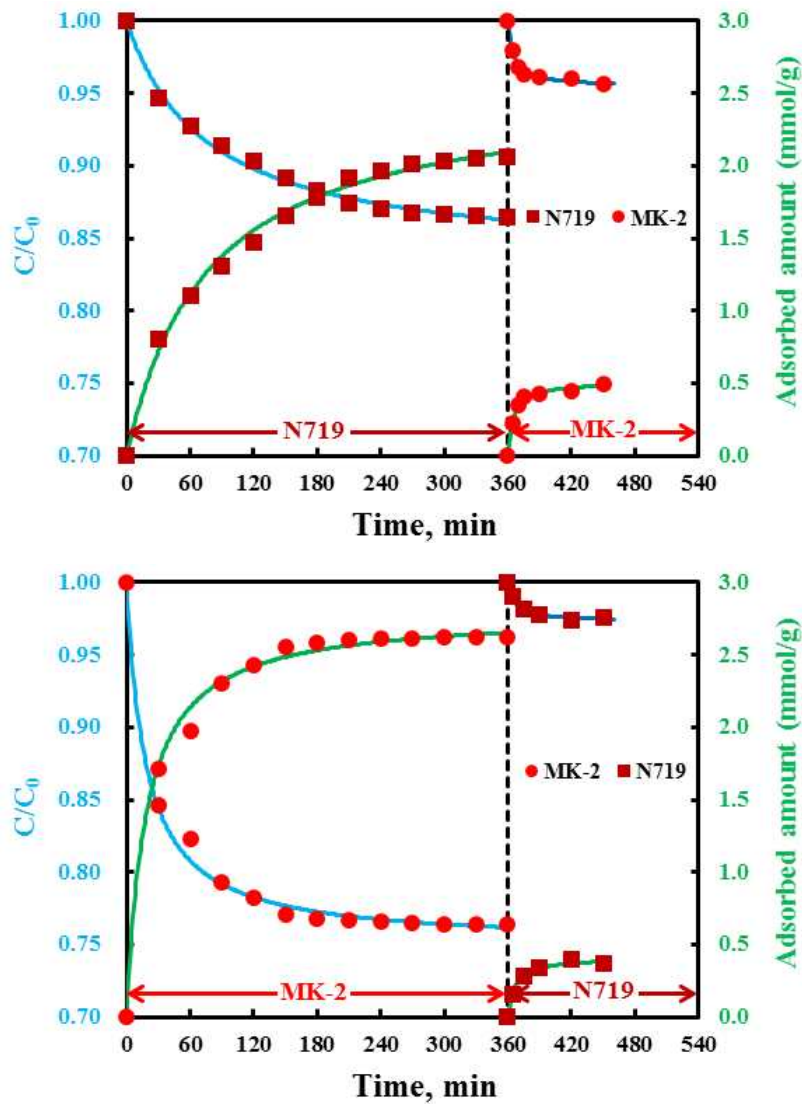
Figure 4.7. Successive adsorption kinetics of N719/MK-2(a) and MK-2/N719(b).

Table 4.2. Adsorption kinetics parameters of the adsorption of N719 and MK-2 dyes onto TiO$_2$ film

Samples		k_2 [g/mmol·min]	q_e [mmol/g]	R^2
N719	N	0.0049	2.594	1.00
MK-2	M	0.0233	2.745	1.00
N719/MK-2	N	0.0052	2.535	1.00
	M	0.3623	0.511	1.00
MK-2/N719	M	0.0197	2.787	1.00
	N	0.3659	0.41	0.99

The adsorption kinetics of MK-2 involving the anchorage of the long alkyl chains of the dye on the TiO$_2$ film surface was much greater than that of N719. Recently, Wei et al. reported the effects of rubrene co-sensitized TiO$_2$ photoanodes on the performance of ruthenium dye N719 sensitized solar cells. The result showed that rubrene is an efficient co-adsorbent for improving the performance of N719-sensitized solar cells [191]. However, unfavorable interactions between the two dye molecules often decreased the photovoltaic performance. It is well known that competitive adsorption generally occurs between binary components on the TiO$_2$ film during the adsorption process, unlike in single-component adsorption. To understand the adsorption mechanism, two successive adsorption cases were also employed: adsorption of N719 followed by MK-2 (N719/MK-2) and adsorption of MK-2 followed by N719 (MK-2/N719). Figure 4.7 shows that for the dye-bilayer formation, interesting results are observed for dye double-layer formation of the N719/MK-2 and MK-2/N719. Figure 4.7(b) shows the adsorption of MK-2 followed by the adsorption of N719 on the same TiO$_2$ film. In this case, MK-2 dye adsorbed at the TiO$_2$ surface was gradually replaced by N719. However, the N719/MK-2 sample showed that N719 adsorbed on the TiO$_2$ surface was not replaced by MK-2 because of the latter's lower adsorption (i.e., adsorption equilibrium) affinity on TiO$_2$ films (Figure 4.7(a)). This result implies that the adsorption affinity of N719 was higher than that of MK-2. However, the rate of adsorption of MK-2 on the nanoporous TiO$_2$ surface is faster than that of N719, which could be attributed to its smaller molecular size, leading to greater diffusion through the

nanoporous layer. The amounts of N719 and MK-2 adsorbed on the nanoporous TiO_2 surface can be successfully controlled based on the adsorption equilibria and kinetics differences of N719/MK-2 vs. MK-2/N719. In the case of the adsorption of N719 and successive adsorption of MK-2 on the same TiO_2 film, the adsorption capacities of former and latter were 2.535 mmol/g and 0.511 mmol/g, respectively. Meanwhile, for the adsorption of MK-2 and successive adsorption of N719 on the same TiO_2 film, the MK-2 and N719 adsorption capacities were 2.787 and 0.410 mg/g, respectively. It is interesting to compare the influence of the adsorption mode on the nanoporous TiO_2 surface.

4.3.2. Improvement of photovoltaic performance for DSSCs
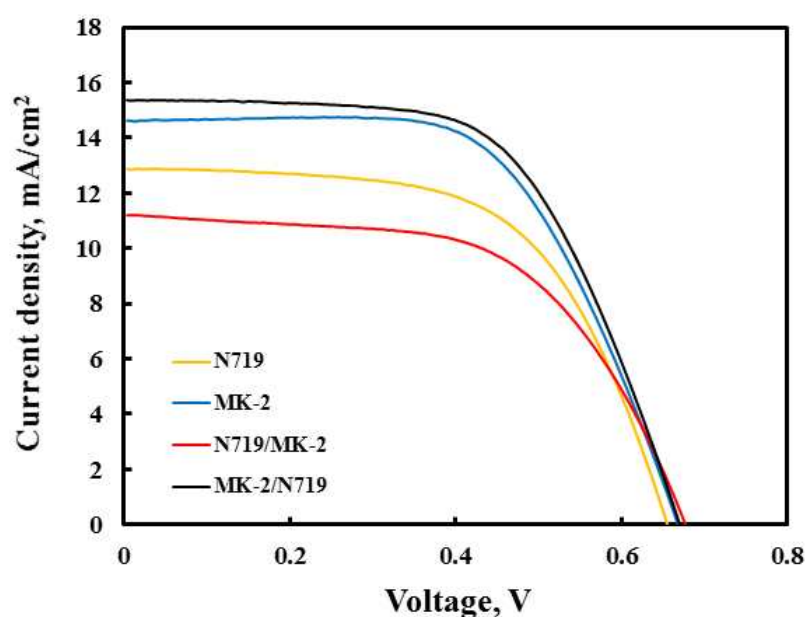
Figure 4.8. Photocurrent-voltage curves of DSSCs adsorbed with N719, MK-2, N719/MK-2, and MK-2/N719.

Table 4.3. Photocurrent-voltage (J-V) curves of N719 and MK-2 dyes

Samples	J_{sc} [mA/cm^2]	V_{oc} [V]	Fill Factor [%]	Efficiency [%]
N719	12.86	0.65	60	5.04
MK-2	14.74	0.66	61	5.94
N719/MK-2	11.2	0.67	58	4.41
MK-2/N719	15.39	0.67	61	6.22

The photocurrent-voltage curves and parameters obtained by recording the $I-V$ curves are shown in Figure 4.8 and listed in Table 4.3. The energy conversion efficiencies of the single-dye-sensitized solar cells based on N719 and MK-2 were 5.04% and 5.94%, respectively. Contrary to our expectations, the successive adsorption of the N719 and MK-2 dyes (i.e., N719/MK-2) showed a decreased photovoltaic conversion efficiency because of the unfavorable interactions between the two dyes [189]. However, the MK-2/N719 solar cell yielded a short-circuit current density (J_{sc}) of 15.39 mA/cm^2, an open-circuit photovoltage (V_{oc}) of 0.67 V, and a fill factor (FF) of 61%, corresponding to a higher energy conversion efficiency (η) of 6.22%.

Table 4.4. Internal resistance of the cells studied by impedance analysis

Samples	R_s [Ω]	R_{ct1} [Ω]	R_{ct2} [Ω]
N719	20.0	17.9	26.5
MK-2	20.3	19.9	26.0
N719/MK-2	18.3	20.6	33.6
MK-2/N719	18.0	19.9	25.2

To investigate the factors responsible for the improvement in cell performance, we conducted impedance analysis to investigate the internal resistance properties of the cells. The EIS fitting results are shown in Figure 4.9, and the analyzed data are summarized in

Table 4.4. Generally, the DSSC spectra exhibited two or three semicircles, which were assigned to the electrochemical reaction at the Pt counter electrode, charge transfer at the TiO_2/dye/electrolyte, and the Warburg diffusion process of I^-/I_3^- [194]. The circuit elements consisted of the interface charge-transfer resistance (R_{ct}), constant phase element (CPE), Warburg impedance (R_w), and series resistance (R_s). The R_{ct1} is the electron transfer resistance at the Pt/electrolyte interface, and the R_{ct2} is the electron transfer resistance at the TiO_2/dye/electrolyte interface.
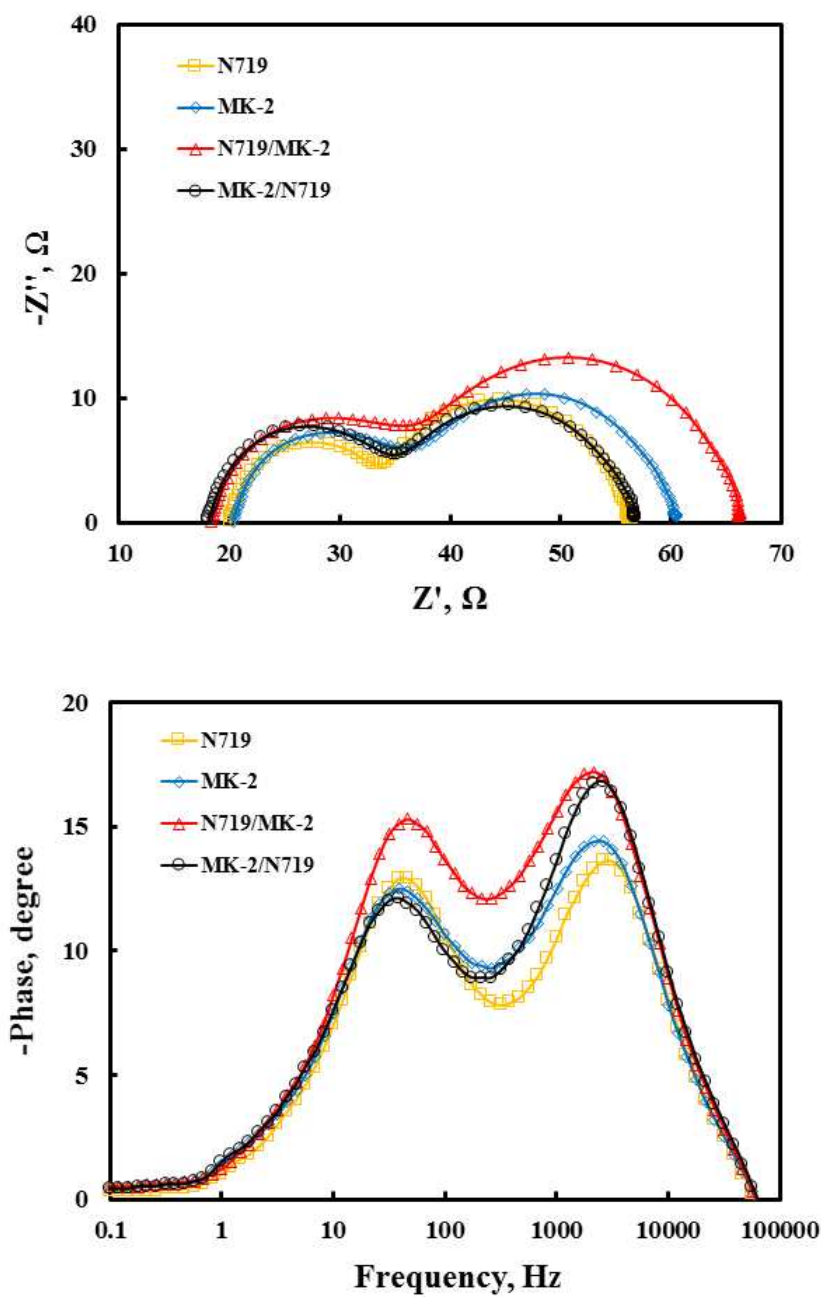
Figure 4.9. Nyquist plots (a) and Bode phase plots (b) of TiO$_2$ films adsorbed with N719, MK-2, N719/MK-2, and MK-2/N719.

The CPE reflects the interfacial capacitance, taking into account the roughness of the electrodes, which causes the semicircle to be depressed into an ellipse in the Nyquist plots [195]. The R_s values of the four cells, namely, 20.0 four cells, namely,t plots [1, were similar, as expected. The R_{ct1} values decreased obviously from 20.6 d.for N719/MK-2 to 17.9 y for N719. The trend correlated with the cell performance. The cell with N719/MK-2 as the sensitizer had an R_{ct2} (33.6 ly markedly higher than those of N719 (26.5 ed MK-2 (26.0 Ω), and MK-2/N719 (25.2 6.5 ed   difference in R_{ct2} can be associated with the binding between the dye molecules and TiO_2 because the two main dyes in the N719 and MK-2 extracts aggregated or mixed together on the TiO_2 films, leading to weaker binding and higher resistance. The high R_{ct2} led to a decrease in the J_{sc}. This may also explain why the efficiency of the cell based on N719/MK-2 was so low. Therefore, to improve the cell efficiency, it is necessary to improve the binding strength between the dyes and nanoporous TiO_2 surfaces.

CVs of the DSSC prepared using TiO_2 films of different adsorption modes are shown in Figure 4.10. The CVs do not include significant peaks, which would indicate oxidative-reductive processes, but they do show different current densities under the illuminated and dark conditions. This difference in current density (ΔI) with adsorption mode is ascribed to the different electron transfer rates between the TiO_2 electrode and the electrolyte. The values of ΔI are 12.86, 14.74, 11.20, and 15.39 mA/cm^2 for the N719, MK-2, N719/MK-2, and MK-2/N719 electrodes, respectively. The MK-2/N719 layered electrode has the highest electron transfer value, thus indicating improved dye regeneration and higher charge collection efficiency, which results in an increase in current density [129]. The diffusion length of the electron for the MK-2/N719 electrode is shorter than that for the N719/MK-2 electrode. When an MK-2/N719 electrode was used, the injected electrons did not reach the electrode and underwent electron recombination. Additionally, the different electron transfer rates between the TiO_2 electrode and the electrolyte optimized at the MK-2/N719 electrode according to the diffusion-limited current density (i_{lim}) were used to obtain the diffusion constant of I_3^-.
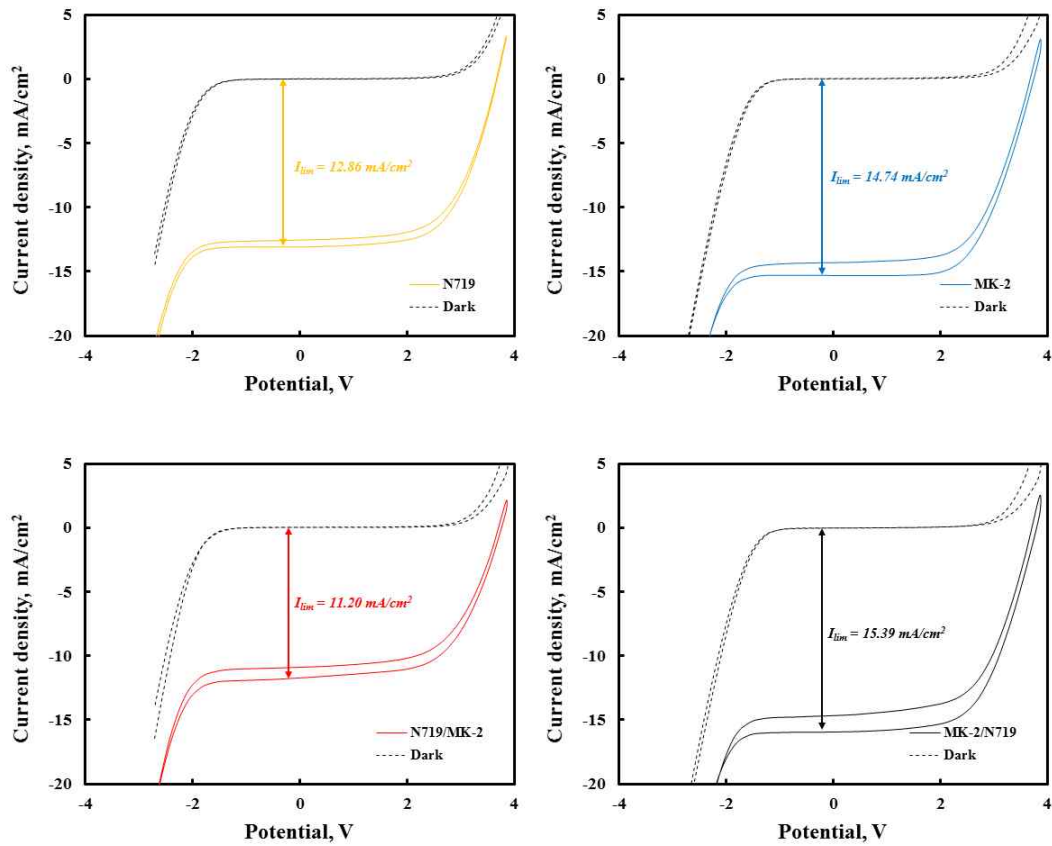
Figure 4.10. Cyclic voltammograms for DSSCs adsorbed with N719, MK-2, N719/MK-2, and MK-2/N719 electrodes at a scan rate of 100 mV/s.

4.4. Conclusions

To improve the photovoltaic conversion efficiency, a double layer of the N719 and MK-2 dyes as sensitizers was successfully formulated on the nanoporous TiO_2 surface. The adsorption properties of photoelectrodes that either adsorbed a single dye (N719 or MK-2) or underwent a successive adsorption of both dyes were compared with respect to electron generation and electron transfer. The energy conversion efficiency in terms of adsorption mode was in the range of 4.41 ~ 6.22%. The amounts of N719 and MK-2 dyes adsorbed on the nanoporous TiO_2 surface could be successfully controlled based on the adsorption equilibria and kinetics differences of the two dyes. The MK-2 dye was adsorbed faster and with weak binding to TiO_2, whereas the N719 dye diffused relatively slower but experienced stronger binding. The systematic studies of the adsorption equilibria and kinetics reported in this work can be widely applied for co-sensitized TiO_2 electrodes.

Chapter 5. Light-Harvesting over a Wide Wavelength Range using a Variety of Natural Dyes with Rainbow Dye-Sensitized Solar Cells

5.1. Introduction

Dye-sensitized solar cells (DSSCs) have attracted considerable attention due to their environmental-friendliness and low cost of production [171]. DSSCs consist of a nanocrystalline porous semiconductor oxide electrode, an adsorbed dye, an electrolyte, and a counter electrode [196]. Many metal complexes and organic dyes have been used as sensitizers in DSSCs. In general, the ruthenium dyes N719 and N3 are very expensive and environmentally toxic. Therefore, numerous metal-free organic dyes have been investigated as potential candidates in DSSCs [160]. Natural dyes provide a viable alternative to expensive organic-based DSSCs because of their cost-efficiency, non-toxicity, and complete biodegradation. Many natural dyes extracted from various plants, flowers, fruits, and leaves have been utilized as sensitizers in DSSCs.

The energy conversion efficiencies of natural dyes are much lower than those of organic dyes. To enhance the DSSC performance, some researchers have investigated dye cocktail solutions, which consists of two different dyes, one of which absorbs at a lower wavelength, to capture light from the visible to the near-infrared. Recently, DSSC performance enhancements using two or more dyes in such combinations have been reported [197]. Furthermore, it is well known that combinations of yellow, blue, and red give various green, violet, orange, and black colors (Figure 5.1). It is therefore useful to investigate the adsorption and electrochemical properties of two or three dyes on TiO$_2$ thin films for rainbow DSSCs.

The aim of this work was to enhance the photovoltaic performance based on the adsorption characteristics and electrochemical properties of dyes on TiO$_2$ thin films. To this end, adsorption kinetics data were obtained and analyzed using a pseudo-second-order model to clarify the adsorption mechanisms of gardenia yellow, blue, and red dye mixtures

for harvesting light over a wide wavelength range in rainbow DSSCs.
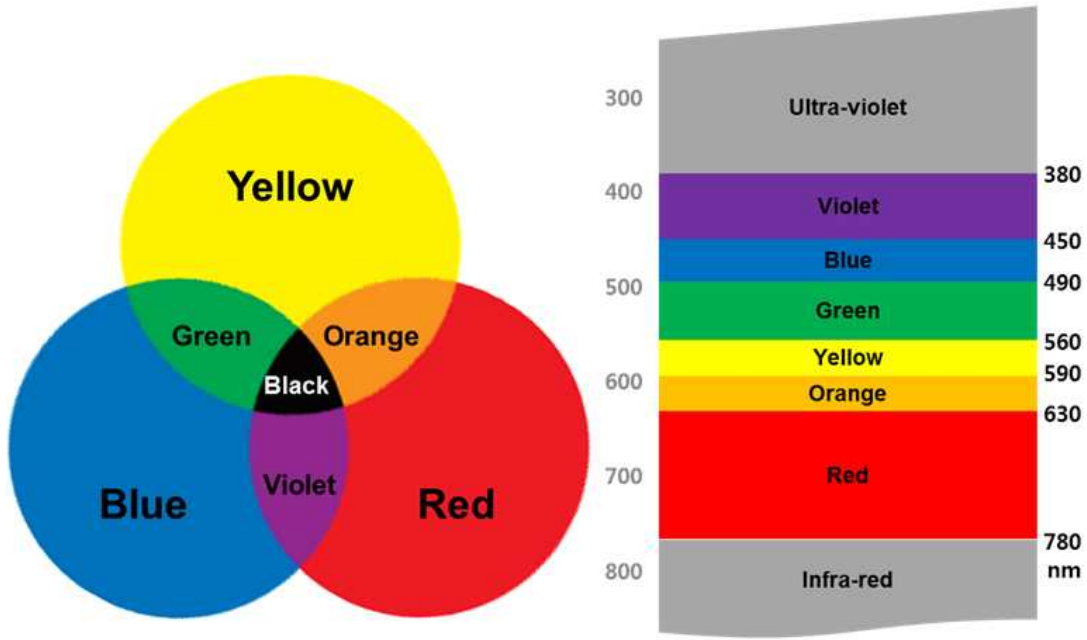
Figure 5.1. Wavelengths of rainbow colors.

Table 5.1. Wavelengths of rainbow colors

Wavelengths(nm)	Color	Wavelengths(nm)	Color
380~430	Bluish purple	558~569	Yellow green
430~467	Purplish blue	569~573	Greenish yellow
467~483	Blue	573~578	Yellow
483~488	Greenish blue	578~586	Yellowish orange
488~493	Blue green	586~597	Orange
493~498	Bluish green	597~640	Reddish orange
498~530	Green	640~780	Red
530~558	Yellowish green	-	-

5.2. Experimental

5.2.1. Fabrication of nanoporous TiO$_2$ electrodes for rainbow DSSCs

TiO$_2$ paste (DSL18NR-T, Dyesol co.) was used to prepare TiO$_2$ films for the DSSCs. The paste was coated on pre-cleaned fluorine-doped tin oxide (FTO) conducting glass (Pilkington, TEC-8, 80% transmittance in the visible region) by a squeeze-printing technique followed by annealing at 723.15 K for 30 min. TiO$_2$ photoelectrodes were deposited on FTO glass substrates with active areas of 2.0 × 2.0 cm^2 and 0.5 × 0.5 cm^2 for adsorption kinetics and photovoltaic efficiency measurements, respectively.
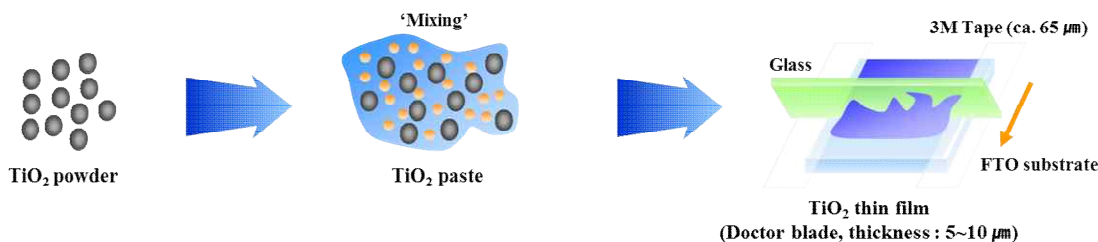
Figure 5.2. Preparation of TiO$_2$ film using the doctor blade method.

5.2.2. Adsorption properties of rainbow photoelectrodes

Natural yellow, blue, and red dyes from gardenia were purchased as powders from the Naju Nature Dyeing Culture Center (Korea). The dyes were dissolved in distilled water. The preparation of the electrode and electrolyte and the assembly of the rainbow DSSCs have been described in our previous work [198]. The adsorption kinetics experiments were conducted by immersing a TiO$_2$ cell with an active area of 4 cm^2 in a small adsorption chamber filled with an aqueous solution of gardenia dyes [168]. The amount of adsorption at time (q_t) was calculated using Equation 5.1:

$$q_t = (C_0 - C_t) \, V / W \qquad\qquad \text{Equation 5.1}$$

where C_0 and C_t are the liquid-phase concentrations (mg/L) of the natural dyes at the start and at time t, respectively; V is the volume of the solution; and W is the mass of adsorbent used. The concentrations of mixtures consisting of gardenia yellow, blue, and red (denoted by YBR) were determined from the Beer-Lambert law at 442, 582, and 530 nm using an ultraviolet (UV) spectrophotometer (Shimadzu UV-160A, Japan).

5.2.3. Characterization of rainbow DSSCs

The resulting concentration was analyzed based on the absorbance of the solution at 442 nm, 582 nm and 530 nm using a UV/vis spectrophotometer (Shimadzu UV-160A, Japan). Electrochemical impedance spectroscopy (EIS) measurements were performed using AC impedance (CH Instruments CHI 660E, USA) over the frequency range of $0.1 \sim 10^5$ Hz with amplitudes of $V_{oc} \pm 5$ mV. The current-voltage (*I-V*) curves were measured using white-light irradiation from a 200-W xenon lamp (McScience, Korea). The active cell area and the incident light intensity were 0.25 cm^2 and 100 mW/cm^2, respectively. The *J-V* curves were used to calculate the short-circuit current density (J_{sc}), open-circuit voltage (V_{oc}), fill factor (*FF*), and overall conversion efficiency (η_{eff}) of the DSSC.

5.3. Results and discussion

5.3.1. Characteristics of photoelectrode rainbow dyes

Figure 5.3 shows photographs and the UV-visible absorption spectra of the gardenia yellow, blue, and red dyes dissolved in aqueous solution. Clear differences among the absorption characteristics of the three dyes were observed. The absorption maxima for the yellow, blue, and red dyes were observed at wavelengths of approximately 442, 582, and 530 nm, respectively. Rainbow DSSCs with these three dyes adsorbed could therefore potentially be very effective for harvesting light over a wide range of wavelengths, resulting in higher photovoltaic conversion efficiencies. To systematically study the influence of the properties of the adsorption of the dye molecules onto the TiO_2 films on the power conversion efficiency of rainbow DSSCs, the effects on the DSSC photovoltaic performance of the quantity of dye adsorbed were analyzed.
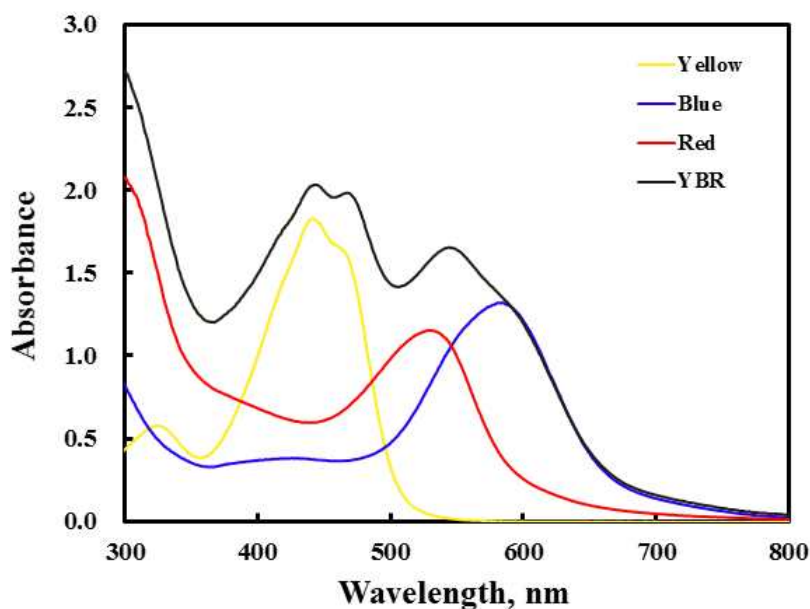
Figure 5.3. Absorption spectra of gardenia yellow, blue, and red and a mixture of the three dyes (YBR).

5.3.2. Improvement of the photovoltaic performance for DSSCs

Figure 5.4 shows the effect of the adsorption time (i.e., the adsorbed amount) on the I–V curves for a nanocrystalline solar cell. The short-circuit currents (J_{sc}), open-circuit voltages (V_{oc}), fill factors (FF), and overall conversion efficiencies (η_{eff}) of the rainbow DSSCs are summarized in Table 5.2. It is interesting to compare the amount of adsorbed dye with the photocurrent density of the corresponding DSSC. To control the adsorption amount, the working electrodes were immersed in cocktail dyes of yellow, red, and blue for different adsorption times (3, 6, 12, 24, 30, 36, 48, 72, 96, and 120 h) before constructing the cell.
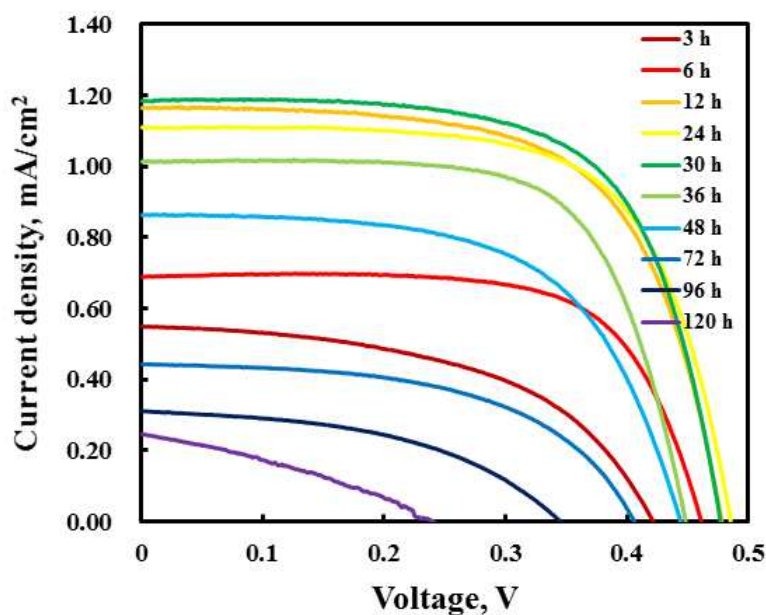
Figure 5.4. Photocurrent-voltage curves for YBR dye adsorption in terms of time.

As expected, the photocurrent density increased with increasing adsorption amount (i.e., adsorption time). The high adsorption capacity (i.e., increase in adsorption time up to 30 h) with low charge-transfer resistance may give rise to a superior J_{sc} for the rainbow DSSCs, most likely because of monolayer adsorption. However, the photocurrent density decreased with increasing immersion time (36 h). This result implies that dye molecules adsorbed on the surface negatively affected the charge-transfer resistance (i.e., dye agglomeration).

Table 5.2. Energy conversion efficiency of YBR dye adsorption in terms of time

Time [h]	J_{sc} [mA/cm^2]	V_{oc} [V]	Fill Factor [%]	Efficiency [%]
3	0.42	0.055	52	0.012
6	0.46	0.070	68	0.022
12	0.48	0.117	64	0.036
24	0.49	0.111	67	0.036
30	0.48	0.119	66	0.037
36	0.45	0.102	68	0.031
48	0.44	0.087	60	0.023
72	0.41	0.044	54	0.010
96	0.35	0.031	47	0.005
120	0.24	0.025	33	0.002
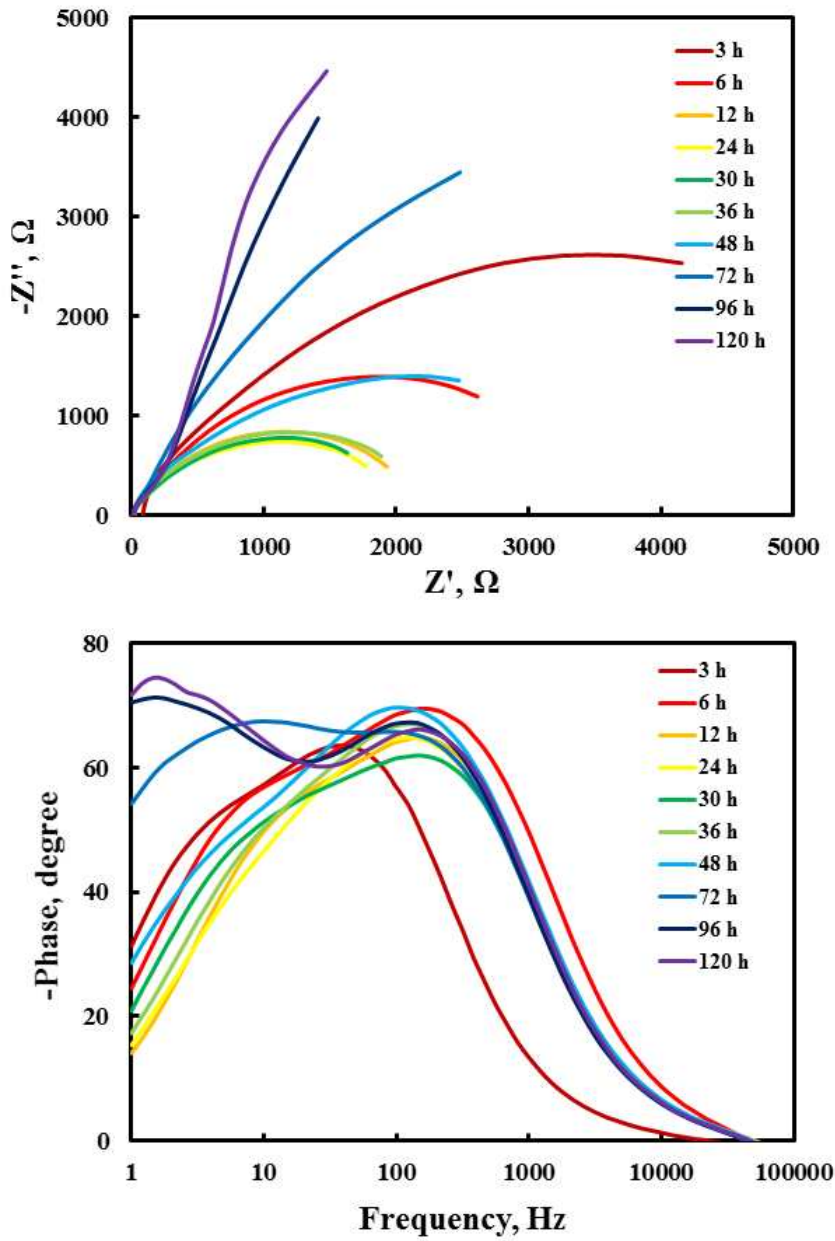
Figure 5.5. Nyquist plots of YBR dye in terms of adsorption time.

The Nyquist complex plane impedance plots, Z′ (real) versus Z″ (imaginary), are presented in Figure 5.5. The Nyquist plots for the rainbow DSSC in terms of adsorption time show that the resulting impedance spectra differ depending on adsorption time.

The R_{ct} value of the middle frequency range (1 ~ 1000 Hz) is the electron-transfer resistance at the TiO$_2$/rainbow dye/electrolyte interface. Variations in R_{ct} are associated with binding between the natural dye molecules and the TiO$_2$ film. The R_{ct} values decreased for adsorption times up to 30 h and then increased after 36 h, as cocktail dye aggregation on the TiO$_2$ films led to weaker binding and higher resistance. The series resistances (R_s) of the cells were similar for all adsorption times except 3 h (Table 5.3).

Table 5.3. Internal resistances determined by the impedance analysis of YBR dye in terms of adsorption time

Time [h]	R_s [Ω]	R_{ct} [kΩ]
3	87.3	2.03
6	14.2	3.88
12	22.1	1.80
24	21.8	1.71
30	17.3	1.56
36	18.6	1.57
48	18.2	2.48
72	17.2	7.15
96	17.1	14.01
120	18.2	15.28

5.3.3. Adsorption study of nanoporous TiO₂ electrodes on rainbow dyes

To avoid agglomeration of dye molecules, the dye adsorption should be conducted under supercritical conditions. The conversion efficiency of the rainbow DSSC was strongly dependent on the adsorption properties of the dye cocktail on the TiO_2 film. The adsorption kinetic data were directly obtained in a small adsorption chamber, without a desorption step. The adsorption kinetics of gardenia yellow, blue, and red dyes on a TiO_2 film from aqueous solutions were obtained and then analyzed using a pseudo-second-order model. Kinetic data provide valuable information for understanding the mechanism of sorption processes. Figure 5.6 shows the obtained concentration decay curves of the multicomponent adsorption of gardenia yellow, blue, and red on the TiO_2 film in a small adsorption chamber. The solid lines are the simulated results obtained using the kinetic model. With increasing time, the amounts of gardenia yellow, blue, and red dyes adsorbed gradually increased. The adsorption affinity of gardenia yellow, involving anchorage of the hydroxyl groups of the dye on the TiO_2 film surface, was much greater than those of gardenia blue and red. As expected, the adsorption of any of these three dyes was infl uenced by the other components. The adsorption capacities of gardenia yellow, blue, and red were 1532 mg/g, 262 mg/g, and 192 mg/g, respectively (Table 5.4). The adsorption kinetic values determined from the pseudo-second-order model were in the range 8.01 × 10^{-5} to 3.32 × 10^{-3} g/(mg min).

Table 5.4. Pseudo-second-order kinetic parameters of YBR dyes

Dye	k_2 [g/mg·min]	q_e [mg/g]	R^2
Yellow	8.01×10^{-5}	1532	0.96
Blue	9.13×10^{-4}	262	0.79
Red	3.32×10^{-3}	192	0.68
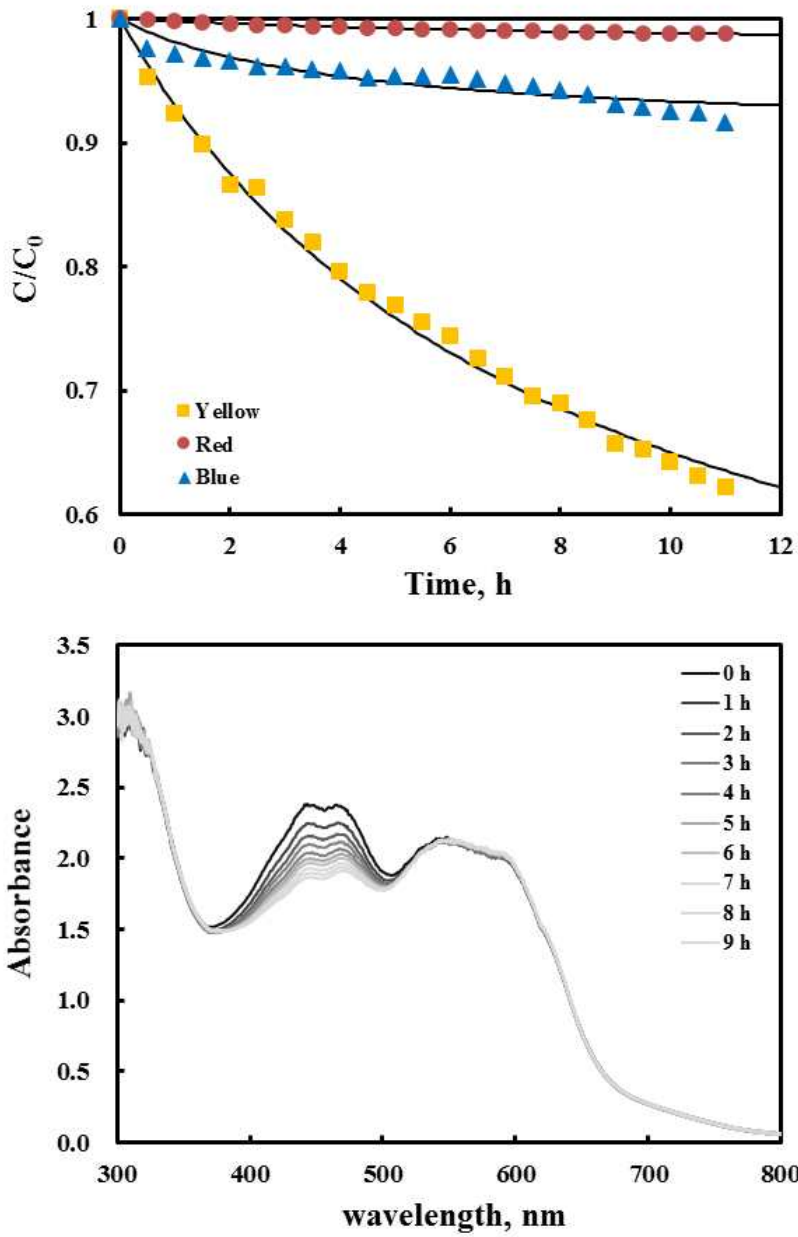
Figure 5.6. Adsorption kinetics (a) and absorption spectra (b) of YBR dye adsorption in terms of time.

5.3.4. Characteristics of commercial natural black dye

As shown in Figure 5.1, black can be obtained by mixing yellow, blue, and red. Figure 5.7(a) shows the absorption spectra of the commercial natural black dye dissolved in water at various concentrations from 78 to 5000 mg/L. Three sharp peaks were observed in the range 300 ~ 700 nm. Based on the fact that the black dye consisted of three dyes, namely gardenia yellow, blue, and red, we analyzed the concentration using the Beer-Lambert law.

Because the total absorbance (A_{total}) of the solution at a given wavelength is equal to the sum of the absorbances of the individual components (as in Equation 5.2), it is possible to analyze the individual constituents of a mixture, even when their spectra overlap.

$$A_{total} = ABS_1 + ABS_2 + ABS_3 \qquad \text{Equation 5.2}$$

Clearly, from Figure 5.7, every wavelength contains contributions from each of gardenia yellow (442 nm), blue (582 nm), and red (530 nm). To overcome this problem, we must first choose wavelengths that are well separated from another (i.e., λ_1, λ_2, and λ_3 in Figure 5.7)

The absorbance of a solution containing three chromophores, gardenia yellow (442 nm), blue (582 nm), and red (530 nm), is then equal to the sum of the absorbances of each of the components at λ_1, λ_2, and λ_3:

$$\lambda_1 : A^1 = \varepsilon_x^1 \cdot C_x + \varepsilon_y^1 \cdot C_y + \varepsilon_z^1 \cdot C_z \qquad \text{Equation 5.3}$$

$$\lambda_2 : A^2 = \varepsilon_x^2 \cdot C_x + \varepsilon_y^2 \cdot C_y + \varepsilon_z^2 \cdot C_z \qquad \text{Equation 5.4}$$

$$\lambda_3 : A^3 = \varepsilon_x^3 \cdot C_x + \varepsilon_y^3 \cdot C_y + \varepsilon_z^3 \cdot C_z \qquad \text{Equation 5.5}$$

Nine molar extinction coefficients (ε_x^1, ε_x^2, ε_x^3, ε_y^1, ε_y^2, ε_y^3, ε_z^1, ε_z^2 and ε_z^3) can

be derived from standard solutions containing only gardenia yellow (442 nm), blue (582 nm), and red (530 nm). Then, if the absorbances of the mixture are measured at λ_1, λ_2, and λ_3, the concentrations of the individual components can be calculated by solving the three simultaneous equations (Equations 5.3, 5.4, and 5.5) using the Gauss-Jordan method.

Before applying the law, we constructed calibration curves for pure gardenia yellow, blue, and red at 442, 582, and 530 nm (Table 5.5). The determined concentrations of the commercial black dye were 273 mg/L of yellow, 5868 mg/L of red, and 318 mg/L of blue. Figure 5.7(b) shows the absorption spectra of a synthetic YBR dye consisting of gardenia yellow (273 mg/L), blue (318 mg/L), and red (5,868 mg/L) dissolved in water. The spectra observed for the commercial black dye and synthetic black dye (YBR) were similar. These results suggest that the Beer-Lambert law can be successfully used to determine the concentrations of natural dye mixtures for rainbow DSSCs.

Table 5.5. Calibration parameters of gardenia yellow, blue, and red for the Beer-Lambert law

UV [nm]	Yellow [L/mg]	Blue [L/mg]	Red [L/mg]
442	2.385×10^{-3}	2.927×10^{-4}	3.010×10^{-5}
530	8.737×10^{-6}	6.474×10^{-4}	5.718×10^{-5}
582	8.308×10^{-6}	9.646×10^{-4}	2.069×10^{-5}
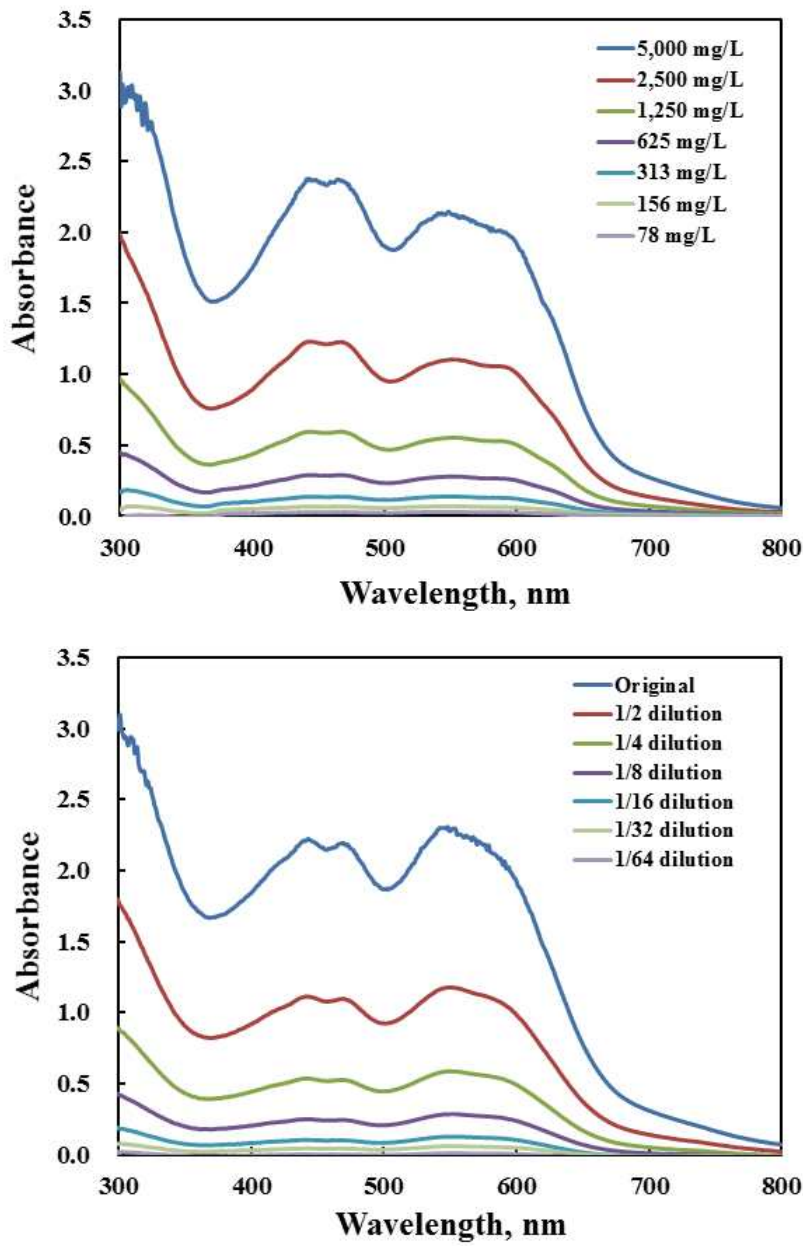
Figure 5.7. Absorption spectra of commercial black dye(a) and synthetic YBR dye(b).

5.4. Conclusions

We investigated rainbow DSSCs for light-harvesting over a wide wavelength range. It was found that a rainbow DSSC could be successfully produced using natural dyes, namely gardenia yellow, blue, and red. The adsorption capacities of gardenia yellow, blue, and red were 1532 mg/g, 262 mg/g, and 192 mg/g, respectively. The adsorption kinetics values determined from a pseudo-second-order model were in the range 8.01 es d^{-5} to 3.32 eter^{-3} g/(mg min). The photocurrent density decreased with increasing adsorption time (36 h). The conversion efficiency of the rainbow DSSCs was highly dependent on the adsorption properties of the cocktail dyes onto the TiO$_2$ films.

Chapter 6. Overall Conclusions

The studies conducted in this work mainly focused on comparing the adsorption properties of photoelectrodes that had adsorbed either a single dye or a mixture of the two and three dyes with respect to electron generation and electron transfer. The energy conversion efficiency in terms of adsorption mode (i.e., successive or cocktail adsorption) was measured. The amounts of dyes adsorbed on the nanoporous TiO_2 surface could be successfully controlled based on the adsorption equilibria and kinetics differences of two and three dyes. The first dye adsorbed faster and with weak binding to TiO_2, whereas the second dye diffused more slowly but with stronger binding. To improve the photovoltaic conversion efficiency, the dyes from adsorption mode as sensitizers were successfully formulated on the nanoporous TiO_2 surface to harvest light over a wide wavelength range. The systematic studies of the adsorption equilibria and kinetics obtained in this work can be widely applied for other DSSCs. According to the performed experiments and calculations, the following conclusions can be drawn.

■ **Hierarchically Structured Photoelectrode Biomimetic Replication from Butterfly Wings**
   ■ Fine hierarchical TiO_2 structures were successfully synthesized using butterfly-wing templates as biotemplates and used as a DSSC electrode.
      • The prepared samples have homogeneous pores, ca. 0.1 ~ 0.5 nm in size, and large pore volumes and surface areas.
      • BW-TiO_2 showed almost single-phase anatase TiO_2 (JCPDS no. 211272).
      • The average crystallite size of BW-TiO_2 is approximately 12.1 nm.
   ■ The photoelectrode performance is strongly dependent on the light adsorption and light-harvesting properties.
      • The band gaps for the NP-TiO_2 and BW-TiO_2 films were calculated to be 3.22 and 3.18 eV, respectively.
      • The electron lifetimes in NP-TiO_2 and BW-TiO_2 films determined from EIS measurements are 6.1 and 7.4 ms.

- The photovoltaic conversion efficiencies were found to be 3.48 and 4.32%, respectively.
- The hierarchical structures have an important and positive impact on light absorption and light-harvesting properties.

■ **Successive Adsorption of N719 and MK-2 for Co-Sensitization in Dye-Sensitized Solar Cells**

■ The systematic studies of the adsorption equilibria and kinetics obtained in this work can be widely applied for co-sensitized TiO_2 electrodes.

- The adsorption properties of photoelectrodes adsorbing either a single dye (N719 or MK-2) or two dyes successively were compared with respect to electron generation and electron transfer.
- The energy conversion efficiency in terms of adsorption mode was 4.41 ~ 6.22%.
- The determined rate constants of q_e and k_2 were approximately 2.594 mmol/g and 0.0049 g/mmol min (N719) and 2.745 mmol/g and 0.0233 g/mmol min (MK-2), respectively.
- The adsorption capacities of the former and latter were 2.535 mmol/g and 0.511 mmol/g, respectively. On the other hand, for the adsorption of MK-2 and successive adsorption of N719 on the same TiO_2 film, the MK-2 and N719 adsorption capacities were 2.787 mmol/g and 0.410 mg/g, respectively.
- The amounts of N719 and MK-2 dyes adsorbed on the nanoporous TiO_2 surface could be successfully controlled based on the adsorption equilibria and kinetics differences between the two dyes.
- The MK-2 dye adsorbed faster with weak binding to TiO_2, whereas the N719 dye diffused more slowly but with stronger binding.

■ **Light-Harvesting over a Wide Wavelength Range using a Variety of Natural Dyes by Rainbow Dye-Sensitized Solar Cells**

■ The conversion efficiency of the rainbow DSSC was strongly dependent on the adsorption properties of the cocktail dyes on TiO_2 films.

- The adsorption capacities of gardenia yellow, blue, and red were 1532 mg/g, 262

mg/g, and 192 mg/g, respectively.

- The adsorption kinetic values determined from a pseudo-second-order model were in the range of 8.01×10^{-5} to 3.32×10^{-3} g/(mg min).

- The photocurrent density decreased with increasing adsorption time (36 h).

- The determined concentrations of the commercial black dye were 237 mg/L of yellow, 5868 mg/L of red, and 318 mg/L of blue.

- The absorption spectra of a synthetic YBR dye consisting of gardenia yellow (237 mg/L), blue (318 mg/L), and red (5,868 mg/L) dissolved in water were recorded.

- The spectra observed for the commercial black dye and synthetic black dye (YBR) were similar. These results suggest that the Beer-Lambert law can be successfully used to determine the concentrations of natural dye mixtures for rainbow DSSCs.

- It was found that a rainbow DSSC could be successfully produced using natural dyes, namely gardenia yellow, blue, and red.

Literature Cited

[1] R.K. Pachauri, M. Allen, V. Barros, J. Broome, W. Cramer, R. Christ, J. Church, L. Clarke, Q. Dahe, P. Dasgupta, Climate Change 2014: Synthesis Report. Contribution of Working Groups I, II and III to the Fifth Assessment Report of the Intergovernmental Panel on Climate Change, (2014).

[2] A. Yadav, P. Kumar, ENHANCEMENT IN EFFICIENCY OF PV CELL THROUGH P&O ALGORITHM, International Journal For Technological Research In Engineering, 2 (2015) 2642-2644.

[3] R.N. Castellano, Solar Panel Processing, Archives contemporaines, 2010.

[4] B. Srinivas, S. Balaji, M. Nagendra Babu, Y. Reddy, Review on Present and Advance Materials for Solar Cells, International Journal of Engineering Research-Online, 3 (2015) 178-182.

[5] A. McEvoy, L. Castaner, T. Markvart, Solar cells: materials, manufacture and operation, Academic Press, 2012.

[6] R. Bube, Fundamentals of solar cells: photovoltaic solar energy conversion, Elsevier, 2012.

[7] T.M. Letcher, Future energy: improved, sustainable and clean options for our planet, Elsevier, 2008.

[8] M. Bertolli, Solar Cell Materials, Course: Solid State II. Department of Physics, University of Tennessee, Knoxville, (2008).

[9] A.M. Bagher, M.M.A. Vahid, M. Mohsen, Types of Solar Cells and Application, American Journal of Optics and Photonics, 3 (2015) 94-113.

[10] P.C.Choubey1, A.Oudhia1, R.Dewangan2, A review: Solar cell current scenario and future trends, Rec. Res. Sci. Tech, 4 (2012) 99-101.

[11] P. Würfel, U. Würfel, Physics of solar cells: from basic principles to advanced concepts, John Wiley & Sons, 2009.

[12] S. Dimitrijev, Principles of semiconductor devices, Oxford university press, 2012.

[13] P. Tomaszewski, Jan Czochralski i jego metoda, Jan Czochralski and his method, in, Wroclaw: Instytut Niskich Temperatur i Badan Strukturalnych PAN: Oficyna

Wydawnicza ATUT, Wroclawskie Wydawn. O'swiatowe, 2003.

[14] T. Saga, Advances in crystalline silicon solar cell technology for industrial mass production, NPG Asia Materials, 2 (2010) 96-102.

[15] P. Jayakumar, Resource assessment handbook, Asia and Pacific Center for Transfer of Technology (APCTT), (2009).

[16] K.L. Chopra, P.D. Paulson, V. Dutta, Thin-film solar cells: an overview, Progress in Photovoltaics: Research and Applications, 12 (2004) 69-92.

[17] J. Yang, A. Banerjee, S. Guha, Amorphous silicon based photovoltaics－from earth to the "final frontier", Solar energy materials and solar cells, 78 (2003) 597-612.

[18] C. Lund, K. Luczak, T. Pryor, J. Cornish, P. Jennings, P. Knipe, F. Ahjum, Field and laboratory studies of the stability of amorphous silicon solar cells and modules, Renewable Energy, 22 (2001) 287-294.

[19] Y. Tawada, H. Yamagishi, Mass-production of large size a-Si modules and future plan, Solar energy materials and solar cells, 66 (2001) 95-105.

[20] F. Kreith, D.Y. Goswami, Handbook of energy efficiency and renewable energy, (2007).

[21] S.S. Hegedus, A. Luque, Status, Trends, Challenges and the Bright Future of Solar Electricity from Photovoltaics, in: Handbook of Photovoltaic Science and Engineering, John Wiley & Sons, Ltd, 2005, pp. 1-43.

[22] K. Elsabawy, W. El-Hawary, M. Refat, ADVANCED SYNTHESIS OF TITANIUM-DOPED-TELLERIUM-CADMIUM MIXTURES FOR HIGH PERFORMANCE SOLAR CELL APPLICATIONS AS ONE OF RENEWABLE SOURCE OF ENERGY, International Journal of Chemical Sciences, 10 (2012) 1869-1879.

[23] W.A. Badawy, A review on solar cells from Si-single crystals to porous materials and quantum dots, Journal of Advanced Research, 6 (2015) 123-132.

[24] V. Sethi, M. Pandey, M.P. Shukla, Use of nanotechnology in solar PV cell, International journal of chemical engineering and applications, 2 (2011) 77.

[25] T.M. Razykov, C.S. Ferekides, D. Morel, E. Stefanakos, H.S. Ullal, H.M. Upadhyaya, Solar photovoltaic electricity: Current status and future prospects, Solar Energy, 85 (2011) 1580-1608.

[26] M. Imamzai, M. Aghaei, Y. Hanum Md Thayoob, M. Forouzanfar, A Review on Comparison between Traditional Silicon Solar Cells and Thin-Film CdTe Solar Cells, in: Proceedings of National Graduate Conference (NatGrad 2012), Tenaga Nasional Universiti, Putrajaya Campus, 2012, pp. 8-10.

[27] H. Hoppe, N.S. Sariciftci, Polymer Solar Cells, in: S.R. Marder, K.-S. Lee (Eds.) Photoresponsive Polymers II, Springer Berlin Heidelberg, Berlin, Heidelberg, 2008, pp. 1-86.

[28] S. Dubey, J.N. Sarvaiya, B. Seshadri, Temperature Dependent Photovoltaic (PV) Efficiency and Its Effect on PV Production in the World – A Review, Energy Procedia, 33 (2013) 311-321.

[29] B. Ganesh, Y.V. Supriya, G. Vaddeswaram, Recent Advancements and Techniques in Manufacture of Solar Cells: Organic Solar Cells, International Journal of Electronics and Computer Science Engineering, 2 (2013) 565-573.

[30] R. Janssen, Introduction to polymer solar cells, Eindhoven University of Technology, Netherlands, (2005).

[31] L. Francis, R. Claude, The Nobel Laureates in Chemistry (1901 - 2001), in: A Century of Nobel Prize Recipients, CRC Press, 2003.

[32] A.C. Mayer, S.R. Scully, B.E. Hardin, M.W. Rowell, M.D. McGehee, Polymer-based solar cells, Materials Today, 10 (2007) 28-33.

[33] F. Wudl, G. Srdanov, Conducting polymer formed of poly(2-methoxy,5-(2'-ethyl-hexyloxy)-p-phenylenevinylene), in, Google Patents, 1993.

[34] G. Li, R. Zhu, Y. Yang, Polymer solar cells, Nat Photon, 6 (2012) 153-161.

[35] C.J. Brabec, S.E. Shaheen, C. Winder, N.S. Sariciftci, P. Denk, Effect of LiF/metal electrodes on the performance of plastic solar cells, Applied Physics Letters, 80 (2002) 1288-1290.

[36] R. Zhu, A. Kumar, Y. Yang, Polarizing Organic Photovoltaics, Advanced Materials, 23 (2011) 4193-4198.

[37] B. Li, L. Wang, B. Kang, P. Wang, Y. Qiu, Review of recent progress in solid-state dye-sensitized solar cells, Solar Energy Materials and Solar Cells, 90 (2006) 549-573.

[38] J. Zahn, P. Sun, S. Jiang, X. Sun, An investigation of the performance of dye-sensitized nanocrystalline solar cell with anthocyanin dye and ruthenium dye as

the sensitizers, (2006).

[39] M. Graetzel, R.A.J. Janssen, D.B. Mitzi, E.H. Sargent, Materials interface engineering for solution-processed photovoltaics, Nature, 488 (2012) 304-312.

[40] A.J. Nozik, Nanoscience and Nanostructures for Photovoltaics and Solar Fuels, Nano Letters, 10 (2010) 2735-2741.

[41] S. Suhaimi, M.M. Shahimin, Z. Alahmed, J. Chysky, A. Reshak, Materials for enhanced dye-sensitized solar cell performance: electrochemical application, International Journal of Electrochemical Science, 10 (2015) 28-59.

[42] M. Liang, W. Xu, F. Cai, P. Chen, B. Peng, J. Chen, Z. Li, New Triphenylamine-Based Organic Dyes for Efficient Dye-Sensitized Solar Cells, The Journal of Physical Chemistry C, 111 (2007) 4465-4472.

[43] P.R.F. Barnes, A.Y. Anderson, S.E. Koops, J.R. Durrant, B.C. O'Regan, Electron Injection Efficiency and Diffusion Length in Dye-Sensitized Solar Cells Derived from Incident Photon Conversion Efficiency Measurements, The Journal of Physical Chemistry C, 113 (2009) 1126-1136.

[44] S. Philipps, A. Bett, K. Horowitz, S. Kurtz, Current status of concentrator photovoltaic (CPV) technology, in, National Renewable Energy Laboratory (NREL), Golden, CO., 2015.

[45] P.R. Mohanta, J. Patel, J. Bhuva, M. Gandhi, A Review on Solar Photovoltaics and Roof Top Application of It, International Journal of Advanced Research in Science, Engineering and Technology, 2 (2015) 2394-2444.

[46] N. Ahn, D.-Y. Son, I.-H. Jang, S.M. Kang, M. Choi, N.-G. Park, Highly Reproducible Perovskite Solar Cells with Average Efficiency of 18.3% and Best Efficiency of 19.7% Fabricated via Lewis Base Adduct of Lead(II) Iodide, Journal of the American Chemical Society, 137 (2015) 8696-8699.

[47] D. Shi, Y. Zeng, W. Shen, Perovskite/c-Si tandem solar cell with inverted nanopyramids: realizing high efficiency by controllable light trapping, Scientific Reports, 5 (2015) 16504.

[48] U. Mehmood, S.-u. Rahman, K. Harrabi, I.A. Hussein, B. Reddy, Recent advances in dye sensitized solar cells, Advances in Materials Science and Engineering, 2014 (2014).

[49] J. Gong, J. Liang, K. Sumathy, Review on dye-sensitized solar cells (DSSCs): Fundamental concepts and novel materials, Renewable and Sustainable Energy Reviews, 16 (2012) 5848-5860.

[50] C. Sima, C. Grigoriu, S. Antohe, Comparison of the dye-sensitized solar cells performances based on transparent conductive ITO and FTO, Thin Solid Films, 519 (2010) 595-597.

[51] T.N. Murakami, Y. Kijitori, N. Kawashima, T. Miyasaka, Low temperature preparation of mesoporous TiO2 films for efficient dye-sensitized photoelectrode by chemical vapor deposition combined with UV light irradiation, Journal of Photochemistry and Photobiology A: Chemistry, 164 (2004) 187-191.

[52] S. Ito, N.L. Ha, G. Rothenberger, P. Liska, P. Comte, S.M. Zakeeruddin, P. Pechy, M.K. Nazeeruddin, M. Gratzel, High-efficiency (7.2%) flexible dye-sensitized solar cells with Ti-metal substrate for nanocrystalline-TiO2 photoanode, Chemical communications (Cambridge, England), (2006) 4004-4006.

[53] Y. Jun, J. Kim, M.G. Kang, A study of stainless steel-based dye-sensitized solar cells and modules, Solar Energy Materials and Solar Cells, 91 (2007) 779-784.

[54] A. Braga, C. Baratto, E. Bontempi, P. Colombi, G. Sberveglieri, Transparent front contact optimization in dye sensitized solar cells: use of cadmium stannate and titanium oxide by sputtering, Thin Solid Films, 555 (2014) 18-20.

[55] M.R. Hoffmann, S.T. Martin, W. Choi, D.W. Bahnemann, Environmental Applications of Semiconductor Photocatalysis, Chemical Reviews, 95 (1995) 69-96.

[56] O. Lupan, V. Guérin, I. Tiginyanu, V. Ursaki, L. Chow, H. Heinrich, T. Pauporté, Well-aligned arrays of vertically oriented ZnO nanowires electrodeposited on ITO-coated glass and their integration in dye sensitized solar cells, Journal of Photochemistry and Photobiology A: Chemistry, 211 (2010) 65-73.

[57] D.-W. Han, J.-H. Heo, D.-J. Kwak, C.-H. Han, Y.-M. Sung, Texture, Morphology and Photovoltaic Characteristics of Nanoporous F:SnO2 Films, Journal of electrical engineering & technology, 4 (2009) 93-97.

[58] Y. Chergui, D. Mekki, N. Nehaoua, Comparative Study of Dye-Sensitized Solar Cell Based on ZnO and TiO2 Nanostructures, INTECH Open Access Publisher, 2011.

[59] Y. Fukai, Y. Kondo, S. Mori, E. Suzuki, Highly efficient dye-sensitized SnO2 solar

cells having sufficient electron diffusion length, Electrochemistry Communications, 9 (2007) 1439-1443.

[60] C. Bauer, G. Boschloo, E. Mukhtar, A. Hagfeldt, Ultrafast studies of electron injection in Ru dye sensitized SnO2 nanocrystalline thin film, International Journal of Photoenergy, 4 (2002).

[61] B. O'Regan, M. Gratzel, A low-cost, high-efficiency solar cell based on dye-sensitized colloidal TiO2 films, Nature, 353 (1991) 737-740.

[62] M.-I. Baraton, Nano-TiO2 for solar cells and photocatalytic water splitting: scientific and technological challenges for commercialization, Open Nanosci. J, 5 (2011) 64-77.

[63] K. Thamaphat, P. Limsuwan, B. Ngotawornchai, Phase characterization of TiO2 powder by XRD and TEM, Kasetsart J.(Nat. Sci.), 42 (2008) 357-361.

[64] S. Mi Yeon, K. Do Kyun, I. Kyo Jin, J. Seong Mu, K. Dong Young, Electrospun TiO 2 electrodes for dye-sensitized solar cells, Nanotechnology, 15 (2004) 1861.

[65] M. Adachi, Y. Murata, J. Takao, J. Jiu, M. Sakamoto, F. Wang, Highly Efficient Dye-Sensitized Solar Cells with a Titania Thin-Film Electrode Composed of a Network Structure of Single-Crystal-like TiO2 Nanowires Made by the "Oriented Attachment" Mechanism, Journal of the American Chemical Society, 126 (2004) 14943-14949.

[66] S.C. Yang, D.J. Yang, J. Kim, J.M. Hong, H.G. Kim, I.D. Kim, H. Lee, Hollow TiO2 Hemispheres Obtained by Colloidal Templating for Application in Dye Sensitized Solar Cells, Advanced Materials, 20 (2008) 1059-1064.

[67] H.J. Koo, Y.J. Kim, Y.H. Lee, W.I. Lee, K. Kim, N.G. Park, Nano embossed Hollow Spherical TiO2 as Bifunctional Material for High Efficiency Dye Sensitized Solar Cells, Advanced Materials, 20 (2008) 195-199.

[68] H. Park, W.-R. Kim, H.-T. Jeong, J.-J. Lee, H.-G. Kim, W.-Y. Choi, Fabrication of dye-sensitized solar cells by transplanting highly ordered TiO2 nanotube arrays, Solar Energy Materials and Solar Cells, 95 (2011) 184-189.

[69] K.D. Seo, H.M. Song, M.J. Lee, M. Pastore, C. Anselmi, F. De Angelis, M.K. Nazeeruddin, M. Gräetzel, H.K. Kim, Coumarin dyes containing low-band-gap chromophores for dye-sensitised solar cells, Dyes and Pigments, 90 (2011) 304-310.

[70] Z.-S. Wang, H. Kawauchi, T. Kashima, H. Arakawa, Significant influence of TiO2

photoelectrode morphology on the energy conversion efficiency of N719 dye-sensitized solar cell, Coordination Chemistry Reviews, 248 (2004) 1381-1389.

[71] Q. Zhang, G. Cao, Nanostructured photoelectrodes for dye-sensitized solar cells, Nano Today, 6 (2011) 91-109.

[72] J.-Y. Liao, J.-W. He, H. Xu, D.-B. Kuang, C.-Y. Su, Effect of TiO 2 morphology on photovoltaic performance of dye-sensitized solar cells: nanoparticles, nanofibers, hierarchical spheres and ellipsoid spheres, Journal of Materials Chemistry, 22 (2012) 7910-7918.

[73] Y. Saito, S. Kambe, T. Kitamura, Y. Wada, S. Yanagida, Morphology control of mesoporous TiO2 nanocrystalline films for performance of dye-sensitized solar cells, Solar Energy Materials and Solar Cells, 83 (2004) 1-13.

[74] L. Feng, J. Jia, Y. Fang, X. Zhou, Y. Lin, TiO2 flowers and spheres for ionic liquid electrolytes based dye-sensitized solar cells, Electrochimica Acta, 87 (2013) 629-636.

[75] C.-S. Chou, F.-C. Chou, J.-Y. Kang, Preparation of ZnO-coated TiO2 electrodes using dip coating and their applications in dye-sensitized solar cells, Powder Technology, 215‑216 (2012) 38-45.

[76] T.-Y. Cho, K.-W. Ko, S.-G. Yoon, S.S. Sekhon, M.G. Kang, Y.-S. Hong, C.-H. Han, Efficiency enhancement of flexible dye-sensitized solar cell with sol‑gel formed Nb2O5 blocking layer, Current Applied Physics, 13 (2013) 1391-1396.

[77] G. Kumara, K. Tennakone, V. Perera, A. Konno, S. Kaneko, M. Okuya, Suppression of recombinations in a dye-sensitized photoelectrochemical cell made from a film of tin IV oxide crystallites coated with a thin layer of aluminium oxide, Journal of Physics D: Applied Physics, 34 (2001) 868.

[78] T.-V. Nguyen, H.-C. Lee, M. Alam Khan, O.B. Yang, Electrodeposition of TiO2/SiO2 nanocomposite for dye-sensitized solar cell, Solar Energy, 81 (2007) 529-534.

[79] E. Palomares, J.N. Clifford, S.A. Haque, T. Lutz, J.R. Durrant, Control of charge recombination dynamics in dye sensitized solar cells by the use of conformally deposited metal oxide blocking layers, Journal of the American Chemical Society, 125 (2003) 475-482.

[80] H. Choi, C. Nahm, J. Kim, J. Moon, S. Nam, D.-R. Jung, B. Park, The effect of TiCl4-treated TiO2 compact layer on the performance of dye-sensitized solar cell,

Current Applied Physics, 12 (2012) 737-741.

[81] L. Vesce, R. Riccitelli, G. Soscia, T.M. Brown, A. Di Carlo, A. Reale, Optimization of nanostructured titania photoanodes for dye-sensitized solar cells: Study and experimentation of TiCl4 treatment, Journal of Non-Crystalline Solids, 356 (2010) 1958-1961.

[82] H. Melhem, P. Simon, J. Wang, C. Di Bin, B. Ratier, Y. Leconte, N. Herlin-Boime, M. Makowska-Janusik, A. Kassiba, J. Bouclé, Direct photocurrent generation from nitrogen doped TiO2 electrodes in solid-state dye-sensitized solar cells: Towards optically-active metal oxides for photovoltaic applications, Solar Energy Materials and Solar Cells, 117 (2013) 624-631.

[83] P. Suri, M. Panwar, R. Mehra, Photovoltaic performance of dye-sensitized ZnO solar cell based on Eosin-Y photosensitizer, Materials Science-Poland, 25 (2007) 137-144.

[84] M. Law, L.E. Greene, J.C. Johnson, R. Saykally, P. Yang, Nanowire dye-sensitized solar cells, Nat Mater, 4 (2005) 455-459.

[85] Q. Peng, Y. Qin, ZnO nanowires and their application for solar cells, INTECH Open Access Publisher, 2011.

[86] L. Giribabu, V.K. Singh, T. Jella, Y. Soujanya, A. Amat, F. De Angelis, A. Yella, P. Gao, M.K. Nazeeruddin, Sterically demanded unsymmetrical zinc phthalocyanines for dye-sensitized solar cells, Dyes and Pigments, 98 (2013) 518-529.

[87] P. Balraju, M. Kumar, M. Roy, G. Sharma, Dye sensitized solar cells (DSSCs) based on modified iron phthalocyanine nanostructured TiO 2 electrode and PEDOT: PSS counter electrode, Synthetic Metals, 159 (2009) 1325-1331.

[88] H. Huang, Z. Cao, X. Li, L. Zhang, X. Liu, H. Zhao, S. Tan, Synthesis and photovoltaic properties of two new unsymmetrical zinc-phthalocyanine dyes, Synthetic Metals, 162 (2012) 2316-2321.

[89] K. Hara, Y. Tachibana, Y. Ohga, A. Shinpo, S. Suga, K. Sayama, H. Sugihara, H. Arakawa, Dye-sensitized nanocrystalline TiO2 solar cells based on novel coumarin dyes, Solar Energy Materials and Solar Cells, 77 (2003) 89-103.

[90] K.R. Justin Thomas, P. Singh, A. Baheti, Y.-C. Hsu, K.-C. Ho, J.T.s. Lin, Electro-optical properties of new anthracene based organic dyes for dye-sensitized solar cells, Dyes and Pigments, 91 (2011) 33-43.

[91] J.A. Mikroyannidis, D.V. Tsagkournos, S.S. Sharma, A. Kumar, Y.K. Vijay, G.D. Sharma, Efficient bulk heterojunction solar cells based on low band gap bisazo dyes containing anthracene and/or pyrrole units, Solar Energy Materials and Solar Cells, 94 (2010) 2318-2327.

[92] N. Xiang, W. Zhou, S. Jiang, L. Deng, Y. Liu, Z. Tan, B. Zhao, P. Shen, S. Tan, Synthesis and characterization of trivalent metal porphyrin with NCS ligand for application in dye-sensitized solar cells, Solar Energy Materials and Solar Cells, 95 (2011) 1174-1181.

[93] M.K. Panda, K. Ladomenou, A.G. Coutsolelos, Porphyrins in bio-inspired transformations: Light-harvesting to solar cell, Coordination Chemistry Reviews, 256 (2012) 2601-2627.

[94] W. Zhou, B. Zhao, P. Shen, S. Jiang, H. Huang, L. Deng, S. Tan, Multi-alkylthienyl appended porphyrins for efficient dye-sensitized solar cells, Dyes and Pigments, 91 (2011) 404-412.

[95] K. Kalyanasundaram, M. Grätzel, Efficient dye-sensitized solar cells for direct conversion of sunlight to electricity, Material Matters, 4 (2009) 88-90.

[96] S.A. Taya, T.M. El-Agez, H.S. El-Ghamri, M.S. Abdel-Latif, Dye-sensitized solar cells using fresh and dried natural dyes, International Journal of Materials Science and Applications, 2 (2013) 37-42.

[97] D. Wei, Dye sensitized solar cells, International journal of molecular sciences, 11 (2010) 1103-1113.

[98] D. LEE, Plant pigments and their manipulation. Annual Plant Reviews Vol 12. Davies KM, ed. 2004. Oxford/Boca Raton: Blackwell Publishing/CRC Press, Boca Raton. £110 (hardback). 352 pp, Annals of Botany, 96 (2005) 1332-1333.

[99] G. Calogero, G. Di Marco, S. Cazzanti, S. Caramori, R. Argazzi, A. Di Carlo, C.A. Bignozzi, Efficient dye-sensitized solar cells using red turnip and purple wild sicilian prickly pear fruits, International journal of molecular sciences, 11 (2010) 254-267.

[100] Q. Dai, J. Rabani, Unusually efficient photosensitization of nanocrystalline TiO_2 films by pomegranate pigments in aqueous medium, New Journal of Chemistry, 26 (2002) 421-426.

[101] S. Suhaimi, M.M. Shahimin, I.S. Mohamad, M.N. Norizan, Comparative study of

natural anthocyanins compound as photovoltaic sensitizer, Advances in Environmental Biology, 7 (2013) 3617-3620.

[102] R. Hemmatzadeh, A. Mohammadi, Improving optical absorptivity of natural dyes for fabrication of efficient dye-sensitized solar cells, Journal of Theoretical and Applied Physics, 7 (2013) 1-7.

[103] M.R. Narayan, Review: Dye sensitized solar cells based on natural photosensitizers, Renewable and Sustainable Energy Reviews, 16 (2012) 208-215.

[104] R. Ahmad, M. Ali, N. Nafarizal, Fabrication and analysis of dye-sensitized solar cell using natural dye extracted from dragon fruit, International Journal of Integrated Engineering, 3 (2010) 1-8.

[105] H. Chang, M.-J. Kao, T.-L. Chen, C.-H. Chen, K.-C. Cho, X.-R. Lai, Characterization of Natural Dye Extracted from Wormwood and Purple Cabbage for Dye-Sensitized Solar Cells, International Journal of Photoenergy, 2013 (2013) 8.

[106] A.K. Alaba, Utilization of natural Morinda lucida as photosensitizers for dye-sensitized solar cell, Arch Appl Sci Res, 4 (2012) 419-425.

[107] K. Moustafa, M. Rekaby, E. El Shenawy, N. Khattab, Green dyes as photosensitizers for dye-sensitized solar cells, Journal of Applied Sciences Research, 8 (2012) 4393-4404.

[108] H. Kusama, H. Arakawa, Influence of pyrazole derivatives in I-/I-3(-) redox electrolyte solution on Ru(II)-dye-sensitized TiO2 solar cell performance, Solar Energy Materials and Solar Cells, 85 (2005) 333-344.

[109] A.F. Nogueira, C. Longo, M.A. De Paoli, Polymers in dye sensitized solar cells: overview and perspectives, Coordination Chemistry Reviews, 248 (2004) 1455-1468.

[110] Z.-S. Wang, K. Sayama, H. Sugihara, Efficient Eosin Y Dye-Sensitized Solar Cell Containing Br-/Br3- Electrolyte, The Journal of Physical Chemistry B, 109 (2005) 22449-22455.

[111] B.V. Bergeron, A. Marton, G. Oskam, G.J. Meyer, Dye-Sensitized SnO2 Electrodes with Iodide and Pseudohalide Redox Mediators, The Journal of Physical Chemistry B, 109 (2005) 937-943.

[112] G. Oskam, B.V. Bergeron, G.J. Meyer, P.C. Searson, Pseudohalogens for dye-sensitized TiO2 photoelectrochemical cells, The Journal of Physical Chemistry B,

105 (2001) 6867-6873.

[113] S.A. Sapp, C.M. Elliott, C. Contado, S. Caramori, C.A. Bignozzi, Substituted Polypyridine Complexes of Cobalt(II/III) as Efficient Electron-Transfer Mediators in Dye-Sensitized Solar Cells, Journal of the American Chemical Society, 124 (2002) 11215-11222.

[114] J. Wu, Z. Lan, S. Hao, P. Li, J. Lin, M. Huang, L. Fang, Y. Huang, Progress on the electrolytes for dye-sensitized solar cells, Pure and Applied Chemistry, 80 (2008) 2241-2258.

[115] Y. Gao, L. Chu, M. Wu, L. Wang, W. Guo, T. Ma, Improvement of adhesion of Pt-free counter electrodes for low-cost dye-sensitized solar cells, Journal of Photochemistry and Photobiology A: Chemistry, 245 (2012) 66-71.

[116] N. Papageorgiou, W.F. Maier, M. Grätzel, An Iodine/Triiodide Reduction Electrocatalyst for Aqueous and Organic Media, Journal of The Electrochemical Society, 144 (1997) 876-884.

[117] G. Tsekouras, A.J. Mozer, G.G. Wallace, Enhanced performance of dye sensitized solar cells utilizing platinum electrodeposit counter electrodes, Journal of the Electrochemical Society, 155 (2008) K124-K128.

[118] X. Fang, T. Ma, G. Guan, M. Akiyama, E. Abe, Performances characteristics of dye-sensitized solar cells based on counter electrodes with Pt films of different thickness, Journal of Photochemistry and Photobiology A: Chemistry, 164 (2004) 179-182.

[119] G. Khelashvili, S. Behrens, C. Weidenthaler, C. Vetter, A. Hinsch, R. Kern, K. Skupien, E. Dinjus, H. Bönnemann, Catalytic platinum layers for dye solar cells: A comparative study, Thin Solid Films, 511‒512 (2006) 342-348.

[120] J.-Z. Chen, Y.-C. Yan, K.-J. Lin, Effects of Carbon Nanotubes on Dye-Sensitized Solar Cells, Journal of the Chinese Chemical Society, 57 (2010) 1180-1184.

[121] G. Syrrokostas, A. Siokou, G. Leftheriotis, P. Yianoulis, Degradation mechanisms of Pt counter electrodes for dye sensitized solar cells, Solar Energy Materials and Solar Cells, 103 (2012) 119-127.

[122] L. Andrade, H.A. Ribeiro, A. Mendes, Dye‒Sensitized Solar Cells: An Overview, Encyclopedia of Inorganic and Bioinorganic Chemistry, (2011).

[123] A. Kay, M. Grätzel, Low cost photovoltaic modules based on dye sensitized nanocrystalline titanium dioxide and carbon powder, Solar Energy Materials and Solar Cells, 44 (1996) 99-117.

[124] J. Velten, A.J. Mozer, D. Li, D. Officer, G. Wallace, R. Baughman, A. Zakhidov, Carbon nanotube/graphene nanocomposite as efficient counter electrodes in dye-sensitized solar cells, Nanotechnology, 23 (2012) 085201.

[125] A. sedghi, H.n. miankushki, Effect of Multi Walled Carbon Nanotubes as Counter Electrode on Dye Sensitized Solar Cells, International Journal of ELECTROCHEMICAL SCIENCE, 9 (2014) 2029-2037.

[126] M. Grätzel, Solar energy conversion by dye-sensitized photovoltaic cells, Inorganic chemistry, 44 (2005) 6841-6851.

[127] A. Hagfeldt, G. Boschloo, L. Sun, L. Kloo, H. Pettersson, Dye-sensitized solar cells, Chemical reviews, 110 (2010) 6595-6663.

[128] M. Gervaldo, F. Fungo, E.N. Durantini, J.J. Silber, L. Sereno, L. Otero, Carboxyphenyl metalloporphyrins as photosensitizers of semiconductor film electrodes. A study of the effect of different central metals, The Journal of Physical Chemistry B, 109 (2005) 20953-20962.

[129] A. Hauch, A. Georg, Diffusion in the electrolyte and charge-transfer reaction at the platinum electrode in dye-sensitized solar cells, Electrochimica Acta, 46 (2001) 3457-3466.

[130] B.C. O'Regan, I. López-Duarte, M.V. Martínez-Díaz, A. Forneli, J. Albero, A. Morandeira, E. Palomares, T. Torres, J.R. Durrant, Catalysis of recombination and its limitation on open circuit voltage for dye sensitized photovoltaic cells using phthalocyanine dyes, Journal of the American Chemical Society, 130 (2008) 2906-2907.

[131] B.C. O'Regan, K. Walley, M. Juozapavicius, A. Anderson, F. Matar, T. Ghaddar, S.M. Zakeeruddin, C. Klein, J.R. Durrant, Structure/function relationships in dyes for solar energy conversion: a two-atom change in dye structure and the mechanism for its effect on cell voltage, Journal of the American Chemical Society, 131 (2009) 3541-3548.

[132] J.B. Baxter, E.S. Aydil, Dye-sensitized solar cells based on semiconductor

morphologies with ZnO nanowires, Solar Energy Materials and Solar Cells, 90 (2006) 607-622.

[133] A.F. Nogueira, M.-A. De Paoli, I. Montanari, R. Monkhouse, J. Nelson, J.R. Durrant, Electron transfer dynamics in dye sensitized nanocrystalline solar cells using a polymer electrolyte, The Journal of Physical Chemistry B, 105 (2001) 7517-7524.

[134] I. Montanari, J. Nelson, J.R. Durrant, Iodide electron transfer kinetics in dye-sensitized nanocrystalline TiO2 films, The Journal of Physical Chemistry B, 106 (2002) 12203-12210.

[135] C. Bauer, G. Boschloo, E. Mukhtar, A. Hagfeldt, Interfacial Electron-Transfer Dynamics in Ru(tcterpy)(NCS)3-Sensitized TiO2 Nanocrystalline Solar Cells, The Journal of Physical Chemistry B, 106 (2002) 12693-12704.

[136] S.A. Haque, Y. Tachibana, D.R. Klug, J.R. Durrant, Charge recombination kinetics in dye-sensitized nanocrystalline titanium dioxide films under externally applied bias, The Journal of Physical Chemistry B, 102 (1998) 1745-1749.

[137] S. Pelet, J.-E. Moser, M. Grätzel, Cooperative effect of adsorbed cations and iodide on the interception of back electron transfer in the dye sensitization of nanocrystalline TiO2, The Journal of Physical Chemistry B, 104 (2000) 1791-1795.

[138] A. Kay, R. Humphry-Baker, M. Graetzel, Artificial photosynthesis. 2. Investigations on the mechanism of photosensitization of nanocrystalline TiO2 solar cells by chlorophyll derivatives, The Journal of Physical Chemistry, 98 (1994) 952-959.

[139] R. Mosurkal, J.-A. He, J. Kumar, L. Li, J. Walker, L. Samuelson, Rod-like dinuclear ruthenium complexes for dye-sensitized photovoltaics, in: MATERIALS RESEARCH SOCIETY SYMPOSIUM PROCEEDINGS, Warrendale, Pa.; Materials Research Society; 1999, 2002, pp. 367-374.

[140] S. Tatay, S.A. Haque, B. O'Regan, J.R. Durrant, W. Verhees, J. Kroon, A. Vidal-Ferran, P. Gaviña, E. Palomares, Kinetic competition in liquid electrolyte and solid-state cyanine dye sensitized solar cells, Journal of Materials Chemistry, 17 (2007) 3037-3044.

[141] P. Qin, X. Yang, R. Chen, L. Sun, T. Marinado, T. Edvinsson, G. Boschloo, A. Hagfeldt, Influence of π-conjugation units in organic dyes for dye-sensitized solar cells, The Journal of Physical Chemistry C, 111 (2007) 1853-1860.

[142] S. Wenger, P.-A. Bouit, Q. Chen, J. Teuscher, D.D. Censo, R. Humphry-Baker, J.-E. Moser, J.L. Delgado, N. Martín, S.M. Zakeeruddin, Efficient electron transfer and sensitizer regeneration in stable π-extended tetrathiafulvalene-sensitized solar cells, Journal of the American Chemical Society, 132 (2010) 5164-5169.

[143] S. Ferrere, A. Zaban, B.A. Gregg, Dye sensitization of nanocrystalline tin oxide by perylene derivatives, The Journal of Physical Chemistry B, 101 (1997) 4490-4493.

[144] G. Wolfbauer, A.M. Bond, J.C. Eklund, D.R. MacFarlane, A channel flow cell system specifically designed to test the efficiency of redox shuttles in dye sensitized solar cells, Solar energy materials and solar cells, 70 (2001) 85-101.

[145] T. Privalov, G. Boschloo, A. Hagfeldt, P.H. Svensson, L. Kloo, A study of the interactions between $I-/I3-$ redox mediators and organometallic sensitizing dyes in solar cells, The Journal of Physical Chemistry C, 113 (2008) 783-790.

[146] N. Koide, L. Han, Measuring methods of cell performance of dye-sensitized solar cells, Review of scientific instruments, 75 (2004) 2828-2831.

[147] C.H. Seaman, Calibration of solar cells by the reference cell method—the spectral mismatch problem, Solar Energy, 29 (1982) 291-298.

[148] M.A. Green, Solar cell fill factors: General graph and empirical expressions, Solid-State Electronics, 24 (1981) 788-789.

[149] J. Nelson, S.A. Haque, D.R. Klug, J.R. Durrant, Trap-limited recombination in dye-sensitized nanocrystalline metal oxide electrodes, Physical Review B, 63 (2001) 205321.

[150] S.G. Yan, J.T. Hupp, Energetics of Electron Transfer at the Nanocrystalline Titanium Dioxide Semiconductor/Aqueous Solution Interface: pH Invariance of the Metal-Based Formal Potential of a Representative Surface-Attached Dye Couple, The Journal of Physical Chemistry B, 101 (1997) 1493-1495.

[151] K. Hara, M. Kurashige, Y. Dan-oh, C. Kasada, A. Shinpo, S. Suga, K. Sayama, H. Arakawa, Design of new coumarin dyes having thiophene moieties for highly efficient organic-dye-sensitized solar cells, New Journal of Chemistry, 27 (2003) 783-785.

[152] L. Schmidt Mende, U. Bach, R. Humphry Baker, T. Horiuchi, H. Miura, S. Ito, S. Uchida, M. Grätzel, Organic Dye for Highly Efficient Solid State Dye Sensitized Solar Cells, Advanced Materials, 17 (2005) 813-815.

[153] L. Dloczik, O. Ileperuma, I. Lauermann, L. Peter, E. Ponomarev, G. Redmond, N. Shaw, I. Uhlendorf, Dynamic response of dye-sensitized nanocrystalline solar cells: characterization by intensity-modulated photocurrent spectroscopy, The Journal of Physical Chemistry B, 101 (1997) 10281-10289.

[154] J. Bisquert, Chemical diffusion coefficient of electrons in nanostructured semiconductor electrodes and dye-sensitized solar cells, The Journal of Physical Chemistry B, 108 (2004) 2323-2332.

[155] H. Greijer Agrell, G. Boschloo, A. Hagfeldt, Conductivity studies of nanostructured TiO2 films permeated with electrolyte, The Journal of Physical Chemistry B, 108 (2004) 12388-12396.

[156] R. van de Krol, A. Goossens, E.A. Meulenkamp, Electrical and optical properties of TiO2 in accumulation and of lithium titanate Li0. 5TiO2, Journal of Applied Physics, 90 (2001) 2235-2242.

[157] F. Fabregat-Santiago, J. Bisquert, G. Garcia-Belmonte, G. Boschloo, A. Hagfeldt, Influence of electrolyte in transport and recombination in dye-sensitized solar cells studied by impedance spectroscopy, Solar Energy Materials and Solar Cells, 87 (2005) 117-131.

[158] C. He, L. Zhao, Z. Zheng, F. Lu, Determination of electron diffusion coefficient and lifetime in dye-sensitized solar cells by electrochemical impedance spectroscopy at high fermi level conditions, The Journal of Physical Chemistry C, 112 (2008) 18730-18733.

[159] H. Wang, J. He, G. Boschloo, H. Lindström, A. Hagfeldt, S.-E. Lindquist, Electrochemical investigation of traps in a nanostructured TiO2 film, The Journal of Physical Chemistry B, 105 (2001) 2529-2533.

[160] J.-H. Yum, E. Baranoff, S. Wenger, M.K. Nazeeruddin, M. Gratzel, Panchromatic engineering for dye-sensitized solar cells, Energy & Environmental Science, 4 (2011) 842-857.

[161] Z. Shenmin, Z. Di, C. Zhixin, G. Jiajun, L. Wenfei, J. Haibo, Z. Gang, A simple and effective approach towards biomimetic replication of photonic structures from butterfly wings, Nanotechnology, 20 (2009) 315303.

[162] X. Liu, S. Zhu, D. Zhang, Z. Chen, Replication of butterfly wing in TiO2 with

ordered mesopores assembled inside for light harvesting, Materials Letters, 64 (2010) 2745-2747.

[163] Z. Han, S. Niu, L. Zhang, Z. Liu, L. Ren, Light Trapping Effect in Wing Scales of Butterfly Papilio peranthus and Its Simulations, Journal of Bionic Engineering, 10 (2013) 162-169.

[164] W. Zhang, D. Zhang, T. Fan, J. Gu, J. Ding, H. Wang, Q. Guo, H. Ogawa, Novel Photoanode Structure Templated from Butterfly Wing Scales, Chemistry of Materials, 21 (2009) 33-40.

[165] C. Yin, S. Zhu, F. Yao, J. Gu, W. Zhang, Z. Chen, D. Zhang, Biomimetic fabrication of WO3 for water splitting under visible light with high performance, Journal of Nanoparticle Research, 15 (2013) 1-11.

[166] L. Ding, H. Zhou, S. Lou, J. Ding, D. Zhang, H. Zhu, T. Fan, Butterfly wing architecture assisted CdS/Au/TiO2 Z-scheme type photocatalytic water splitting, International Journal of Hydrogen Energy, 38 (2013) 8244-8253.

[167] H. Liu, QibinZhao, H. Zhou, J. Ding, D. Zhang, H. Zhu, T. Fan, Hydrogen evolution via sunlight water splitting on an artificial butterfly wing architecture, Physical Chemistry Chemical Physics, 13 (2011) 10872-10876.

[168] T.-Y. Kim, J.-W. Lee, E.-M. Jin, J.-Y. Park, J.-H. Kim, K.-H. Park, In situ measurement of dye adsorption on TiO2 thin films for dye-sensitized solar cells, Measurement, 46 (2013) 1692-1697.

[169] T. Horikawa, M. Katoh, T. Tomida, Preparation and characterization of nitrogen-doped mesoporous titania with high specific surface area, Microporous and Mesoporous Materials, 110 (2008) 397-404.

[170] A. Zaban, M. Greenshtein, J. Bisquert, Determination of the Electron Lifetime in Nanocrystalline Dye Solar Cells by Open-Circuit Voltage Decay Measurements, ChemPhysChem, 4 (2003) 859-864.

[171] M. Gratzel, Photoelectrochemical cells, Nature, 414 (2001) 338-344.

[172] L.M. Goncalves, V. de Zea Bermudez, H.A. Ribeiro, A.M. Mendes, Dye-sensitized solar cells: A safe bet for the future, Energy & Environmental Science, 1 (2008) 655-667.

[173] C.-W. Hsu, S.-T. Ho, K.-L. Wu, Y. Chi, S.-H. Liu, P.-T. Chou, Ru(ii) sensitizers

with a tridentate heterocyclic cyclometalate for dye-sensitized solar cells, Energy & Environmental Science, 5 (2012) 7549-7554.

[174] K.-L. Wu, C.-H. Li, Y. Chi, J.N. Clifford, L. Cabau, E. Palomares, Y.-M. Cheng, H.-A. Pan, P.-T. Chou, Dye Molecular Structure Device Open-Circuit Voltage Correlation in Ru(II) Sensitizers with Heteroleptic Tridentate Chelates for Dye-Sensitized Solar Cells, Journal of the American Chemical Society, 134 (2012) 7488-7496.

[175] S. Lu, S.-S. Sun, R. Geng, J. Gao, Effects of modified TiO2 photoanode on the photoelectrochemical properties of dye sensitized solar cells, Thin Solid Films, 589 (2015) 8-12.

[176] I. Luisetto, S. Licoccia, A. D'Epifanio, A. Sanson, E. Mercadelli, E. Di Bartolomeo, Electrochemical performance of spin coated dense BaZr0.80Y0.16Zn0.04O3-δ membranes, Journal of Power Sources, 220 (2012) 280-285.

[177] M.K. Kashif, J.C. Axelson, N.W. Duffy, C.M. Forsyth, C.J. Chang, J.R. Long, L. Spiccia, U. Bach, A New Direction in Dye-Sensitized Solar Cells Redox Mediator Development: In Situ Fine-Tuning of the Cobalt(II)/(III) Redox Potential through Lewis Base Interactions, Journal of the American Chemical Society, 134 (2012) 16646-16653.

[178] D. Fu, X.L. Zhang, R.L. Barber, U. Bach, Dye-Sensitized Back-Contact Solar Cells, Advanced Materials, 22 (2010) 4270-4274.

[179] R.Y. Ogura, S. Nakane, M. Morooka, M. Orihashi, Y. Suzuki, K. Noda, High-performance dye-sensitized solar cell with a multiple dye system, Applied Physics Letters, 94 (2009) 073308.

[180] Y. Noma, K. Iizuka, Y. Ogomi, S.S. Pandey, S. Hayase, Preparation of double dye-layer structure of dye-sensitized solar cells from cocktail solutions for harvesting light in wide range of wavelengths, Japanese Journal of Applied Physics, 48 (2009) 020213.

[181] L.H. Nguyen, H.K. Mulmudi, D. Sabba, S.A. Kulkarni, S.K. Batabyal, K. Nonomura, M. Grätzel, S.G. Mhaisalkar, A selective co-sensitization approach to increase photon conversion efficiency and electron lifetime in dye-sensitized solar cells, Physical Chemistry Chemical Physics, 14 (2012) 16182-16186.

[182] J.J. Cid, J.H. Yum, S.R. Jang, M.K. Nazeeruddin, E. Martínez Ferrero, E. Palomares, J. Ko, M. Grätzel, T. Torres, Molecular Cosensitization for Efficient Panchromatic Dye Sensitized Solar Cells, Angewandte Chemie, 119 (2007) 8510-8514.

[183] C.-M. Lan, H.-P. Wu, T.-Y. Pan, C.-W. Chang, W.-S. Chao, C.-T. Chen, C.-L. Wang, C.-Y. Lin, E.W.-G. Diau, Enhanced photovoltaic performance with co-sensitization of porphyrin and an organic dye in dye-sensitized solar cells, Energy & Environmental Science, 5 (2012) 6460-6464.

[184] K.-M. Lee, Y.-C. Hsu, M. Ikegami, T. Miyasaka, K.J. Thomas, J.T. Lin, K.-C. Ho, Co-sensitization promoted light harvesting for plastic dye-sensitized solar cells, Journal of Power Sources, 196 (2011) 2416-2421.

[185] G.-W. Lee, D. Kim, M.J. Ko, K. Kim, N.-G. Park, Evaluation on over photocurrents measured from unmasked dye-sensitized solar cells, Solar Energy, 84 (2010) 418-425.

[186] K. Sayama, S. Tsukagoshi, T. Mori, K. Hara, Y. Ohga, A. Shinpou, Y. Abe, S. Suga, H. Arakawa, Efficient sensitization of nanocrystalline TiO_2 films with cyanine and merocyanine organic dyes, Solar Energy Materials and Solar Cells, 80 (2003) 47-71.

[187] M. Guo, P. Diao, Y.-J. Ren, F. Meng, H. Tian, S.-M. Cai, Photoelectrochemical studies of nanocrystalline TiO_2 co-sensitized by novel cyanine dyes, Solar energy materials and solar cells, 88 (2005) 23-35.

[188] J. Chang, C.-P. Lee, D. Kumar, P.-W. Chen, L.-Y. Lin, K.J. Thomas, K.-C. Ho, Co-sensitization promoted light harvesting for organic dye-sensitized solar cells using unsymmetrical squaraine dye and novel pyrenoimidazole-based dye, Journal of Power Sources, 240 (2013) 779-785.

[189] Y. Ogomi, S.S. Pandey, S. Kimura, S. Hayase, Probing mechanism of dye double layer formation from dye-cocktail solution for dye-sensitized solar cells, Thin Solid Films, 519 (2010) 1087-1092.

[190] A. Yella, H.-W. Lee, H.N. Tsao, C. Yi, A.K. Chandiran, M.K. Nazeeruddin, E.W.-G. Diau, C.-Y. Yeh, S.M. Zakeeruddin, M. Grätzel, Porphyrin-sensitized solar cells with cobalt (II/III)‑based redox electrolyte exceed 12 percent efficiency, science, 334 (2011) 629-634.

[191] L. Wei, Y. Yang, R. Fan, Y. Na, P. Wang, Y. Dong, Effects of rubrene co-sensitized TiO2 photoanode on the performance of ruthenium dye N719 sensitized solar cells, Thin Solid Films, 592, Part A (2015) 14-23.

[192] N. Koumura, Z.-S. Wang, S. Mori, M. Miyashita, E. Suzuki, K. Hara, Alkyl-Functionalized Organic Dyes for Efficient Molecular Photovoltaics, Journal of the American Chemical Society, 128 (2006) 14256-14257.

[193] Y.-S. Ho, G. McKay, Pseudo-second order model for sorption processes, Process biochemistry, 34 (1999) 451-465.

[194] A.W.M. Ip, J.P. Barford, G. McKay, A comparative study on the kinetics and mechanisms of removal of Reactive Black 5 by adsorption onto activated carbons and bone char, Chemical Engineering Journal, 157 (2010) 434-442.

[195] C.-P. Hsu, K.-M. Lee, J.T.-W. Huang, C.-Y. Lin, C.-H. Lee, L.-P. Wang, S.-Y. Tsai, K.-C. Ho, EIS analysis on low temperature fabrication of TiO2 porous films for dye-sensitized solar cells, Electrochimica Acta, 53 (2008) 7514-7522.

[196] H. Zhou, L. Wu, Y. Gao, T. Ma, Dye-sensitized solar cells using 20 natural dyes as sensitizers, Journal of Photochemistry and Photobiology A: Chemistry, 219 (2011) 188-194.

[197] K.-H. Park, T.-Y. Kim, S. Han, H.-S. Ko, S.-H. Lee, Y.-M. Song, J.-H. Kim, J.-W. Lee, Light harvesting over a wide range of wavelength using natural dyes of gardenia and cochineal for dye-sensitized solar cells, Spectrochimica Acta Part A: Molecular and Biomolecular Spectroscopy, 128 (2014) 868-873.

[198] K.-H. Park, T.-Y. Kim, J.-H. Kim, H.J. Kim, C.K. Hong, J.-W. Lee, Adsorption and electrochemical properties of photoelectrodes depending on TiO2 film thickness for dye-sensitized solar cells, Journal of Electroanalytical Chemistry, 708 (2013) 39-45.

Research Activities

Personal:

Name	: Jung-Hun Kim
Date of birth	: February 12, 1986
Gender	: Male
Martial status	: Married
Nationality	: Republic of Korea
Mailing Address	: Department of Biochemical Polymer Engineering, Chosun University, 309, Pilmun-daero, Dong-gu, Gwangju, 61452, Republic of Korea
E-mail Address	: jhkim@chosun.kr, bettertofly@nate.com

Work Experience:

March 2016 ~	: Department of Petroleum Chemistry Process , Hanyeong College, Invited Professor
March 2016 ~ October 2016	: Department of Biochemical Polymer Engineering, Chosun University, Part-time instructor
March 2015 ~ October 2015	: Department of Biochemical Polymer Engineering, Chosun University, Part-time Instructor

Area of Interest:

◎ **Dye-Sensitized Solar Cells** (2011-Present)

1. Synthesis and Characterization of TiO_2 (Sol, Film, Powder, and Fiber)

2. Adsorption Characterization of Dye on TiO_2 electrode

◎ **Adsorption and Separation Technologies** (2010-Present)

1. Synthesis and Characterization of Porous Materials

2. Liquid and Gas-Phase Adsorption

(Removal of CO_2, DME, and Dyes)

3. Optimization of Adsorption Process

List of International Scientific Journals (SCI/SCIE):

(9) **Jung-Hun Kim**, Woo-Hyeon Cho, Yong-Min Song, Tae-Young Kim, Kyung-Hee Park, Jae-Wook Lee, **Light harvesting over wide range of wavelengths by rainbow dye-sensitized solar cells**, Journal of Nanoscience and Nanotechnology, Volume 16, Number 2, February 2016, Pages 1553-1557, ISSN : 1533-4880, I/F: 1.339 (SCI)

(8) Tae Young Kim, Seok Jae Kim, En Mi Han, **Jung Hun Kim**, Jae Wook Lee, Kyung Hee Park, **Hierarchical Nanorod/Nanoflower TiO$_2$ Photoanode for Natural Dye-Sensitized Solar Cells**, International Journal of Electrochemical Science, Volume 10, 30 September 2015, Pages 9466–9474, ISSN : 1452-3981, I/F: 1.956 (SCI-E)

(7) Kyung Hee Park, Tae Young Kim, Hyun Seok Ko, Eun Mi Han, Suk Ho Lee, **Jung-Hun Kim**, Jae Wook Lee, **Analysis of chameleonic change of red cabbage depending on broad pH range for dye-sensitized solar cells**, Journal of Nanoscience and Nanotechnology, Volume 15, Number 8, August 2015, Pages 5840–5844, ISSN : 1533-4880, I/F: 1.339 (SCI)

(6) **Jung-Hun Kim**, Tae Young Kim, Kyung-Hee Park, Jae-Wook Lee, **Electron lifetimes in hierarchically structured photoelectrodes biotemplated from butterfly wings for dye-sensitized solar cells**, International Journal of Electrochemical Science, Volume 10, 27 May 2015, Pages 5513–5520, ISSN : 1452-3981, I/F: 1.956 (SCI-E)

(5) Oh Oun Kwon, Hyo Jung Lee, Sang-Wook Kim, **Jung-Hun Kim**, Tae-Young Kim, Kyung-Hee Park, Jae-Wook Lee, **Layered co-sensitization of gardenia and monascus for panchromatic light harvesting in dye-sensitized solar cells,** Photonics and Nanostructures − Fundamentals and Applications, Volume 14, April 2015, Pages 71−76, ISSN : 1569-4410, I/F: 1.350 (SCI-E)

(4) Kyung-Hee Park, Tae-Young Kim, Shin Han, Hyun-Seok Ko, Suk-Ho Lee, Yong-Min Song, **Jung-Hun Kim**, Jae-Wook Lee, **Light harvesting over a wide range of wavelength using natural dyes of gardenia and cochineal for dye-sensitized solar cells**, Spectrochimica Acta Part A: Molecular and Biomolecular Spectroscopy,

− 116 −

Volume 128, 24 July 2014, Pages 868–873, ISSN : 1386-1425, I/F: 2.129 (SCI)

(3) Kyung-Hee Park, Tae-Young Kim, **Jung-Hun Kim**, Hyung Jin Kim, Chang Kook Hong, Jae-Wook Lee, **Adsorption and electrochemical properties of photoelectrodes depending on TiO₂ film thickness for dye-sensitized solar cells**, Journal of Electroanalytical Chemistry, Volume 708, 1 November 2013, Pages 39–45, ISSN : 1572-6657, I/F: 2.871 (SCI)

(2) Kyung-Jun Hwang, Wang-Geun Shim, **Jung-Hoon Kim**, Do-Young Choi, Ju-Young Park, Chan Kim, Namsu Kim, Jae-Wook Lee, **Synthesis and characterization of novel activated carbon fibers from Pleuropterus multiflorus TURCZ. (Hasuo)**, Materials Letters, Volume 108, 1 October 2013, Pages 219-221, ISSN : 0167-577X, I/F: 2.269 (SCI)

(1) Tae-Young Kim, Jae-Wook Lee, En-Mei Jin, Ju-Young Park, **Jung-Hun Kim**, Kyung-Hee Park, **In situ measurement of dye adsorption on TiO₂ thin films for dye-sensitized solar cells**, Measurement, Volume 46, Issue 5, June 2013, Pages 1692-1697, ISSN : 0263-2241, I/F: 1.526 (SCI-E)

List of Korean Patent:

(2) 박주영, 최도영, 황철호, 이재욱, 이석호, 임철현, 오일홍, 이재혁, **김정훈**, 김미진, **전기방사와 수열반응을 이용한 반도체산화물 나노섬유 제조방법**, 10-2012-0045152, 출원 (2012.04.30)

(1) 이재욱, 황경준, **김정훈**, 김선영, 황운연, **흡착 및 흡수 공정을 이용한 불화수소의 처리 기술**, 10-2011-0106105, 출원 (2011.10.17)

List of Participation in International Conferences:

(15) **Jung-Hun Kim**, Tae-Young Kim, Kyung-Hee Park, Jae-Wook Lee, **Cocktail and Successive Adsorption of Natural Dyes on Nanoporous Photoelectrode for**

Dye-Sensitized Solar Cells, ICNST2014 The 12th International Conference on Nano Science and Nano Technology, P1-67, P.38, Mokpo National University & Shangria Beach Hotel, KOREA (November 6~7, 2014)

(14) **Jung-Hoon Kim**, Tae-Young Kim, Kyung-Hee Park, Jae-Wook Lee, **Successive adsorption of Natural Dyes for Light harvesting over a wide range of avelengths in Dye-Sensitized Solar Cells**, ICNST2013 The 11th International Conference on Nano Science and Nano Technology, P3-26, P.168, Chosun University, Gwangju, KOREA (November 7~8, 2013)

(13) Yong-Min Song, **Jung-Hun Kim**, Ju-Young Park, Suk-Ho Lee, Jae-Wook Lee, **Successive Adsorption of Gardenia Yellow and Monascus for Cocktail Dye-Sensitized Solar Cells**, ICSST2013 The 7th International Conference on Separation Science & Technology, P.254, Homeland Hotel, Chengdu, Sichuan, CHINA (July 2~4, 2013)

(12) **Jung-Hun Kim**, Kyung-Hee Park, Tae-Young Kim, Jae-Wook Lee, **Measurement of Dye Adsorption on Mesoporous TiO_2 Thin Film for Dye-Sensitized Solar Cells**, ICSST2013 The 7th International Conference on Separation Science & Technology, P.233, Homeland Hotel, Chengdu, Sichuan, CHINA (July 2~4, 2013)

(11) **Jung-Hun Kim**, Yong-Min Song, Jae-Wook Lee, **Adsorption Equilibrium and Kinetics of N719 and MK-2 Dyes on Nanostructured TiO_2 Film for Dye-Sensitized Solar Cells**, ICSST2013 The 7th International Conference on Separation Science & Technology, P.215, Homeland Hotel, Chengdu, Sichuan, CHINA (July 2~4, 2013)

(10) Jeon-Hee Kim, **Jung-Hun Kim**, Jae-Hyeok Lee, Yong-Min Song, Wang-Geun Shim, Jang-Jin Park, Jea-Wook Lee, **Adsorption Dynamics of Gaseous Radionuclides in Fly Ash Filter**, ICSST2013 The 7th International Conference on Separation Science & Technology, P.214, Homeland Hotel, Chengdu, Sichuan, CHINA (July 2~4, 2013)

(9) Jae-Hyeok Lee, **Jung-Hun Kim**, Joon-Hyung Park, Wang-Geun Shim, Jae-Wook Lee, **Adsorption Energy Distribution of Hollow Carbon fibers prepared from biomass**, POLYCHAR21 World Forum on Advanced Materials BOOK OF ABSTRACTS, CHOSUN UNIVERSITY, 14-PP-26, P.244, Gwangju, KOREA

(March 11~15, 2013)

(8) **Jung-Hun Kim**, Tae-Young Kim, Kyung-Hee Park, Jae-Wook Lee, **Competitive adsorption of gardenia and monascus for cocktail dye-sensitized solar cells**, POLYCHAR21 World Forum on Advanced Materials BOOK OF ABSTRACTS, CHOSUN UNIVERSITY, 13-PP-52, P.202, Gwangju, KOREA (March 11~15, 2013)

(7) **Jung-Hun Kim**, Tae-Young Kim, Kyung-Hee Park, Jae-Wook Lee, **Selective anchoring of organic and inorganic dyes for cocktail dye-sensitized solar cells**, POLYCHAR21 World Forum on Advanced Materials BOOK OF ABSTRACTS, CHOSUN UNIVERSITY, 14-IL-13, P.49, Gwangju, KOREA (March 11~15, 2013)

(6) **Jung Hun KIM**, Kyung Hee PARK, Tae Young KIM, Jae Wook LEE, **PHOTOVOLTAIC PERFORMANCE OF GARDENIA YELLOW SEPARATED BY NONIONIC POLYMERIC SORBENT FOR DYE-SENSITIZED SOLAR CELLS**, AFORE2012 Asia-Pacific Forum on Renewable Energy 2012 Abstract Book, P-PV-021, P.287, Lotte Hotel, Jeju, KOREA (November 26~29, 2012)

(5) **Jung Hun KIM**, Kyung Hee PARK, Tae Young KIM, Jae Wook LEE, **INFLUENCE OF TIO_2 FILM THICKNESS ON MASS TRANSPORT OF DYE MOLECULE AND TRIIODIDE/IODIDE REDOX COUPLE IN DYE-SENSITIZED SOLAR CELLS**, AFORE2012 Asia-Pacific Forum on Renewable Energy 2012 Abstract Book, P-PV-020, P.286, Lotte Hotel, Jeju, KOREA (November 26~29, 2012)

(4) Jae-Wook LEE, **Jung-Hun Kim**, Ju-Young PARK, Do-Young CHOI, Chel-Ho HWANG, **Enhancement of photoelectric performance of Dye-sensitized solar cells using metal-doped Titaniun nanofiber electrodes**, AFORE2012 Asia-Pacific Forum on Renewable Energy 2012 Abstract Book, P-PV-018, P.284, Lotte Hotel, Jeju, KOREA (November 26~29, 2012)

(3) Tae Young KIM, Byoung Jun Min, Kyung Hee PARK, Jae Wook LEE, **Jung-Hun KIM**, Sung Yong CHO, **Adsorption chrcteristics of gardenia blue on TiO2 thin film for dye-sensitized solar cells**, AFORE2012 Asia-Pacific Forum on Renewable Energy 2012 Abstract Book, P-PV-013, P.279, Lotte Hotel, Jeju, KOREA

(November 26~29, 2012)

(2) Tae-Young Kim, Byong-Jun Min, **Jung-Hun Kim**, Sung-Yong Cho, **A Study on the Characteristics of TiO$_2$ Impregnated with Silver for Polymer Electrolyte Fuel Cells**, ICSST11 9th International Conference on Separation Science and Technology PROGRAM & ABSTRACTS, HP-15, P.333, Grand Hotel, Jeju, KOREA (November 3~5, 2011)

(1) **Jung-Hun Kim**, Jae-Hyeok Lee, Kyung-Jun Hwang, Jae-Wook Lee, **Adsorption of Hydrogen Fluoride on Activated Alumina**, ICSST11 9th International Conference on Separation Science and Technology PROGRAM & ABSTRACTS, DP-38, P.173, Grand Hotel, Jeju, KOREA (November 3~5, 2011)

Award:

(1) 광주광역시 청소년 활동진흥센터장賞, "지역사회발전과 봉사활동 활성화에 기여한 공", (2006.12.08)
(2) 경찰청장賞, "경찰행정 발전에 기여한 공", (2008.10.21.)
(3) 우수 포스터논문賞, *한국화학공학회 2011년도 가을 총회 및 학술대회* (2011)
(4) 입선, 2013 재료연구소 소재사진 공모전, (2013.08.30.)

Scholarship:

(1) 실험 조교 장학금, 조선대학교 일반대학원 (2011) 1~2학기
(2) 실험 조교 장학금, 조선대학교 일반대학원 (2012) 1학기
(3) 연구 보조 장학금, 조선대학교 일반대학원 (2012) 1학기
(4) 실험 조교 장학금, 조선대학교 일반대학원 (2013) 1~2학기
(5) 연구 보조 장학금, 조선대학교 일반대학원 (2013) 1~2학기
(6) 연구 조교 장학금, 조선대학교 일반대학원 (2014) 1~2학기
(5) 연구 보조 장학금, 조선대학교 일반대학원 (2014) 1학기

Table of Research Results (2010 – Present)

Research	Total
SCI(SCIE) Journal	9
Domestic Journal	0
Domestic Journal	15
Domestic Conference	24
Korean Patent	2